NAVAL POSTGRADUATE SCHOOL

MONTEREY, CALIFORNIA

THESIS

MAXIMUM POWER POINT TRACKING OF A PHOTOVOLTAIC SYSTEM UTILIZING AN INTERLEAVED BOOST CONVERTER

by

James S. Topping

September 2015

Thesis Advisor: Giovanna Oriti
Co-Advisor: Alexander L. Julian

Approved for public release; distribution is unlimited

THIS PAGE INTENTIONALLY LEFT BLANK

REPORT DOCUMENTATION PAGE		*Form Approved OMB No. 0704–0188*

Public reporting burden for this collection of information is estimated to average 1 hour per response, including the time for reviewing instruction, searching existing data sources, gathering and maintaining the data needed, and completing and reviewing the collection of information. Send comments regarding this burden estimate or any other aspect of this collection of information, including suggestions for reducing this burden, to Washington headquarters Services, Directorate for Information Operations and Reports, 1215 Jefferson Davis Highway, Suite 1204, Arlington, VA 22202-4302, and to the Office of Management and Budget, Paperwork Reduction Project (0704-0188) Washington, DC 20503.

1. AGENCY USE ONLY *(Leave blank)*	2. REPORT DATE September 2015	3. REPORT TYPE AND DATES COVERED Master's Thesis	
4. TITLE AND SUBTITLE MAXIMUM POWER POINT TRACKING OF A PHOTOVOLTAIC SYSTEM UTILIZING AN INTERLEAVED BOOST CONVERTER		5. FUNDING NUMBERS	
6. AUTHOR(S) Topping, James S.			
7. PERFORMING ORGANIZATION NAME(S) AND ADDRESS(ES) Naval Postgraduate School Monterey, CA 93943-5000		8. PERFORMING ORGANIZATION REPORT NUMBER	
9. SPONSORING /MONITORING AGENCY NAME(S) AND ADDRESS(ES) N/A		10. SPONSORING/MONITORING AGENCY REPORT NUMBER	

11. SUPPLEMENTARY NOTES The views expressed in this thesis are those of the author and do not reflect the official policy or position of the Department of Defense or the U.S. Government. IRB Protocol number ___N/A___.

12a. DISTRIBUTION / AVAILABILITY STATEMENT Approved for public release; distribution is unlimited	12b. DISTRIBUTION CODE

13. ABSTRACT (maximum 200 words)

Over the last several years, the Department of Defense has focused on conserving energy in order to enhance its combat capabilities. Renewable energy technologies, such as wind, solar, biomass, and others, have been explored so that the military can reduce its reliance on fossil fuels and improve its operational range. One of the components to this effort is solar photovoltaic (PV) technology. The purpose of this thesis is to demonstrate the importance of using a maximum power point tracking (MPPT) algorithm to ensure that a PV system provides the most energy possible. Moreover, two different MPPT algorithms are presented in this thesis. An interleaved boost converter controls the flow of power to a load and a 24-volt source. Also, it regulates the PV panel's voltage and current so that the panel may operate at its maximum power point. A complete model of the solar panel, boost converter, and control algorithms was created in Simulink in order to validate the system in simulation. The control algorithms were implemented using a field-programmable gate array so that the actual system could be tested and compared against the simulation. Experimental measurements validate the model and demonstrate that the MPPT algorithms perform as expected.

14. SUBJECT TERMS solar, photovoltaic, maximum power point tracking, MPPT, interleaved boost converter, Xilinx, field-programmable gate array, perturb and observe, incremental conductance	15. NUMBER OF PAGES 155
	16. PRICE CODE

17. SECURITY CLASSIFICATION OF REPORT Unclassified	18. SECURITY CLASSIFICATION OF THIS PAGE Unclassified	19. SECURITY CLASSIFICATION OF ABSTRACT Unclassified	20. LIMITATION OF ABSTRACT UU

NSN 7540–01-280-5500

Standard Form 298 (Rev. 2–89)
Prescribed by ANSI Std. 239–18

i

THIS PAGE INTENTIONALLY LEFT BLANK

MAXIMUM POWER POINT TRACKING OF A PHOTOVOLTAIC SYSTEM UTILIZING AN INTERLEAVED BOOST CONVERTER

James S. Topping
Major, United States Marine Corps
B.S., United States Air Force Academy, 2001

Submitted in partial fulfillment of the
requirements for the degree of

MASTER OF SCIENCE IN ELECTRICAL ENGINEERING

from the

NAVAL POSTGRADUATE SCHOOL
September 2015

Author: James S. Topping

Approved by: Giovanna Oriti
                     Thesis Advisor

                     Alexander L. Julian
                     Co-Advisor

                     R. Clark Robertson
                     Chair, Department of Electrical and Computer Engineering

THIS PAGE INTENTIONALLY LEFT BLANK

ABSTRACT

Over the last several years, the Department of Defense has focused on conserving energy in order to enhance its combat capabilities. Renewable energy technologies, such as wind, solar, biomass, and others, have been explored so that the military can reduce its reliance on fossil fuels and improve its operational range. One of the components to this effort is solar photovoltaic (PV) technology. The purpose of this thesis is to demonstrate the importance of using a maximum power point tracking (MPPT) algorithm to ensure that a PV system provides the most energy possible. Moreover, two different MPPT algorithms are presented in this thesis. An interleaved boost converter controls the flow of power to a load and a 24-volt source. Also, it regulates the PV panel's voltage and current so that the panel may operate at its maximum power point. A complete model of the solar panel, boost converter, and control algorithms was created in Simulink in order to validate the system in simulation. The control algorithms were implemented using a field-programmable gate array so that the actual system could be tested and compared against the simulation. Experimental measurements validate the model and demonstrate that the MPPT algorithms perform as expected.

THIS PAGE INTENTIONALLY LEFT BLANK

TABLE OF CONTENTS

LIST OF FIGURES

xi

THIS PAGE INTENTIONALLY LEFT BLANK

LIST OF TABLES

THIS PAGE INTENTIONALLY LEFT BLANK

LIST OF ACRONYMS AND ABBREVIATIONS

AC	alternating current
ADC	analog-to-digital converter
CCM	continuous conduction mode
DC	direct current
DCM	discontinuous conduction mode
DOD	Department of Defense
EHP	electron-hole pair
ESR	equivalent series resistance
FPGA	field-programmable gate array
GREENS	Ground Renewable Expeditionary Energy Network System
IBC	interleaved boost converter
IC	incremental conductance
IGBT	insulated gate bipolar transistor
IIR	infinite impulse response
KCL	Kirchhoff's Current Law
KVL	Kirchhoff's Voltage Law
MOSFET	metal-oxide semiconductor field-effect transistor
MPP	maximum power point
MPPT	maximum power point tracking
RCC	ripple correlation control
P&O	perturb and observe
PI	proportional-integral
PWM	pulse width modulation
PV	photovoltaic
SPACES	Solar Portable Alternative Communications Energy System
USMC	United States Marine Corps
VHDL	VHSIC hardware description language
VHSIC	very high speed integrated circuit

THIS PAGE INTENTIONALLY LEFT BLANK

ACKNOWLEDGMENTS

I would like to thank my wife, Kim, for all of her support, help, and love while I completed this thesis. I also would like to thank my lovely daughter, Molly, who has definitely brought joy to my life while accomplishing this demanding task.

I would like to thank my family and friends, especially my mother, Kathy, and brother, Andrew, who have supported me over the years. I appreciate their assistance and encouragement.

Professor Giovanna Oriti spent many hours assisting me with writing this document. Additionally, she gave me excellent guidance on how to conduct my research.

Professor Alexander Julian devoted a great deal of time in the laboratory and elsewhere in order to ensure my hardware and computer code worked correctly.

Finally, I want to thank God for blessing me with the talents necessary to complete this research.

THIS PAGE INTENTIONALLY LEFT BLANK

I.   INTRODUCTION

The Department of Defense's (DOD) energy policy "is to enhance military capability, improve energy security, and mitigate costs in its use and management of energy" [1, p. 1]. In order to accomplish that, the DOD has established several priorities such as acquiring alternative energy sources and developing new technologies that help exploit those resources [1]. Solar photovoltaic (PV) energy is just one of those technologies that the DOD is currently pursuing.

The United States Marine Corps (USMC) has devoted itself to achieving several energy goals that are in line with the DOD's objectives. Among them are a few that apply to solar PV energy. First and foremost, the USMC wants to "forge an ethos throughout the Marine Corps equating energy and resource efficiency with combat effectiveness" [2, pp. 21]. It has challenged itself to ensure that at least 50% of all energy consumed will come from alternative energy by 2020 [2]. Also, the Corps has committed itself to achieving its operational energy demands by using renewable energy sources and to making these systems as efficient as possible [2]. Furthermore, the USMC has chosen to fulfill these goals by using photovoltaic devices among other things. For instance, the USMC has fielded two different solar PV systems—the Solar Portable Alternative Communications Energy System (SPACES) and the Ground Renewable Expeditionary Energy Network System (GREENS). These systems are shown in Figures 1, 2, and 3.

While these systems represent a great leap forward by the USMC in terms of expeditionary energy usage, they can and will be improved. For instance, the GREENS employs a maximum power point tracker (MPPT), which attempts to harness the maximum amount of energy from the solar panels, but it uses a centralized controller [3]. As described in [4], centralized MPPT systems can have issues harvesting the maximum available energy during certain conditions. For instance, a voltage or current mismatch between panels due to degraded or shaded panels can be problematic for the system [4]. This concept will be developed later in this thesis. For now, it is sufficient to realize that it is a problem which affects the ability of the MPPT system to extract the maximum available power from the solar panel; thus, using an individual MPPT system per solar

panel is not only important but may also help the Marine Corps as well as the DOD achieve its stated goals.

Figure 1.   Ground Renewable Expeditionary Energy Network System,
from [3].

Various facets of solar energy technology, such as maximum power point tracking, energy storage via a 24-volt battery, power electronics, and control, are explained in this thesis. Initially, a physics-based model of the solar panel, the converter, and control system was created in MATLAB Simulink in order to predict the system's performance. To verify that the actual physical system worked as predicted, the system was assembled in the laboratory with the Raloss SR40-36 solar panel in conjunction with an interleaved boost converter (IBC). This solar panel is displayed in Figure 4. Furthermore, a digital control algorithm was required so that the solar panels operated at their maximum power point (MPP). In this thesis, two control algorithms, perturb and observe (P&O) and incremental conductance (IC), are implemented on a Xilinx field-programmable gate array (FPGA). Ultimately, experimental data as well as the results from the computer simulations are compared against each other.

Figure 2.   A Marine sets up the SPACES, from [5].

A.   PURPOSE

In this part of the introduction, the purpose of this thesis research, which is related to the expeditionary energy goals, is discussed. Given the goals as stated in the previous section as well as other interests, the purpose of this research can be summarized as follows:

- To emphasize the importance of using a MPPT with a solar array.

- To highlight the advantages of using a MPPT on each solar panel.

- To describe how one can use a tracking algorithm to maximize the production of the available energy from a solar panel.

- To demonstrate how digitally controlled power electronics interfaced to a solar panel can achieve the highest efficiency possible in order to power a load.

Ideally, if the goals of this research can be implemented, then the DOD energy goals may be advanced, bringing the DOD one step closer to its energy goals being realized.

3

Figure 3.   Marines employ the GREENS, from [3].

Figure 4.   Raloss SR40-36 solar panel.

B. RESEARCH OBJECTIVES

The objectives of this research are defined as those things that must be done in order to accomplish the stated purpose. Based on the purpose of this thesis, the objectives for this research have been determined and are summarized as follows:

- Detail the physics of a solar cell at a fundamental level.

- Model a solar panel using physics-based equations.

- Construct an interleaved boost converter so that it can power a load and charge a battery simultaneously.

- Simulate the solar PV system so that the performance may be predicted.

- Implement at least two maximum power point tracking algorithms in order to track the MPP of a solar panel.

- Test and record the results of the actual system in order to verify the physics-based model.

- Compare the results against the simulations and evaluate the MPPT algorithms that were utilized against each other.

C. RELATED WORK

In this part of the introduction, other related research that has been previously conducted is briefly discussed in a general sense. Also, the differences of this research in relation to earlier work are presented. Previous literature presented and compared different maximum power point tracking (MPPT) algorithms for various PV systems. There are literally thousands of documents that chronicle MPPT algorithms, and they are too numerous to name here. Later in this thesis, various MPPT algorithms are explained. Moreover, the two algorithms that are used in this thesis research are fairly traditional and have been explored by other researchers. However, in this thesis, these two algorithms are investigated in more detail than most. Additionally, many different types of power converters have been used to control these types of systems. For instance, various DC-to-DC converters, such as the buck, boost, buck-boost, forward, SEPIC, resonant, flyback, and others, as well as DC-to-AC inverters have been used in the implementation of a MPPT system. Interleaving techniques like the one described here

5

also have been employed but to a lesser extent. In this thesis, certain aspects of the interleaved boost converter are explored and explained more fully. A unique aspect of this research is that the MPPT algorithms are synthesized via the Xilinx blockset within Simulink and other Xilinx software. Then the algorithms are loaded into a FPGA for usage. Succinctly put, the novel contribution of this thesis is to present both simulations and experiments of two digitally implemented MPPT techniques utilizing an interleaved boost converter. Additionally, the level of detail with which the author presents these topics contributes further knowledge of these subjects.

II.   THEORY

A.   PHOTOVOLTAIC SOLAR CELL

A brief understanding of how solar cells physically work is provided in this section, which is intended to provide the reader with a fundamental explanation of the physics involved as well as the mathematical equations used to model a solar cell.

1.   Basic Physics

In order to understand how a solar cell physically works, one must have a fundamental grasp of how a diode operates. Diodes are made of semiconductor materials such as germanium and silicon. For the purposes of this discussion, it is assumed that the main element within the semiconductor under consideration is silicon since it is the most prevalent; however, other semiconductor materials are used to make diodes, solar cells, transistors, and other electronic components.

a.   Basic Physics of a Diode

Referencing the periodic table of elements, silicon is a group 4 element, which means that it has four valence electrons in its outermost shell as explained in [6]–[8]. Within a silicon crystal lattice, the outer valence electrons of one atom are interconnected to the valence electrons of other atoms via covalent bonds [6], [7]. A two-dimensional graphical depiction of this concept is presented in Figure 5. The electrons in the valence band do not conduct electricity unless they are excited. If they are stimulated with enough energy from either thermal, electrical, or electromagnetic sources, these electrons transition into the conduction band by breaking their covalent bonds [7]. Of note, this energy gap between the valance band and the conduction band is referred to as the bandgap, which is approximately 1.11 eV for silicon [7], [8]. This means that, within silicon, a single valence electron must absorb 1.11 eV in order to be able to conduct electricity. Additionally, in Figure 5, it must be pointed out that there are four corresponding protons in the nucleus of each silicon atom so that the material is still neutral [7].
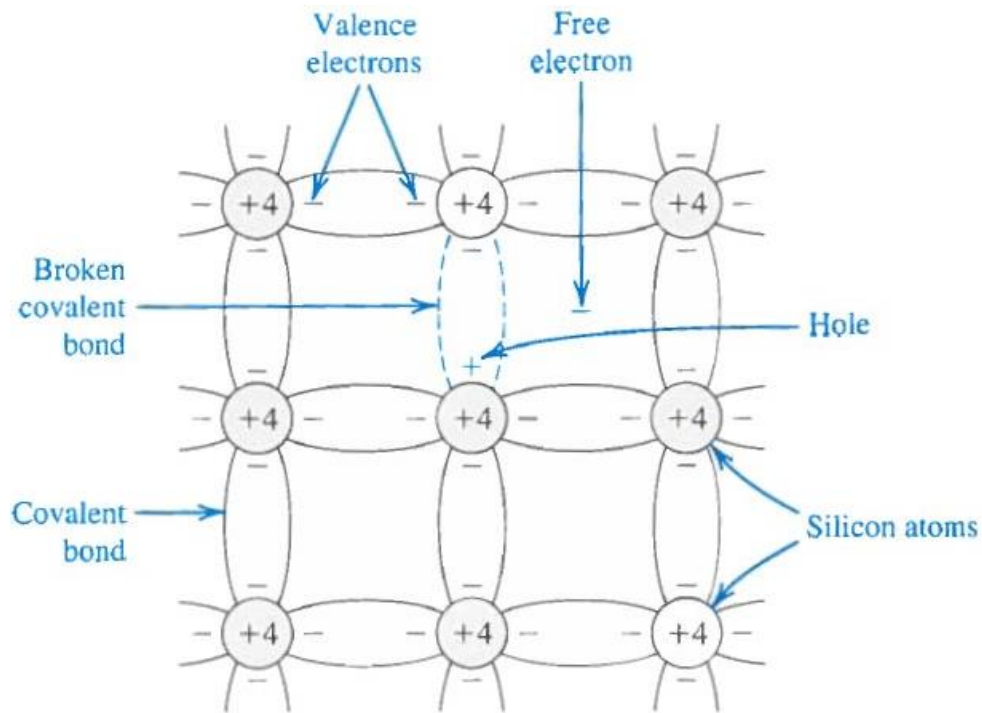
Figure 5.   Silicon crystal lattice showing covalent bonds, from [6].

In order to make a diode, one must dope the crystalline lattice of a semiconductor with impurities. On one side, the semiconductor is doped with a group 5 element such as phosphorus, arsenic, or antimony [8]. This type of structure is depicted in Figure 6 and is called *n*-type since it has an extra electron, which is a negative charge carrier. Since the impurity atom has five corresponding protons in its nucleus, the *n*-type material is still neutral. On the other side of the silicon crystal, a group 3 element such as gallium, indium, or boron is introduced to form a *p*-type semiconductor as shown in Figure 7 [8]. Here, the absence of an electron creates a hole, which is a positive charge carrier. The material remains neutral since the corresponding number of protons within the impurity atom is three vice four.
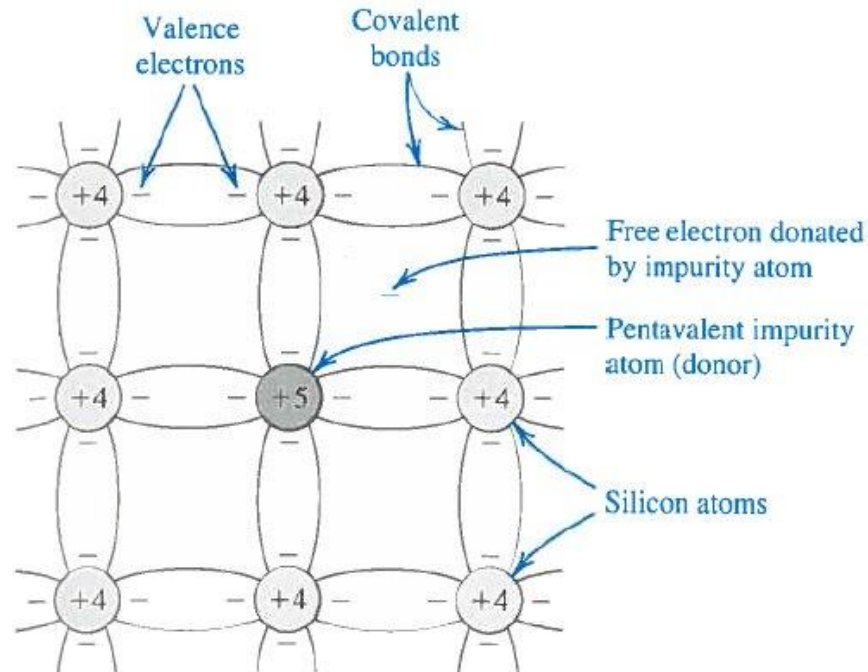
Figure 6.   Pentavalent impurity injected into the crystalline lattice creating an *n*-type semiconductor, from [6].
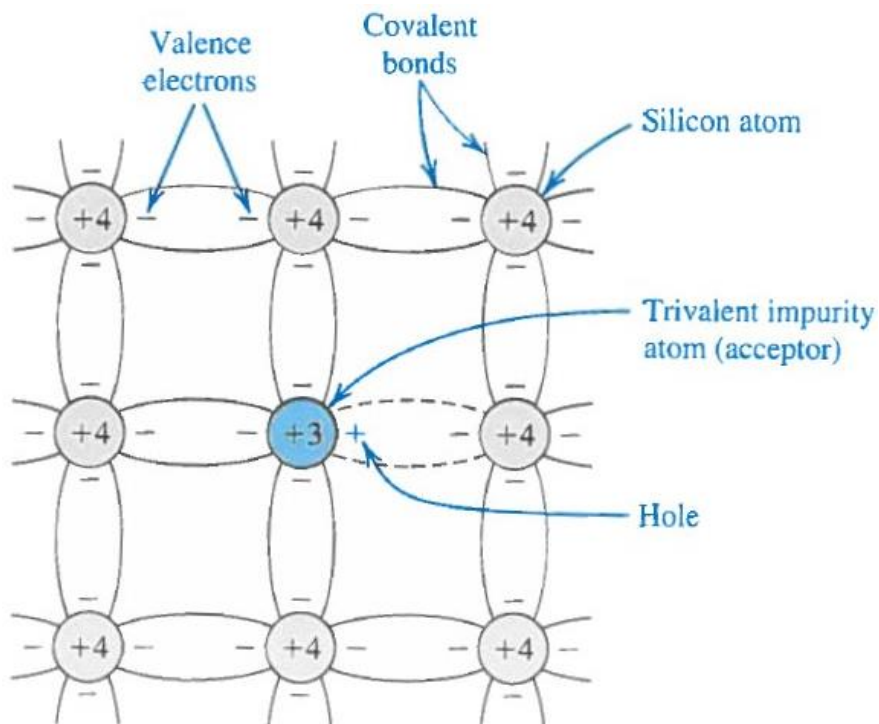
Figure 7.   Trivalent impurity injected into the crystalline lattice creating a *p*-type semiconductor, from [6].

At the *p-n* junction where these two types of materials meet within the silicon crystal, some interesting things happen. First, a process known as diffusion takes place. Diffusion is the process by which charge carriers move from a place of high concentration to a place of lower concentration; hence, some of the holes within the *p*-type material diffuse to the *n*-type side [6]. This is because holes, which are the majority charge carriers on the *p*-type side, are in high concentration on that side, but they are in low concentration on the *n*-type side [6]–[8]. Likewise, some of the electrons within the *n*-type material diffuse to the *p*-type side. This produces a fascinating phenomenon at the junction. Since electrons have moved from the *n*-type material to the *p*-type material, they recombine with the majority holes [6]. This causes a portion of the *p*-type material to become negatively charged due to the fact that the impurity atoms there have only three corresponding protons compared to the four valence electrons. Also, these trivalent impurity atoms are sometimes called acceptors since their holes can more easily accept electrons [6]–[8]. This is because it takes less energy to form a covalent bond [7]. Similarly, the holes that diffused from the *p*-type material into the *n*-type material recombine with the majority electrons on the *n*-type side [6]. Thus, this portion of the *n*-type material becomes positively charged since the impurity atoms on the *n*-type side now have five protons that correspond to only four outer shell electrons. Additionally, these pentavalent impurity atoms are sometimes called donors since they can more easily donate their free electron [6]–[8]. In other words, it takes less energy to separate these free electrons from its attraction to its atom [7].

Consequently, an electric field is created at the *p-n* junction since the *n*-type material is positively charged with respect to the *p*-type material [6]–[8]. When in equilibrium, this electric field restricts additional diffusion of holes and electrons due to its polarity [6]–[8]. To understand why this works, consider the following example under open-circuit conditions. As previously stated, the electrons in the *n*-type material want move to towards the *p*-type region due to diffusion current. At some point, the electric field becomes strong enough that these electrons cannot diffuse anymore and are repelled back towards the *n*-type side. A similar explanation can be made for holes on the *p*-type side. Furthermore, the material in the vicinity of the junction is called the depletion

region (or space-charge region) because it has been depleted of all of its charge carriers [6]. In Figure 8, a depiction of the depletion region is portrayed with its electric field.
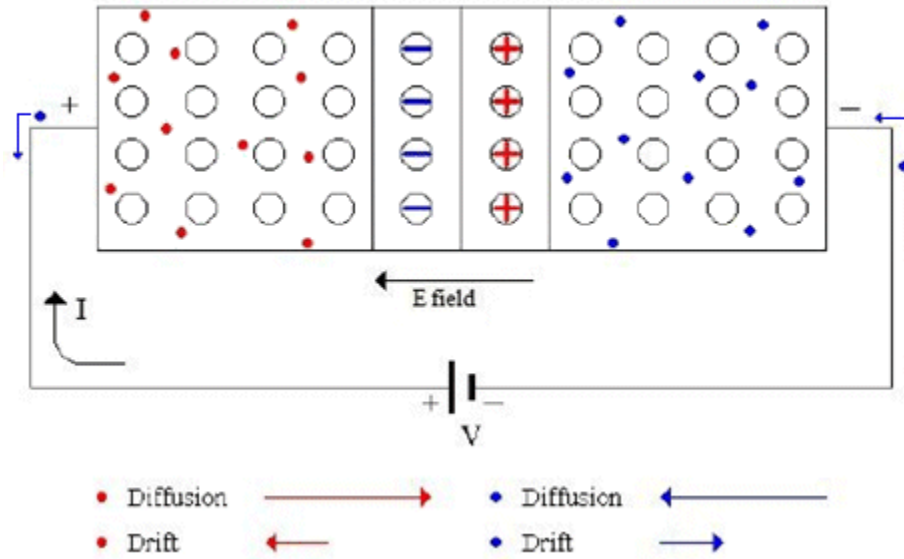
Figure 8.   Forward-biased diode, after [9].

The depletion region gives rise to an additional mechanism called drift. Drift is the process by which charge carriers are influenced by an electric field. Holes, which are deemed positive, drift in the direction of the electric field from the positively charged side to the negatively charged side [6]. On the other hand, electrons, which are designated as negative, drift in the opposite direction of the electric field from the negative side to the positive side [6]. One must remember that the positively charged side is *n*-type, and the negatively charged side is *p*-type; thus, drift current due to the *p-n* junction's electric field works in the opposite direction of the diffusion current. As explained in [6], holes on the *n*-type side and electrons on the *p*-type side move across the junction due to drift current. When in proximity of the depletion region and under the influence of its electric field, these minority carriers, which are dependent on temperature, are swept across the junction due to the polarity of the electric field [6]–[7]. Lastly, based on [6], it can be shown mathematically that the forward-biased current through a diode can be written as

11

$$I = I_D - I_S = I_S\ exp\left[\frac{v}{nV_t}\right] - I_S = I_S\left(exp\left[\frac{v}{nV_t}\right] - 1\right) \tag{1}$$

where I_D is the diffusion current, I_S is the drift current, n is the ideality factor, v is external voltage across the diode, and V_t is the thermal voltage at the junction's temperature. One must realize that the reference direction for the current I is from the diode's positive terminal to its negative terminal. This is important later when analyzing the current through a solar cell.

b.   *Basic Physics of a Solar Cell*

Since many of the basic concepts about diodes have been clarified, the following discussion focuses on the physics behind the operation of a solar cell. The first thing to understand is the notion of electromagnetic energy contained in photons. Photons are the fundamental particles that propagate electromagnetic waves. They are considered to be without mass and do not have any electric charge [10]–[11]. Also, according to Max Planck and Albert Einstein, photons can only exist in quantized levels of energy [10]. That is, they can only attain specific, discrete energy levels as opposed to any arbitrary amount of energy in between those levels [10]. Moreover, Planck discovered that matter absorbs and emits light in distinct quantities of energy, or "packets" of energy [10]. The energy E contained in one photon was shown to be

$$E = \frac{hc}{\lambda} \tag{2}$$

in accordance with [7], [8], and [10], where h is Planck's constant (6.626×10^{-34} J·s), c is the speed of light (3.0×10^8 m/s), and λ is the wavelength of the photon. If one inserts the bandgap energy of silicon, which is 1.11 eV, into (2), one can solve for the corresponding wavelength. As stated in [8], only photons that have a wavelength of 1.12 μm or less are able to generate the energy necessary to separate an electron from its covalent bond so that it may enter the conduction band. This is the fundamental process that makes the photoelectric effect, which Planck and Einstein first theorized, possible.

When a solar PV cell is exposed to electromagnetic radiation via sunlight, a tremendous number of photons are injected into the material. Some of these photons are

absorbed by electrons and energize them [8], [11]. Provided these photons possess the required amount of energy, they cause electrons within the material to break free from their covalent bonds [8], [11]. As a result, these photons create a number of electron-hole pairs (EHP), which are swept across the electric field of the solar cell via the drift principle discussed earlier. Electrons, whether they are generated in the *p*-type or *n*-type region, are forced to flow towards the terminal on the *n*-type side. Once they arrive at that terminal, they flow through the external circuit to power a load. Eventually, the electrons reach the terminal on the *p*-type side, where they are injected back into the solar cell [11]. Additionally, the creation of an EHP causes a hole to be left behind. This allows other valence electrons that are in adjacent atoms to move and take the place of this hole [11]. This leaves behind another hole, and this process repeats itself until, by chance, an electron recombines with this hole [11]. Accordingly, these valence electrons move in the same direction as the conduction electrons, but the holes appear to move in the opposite direction. Ultimately, holes, whether they are created in the *p*-type or *n*-type material, are driven to the terminal on the *p*-type side, where they recombine with electrons from the external circuit [11].

In Figure 9, the flow of electric current and overall operation of a solar cell is illustrated. It is important to note that the reference direction for the current *I* is in the opposite direction to that of a diode. If one were to use the same reference direction that the diode uses for the current, then the voltage versus current plot, which is also known as the I-V curve, would be similar to Figure 10. Here, the solar cell's I-V curve is contrasted against its diode only current. The diode current is the only current that results if the solar cell is not generating any photocurrent. In other words, if the solar cell is placed in the dark and then subjected to the corresponding voltages, it operates just like a diode [8]. For a solar cell, one typically flips the I-V curve on its head to produce the more familiar plots that are presented in Figures 12 and 14. Realize that doing this is akin to reversing the reference direction of the current *I* as is shown in Figure 9.
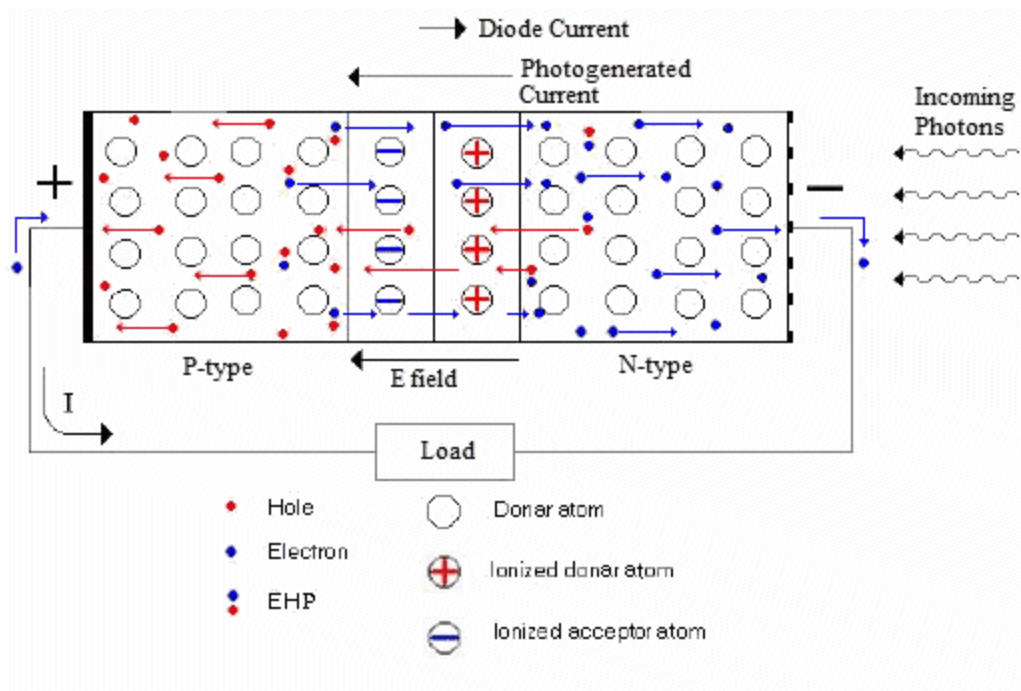
Figure 9.   Solar cell connected to a load, after [9].
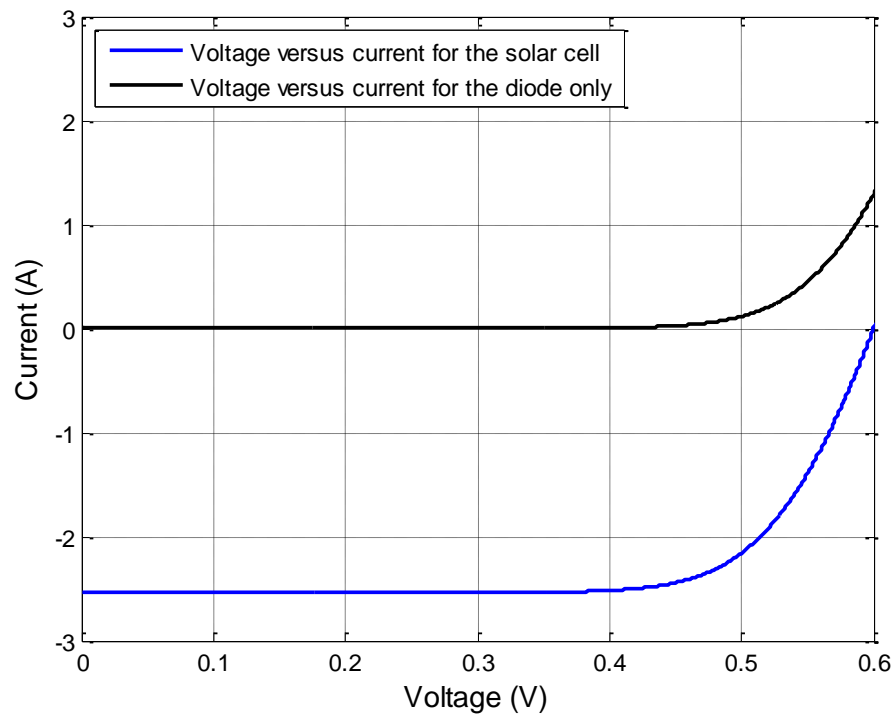
Figure 10.   Voltage versus current for the solar cell and for the diode only, after [7].

14

Based on the physical interactions within the solar cell as well as external to it, there are several possibilities that can transpire. The following is a summary of those scenarios, and this list, while not all inclusive, helps to explain the low efficiency of solar photovoltaic energy conversion.

- Photons are either reflected or absorbed in the atmosphere [11]. This is energy from the sun that does not even make it to the solar cell. While this does not account for the low efficiency, some of this energy could be collected provided the environmental conditions were more suitable.

- Photons reflect off the surface of the solar cell. These particles may strike the surface at a poor angle or may collide with the electric contacts on top of the cell [7], [11]. Either way, they are reflected and are not absorbed by the solar cell. Textured surfaces and anti-reflective coatings help to prevent photons from reflecting off the surface of the solar cell [7], [8].

- A photon of sufficient energy is absorbed by an electron and creates an EHP, but the electron and/or hole ends up recombining internally prior to producing a current external to the solar cell [7].

- Photons of sufficient energy are absorbed by numerous electrons and create many EHPs. Subsequently, the electrons are collected so that an electric current is created in the external circuit [7], [11]. Once the electrons are outside the solar cell, there is no threat of recombination. While this is the best and desired outcome, this current still has to flow through ohmic contacts and electrical wires as well as resistance within in the semiconductor itself; hence, this scenario is not without its own losses [7].

- A photon does not strike an electron and passes through the material without creating an EHP [11]. This problem can be mitigated by using back-surface reflectors as mentioned in [7].

- A low energy photon is absorbed by an electron but does not create an EHP since it cannot raise the electron's energy enough to move it into the conduction band [7], [11]. This excess energy is converted into heat [7], [11].

- A high energy photon, also referred to as a phonon, is absorbed by an electron and creates an EHP [7], [11]. In this case, the amount of energy that exceeds the bandgap energy causes lattice vibrations and is transformed into heat [7], [11].

2. Mathematical Model

In order to model the solar cell, the single-diode model was implemented in accordance with [12]–[14]. In Figure 11, the schematic of the single-diode model that has been used traditionally to represent a solar cell is illustrated.
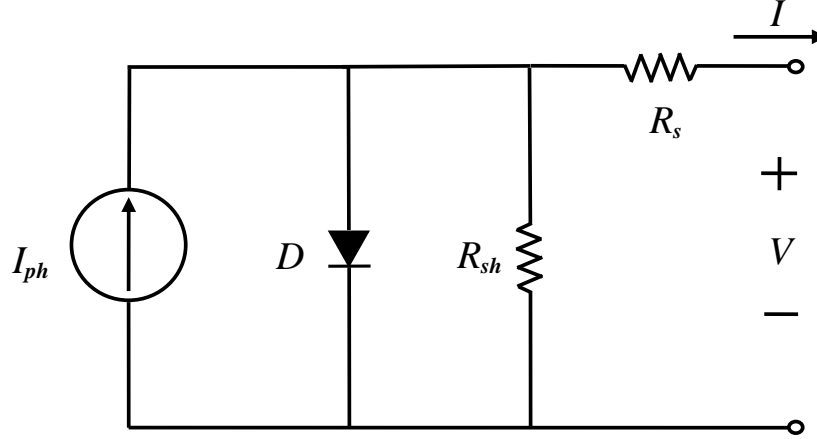
Figure 11. Single-diode model of PV solar cell.

Based on the schematic diagram, the single-diode model can be represented as

$$I = I_{ph} - I_S\left(exp\left[\frac{V + IR_s}{nV_t}\right] - 1\right) - \frac{V + IR_s}{R_{sh}} \tag{3}$$

where

$$V_t = \frac{kT}{q}, \tag{4}$$

q is the charge of an electron, n is the ideality factor, k is Boltzmann's constant, T is the temperature of the solar cell in Kelvin, and V_t is the thermal voltage at the solar cell's temperature. In addition, R_s is the series resistance of the solar cell, R_{sh} is the shunt resistance and I_s is the reverse saturation current. The photovoltaic-generated current I_{ph} is a function of temperature, solar irradiance, surface area, and the material characteristics of the solar cell. As outlined in [12]–[14], I_{ph} can be calculated from

$$I_{ph} = \left[I_{sc} + K_i\left(T - T_{ref}\right)\right]\frac{S}{1000} \tag{5}$$

16

where S is the solar irradiance in W/m^2, T is the temperature of the solar cell, T_{ref} is the reference temperature of 25 °C (298.15 K), and I_{sc} is the short-circuit current of the solar cell at a solar irradiance of 1000 W/m^2 assuming a reference temperature of 25 °C. Lastly, K_i is the short-circuit current temperature coefficient and was chosen to be 0.0017 A per °C based on [12] and [13]. Like the photo-generated current, the reverse saturation current I_s can be adjusted for temperature as well using

$$I_s = I_{s,ref} \left[\frac{T}{T_{ref}} \right]^3 exp \left[\left(\frac{T}{T_{ref}} - 1 \right) \frac{E_g}{nV_t} \right] \tag{6}$$

in accordance with [12]–[14]. Here, it must be noted that the temperature T and the reference temperature T_{ref} must be calibrated in Kelvin. Also, $I_{s,ref}$ is the reverse saturation current at the reference temperature, and E_g is the bandgap energy of the solar cell material, which is silicon in this case. The reverse saturation current I_s is a function of temperature as well as the material characteristics of the solar panel. In Table 1, the parameters that were used in this thesis to simulate the solar cell are summarized.

Table 1.   Parameters utilized for solar cell model.

Parameter	Symbol	Value
Series Resistance	R_s	0.01717 Ω
Shunt Resistance	R_{sh}	1000 Ω
Reverse Saturation Current @ 25 °C	$I_{s,ref}$	3.12x10^{-8} A
Bandgap Energy of Silicon	E_g	1.11 eV
Ideality Factor	n	1.282
Short Circuit Current Temperature Coefficient	K_i	0.0017 A per °C
Boltzmann's Constant	k	1.3806488x10^{-23} J/K
Charge of an electron	q	1.602176565x10^{-19} C

With (3) and (4), one can create a mathematical model in order to simulate a solar panel, also known as a module, or even an entire array. Of note, a solar panel or module can be defined as a collection of solar cells that are usually connected in series, and a solar array is multiple solar modules that are connected in series, parallel, or some combination. Up to this point, the model presented applies to just one solar cell. In order to have it pertain to a solar panel or an entire array of solar panels, some modifications

17

must be made. For one, it is assumed that every solar cell in the entire array experiences the same solar irradiance, temperature, and incidence angle. Additionally, one must transform the voltage V_{IN} and current I_{IN} at the terminals of the solar panel (or array) into the voltage V and current I experienced by just one cell. Since voltage is distributed equally when elements are joined in series, $V = V_{IN} \div N_s$. Also, current is spread evenly amongst components connected in parallel, so $I = I_{IN} \div N_p$. In these equations, the number of cells in series is N_s, and the number of strings of series-connected cells in parallel is N_p. With these adjustments, one can use the single cell model to simulate a solar panel (or array); hence, (3) becomes

$$I = I_{ph} - I_s \left(exp \left[\frac{\dfrac{V_{IN}}{N_s} + \dfrac{I_{IN}}{N_p} R_s}{nV_t} \right] - 1 \right) - \frac{\dfrac{V_{IN}}{N_s} + \dfrac{I_{IN}}{N_p} R_s}{R_{sh}} . \tag{7}$$

Once the new, updated current I for the solar cell is calculated from (7), the array's updated current I_{IN} can be found by multiplying I by N_p. Notice that if one is simulating just a single module (assuming all of its cells are connected in series), then N_p is equal to one. Thus, I_{IN} and I are equal. Since the solar cell is modeled as a current source, the external circuit, which is connected to the solar panel (or array), governs what the new, updated voltage V_{IN} is across its terminals. As a side note, if two or more solar panels are connected in series, which is done in some solar arrays, the voltage across each panel can be found by dividing V_{IN} by the number of panels in series. See Chapter IV and Appendix B for more details of how this model was created in Simulink.

Subsequently, one can utilize the mathematical model previously presented to create the model of the solar panel used in this thesis. To achieve this, some of the variables in Table 1 were altered multiple times until the desired electrical characteristics of the solar panel, which are displayed in Table 2, were finally obtained. Namely, R_s, n, and $I_{s,ref}$ were manipulated to obtain the correct characteristics as seen in Table 2. Of note, these characteristics represent that of the Raloss SR40-36 solar panel when tested in standard test conditions, which are 1000 W/m^2, 25℃, and an air mass of 1.5 as defined in [11].

Table 2.   Electrical characteristics of the Raloss SR40-36 solar panel, from [15].

Parameter	Symbol	Value
Open Circuit Voltage	V_{oc}	21.6 V
Short Circuit Current	I_{sc}	2.54 A
Maximum Power Point Voltage	V_{mpp}	17.0 V
Maximum Power Point Current	I_{mpp}	2.36 A

As mentioned before, the characteristics of the solar panel listed in Table 2 are achieved by adjusting the settings of the mathematical model. After that, one can create various plots of its performance under certain circumstances. For instance, one can make current versus voltage and power versus voltage plots for different levels of irradiance assuming the temperature remains constant as in Figures 12 and 13. Additionally, in Figures 14 and 15, current versus voltage and power versus voltage plots were generated for different temperature levels assuming the solar irradiance remained constant.
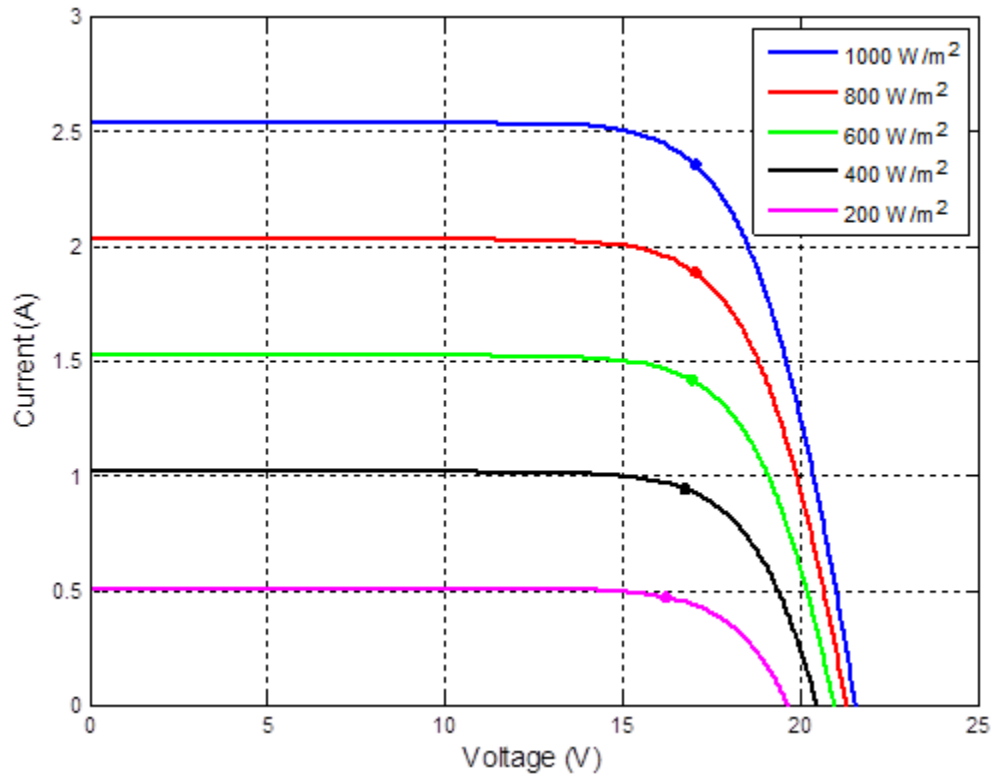
Figure 12.   Current versus voltage for varying levels of irradiance at 25 ºC.
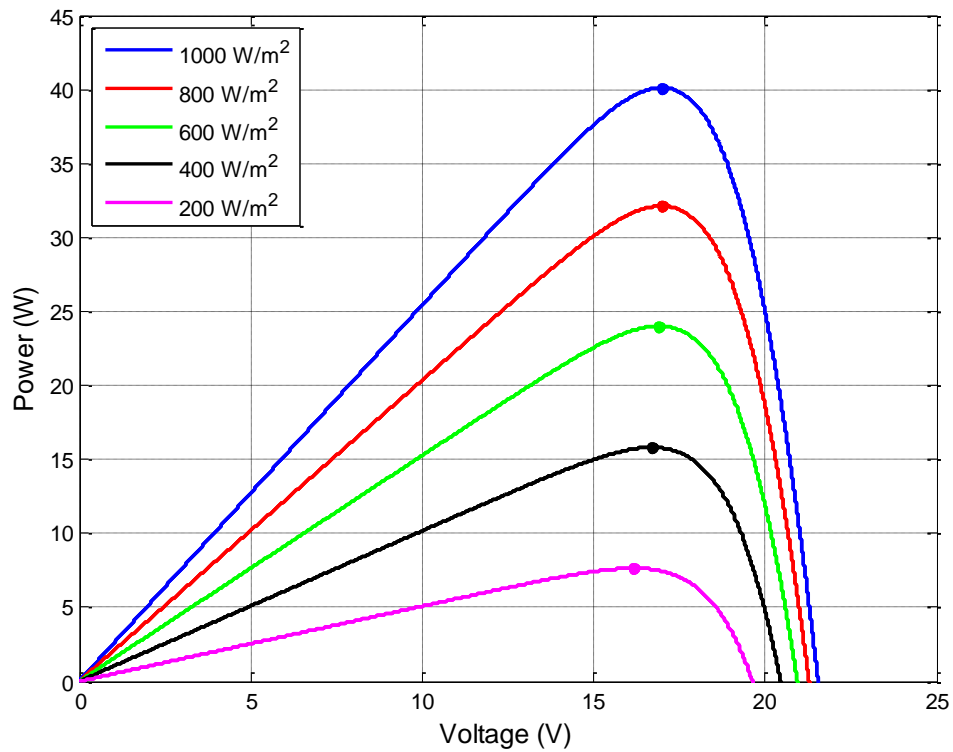
Figure 13.   Power versus voltage for varying levels of irradiance at 25 ºC.
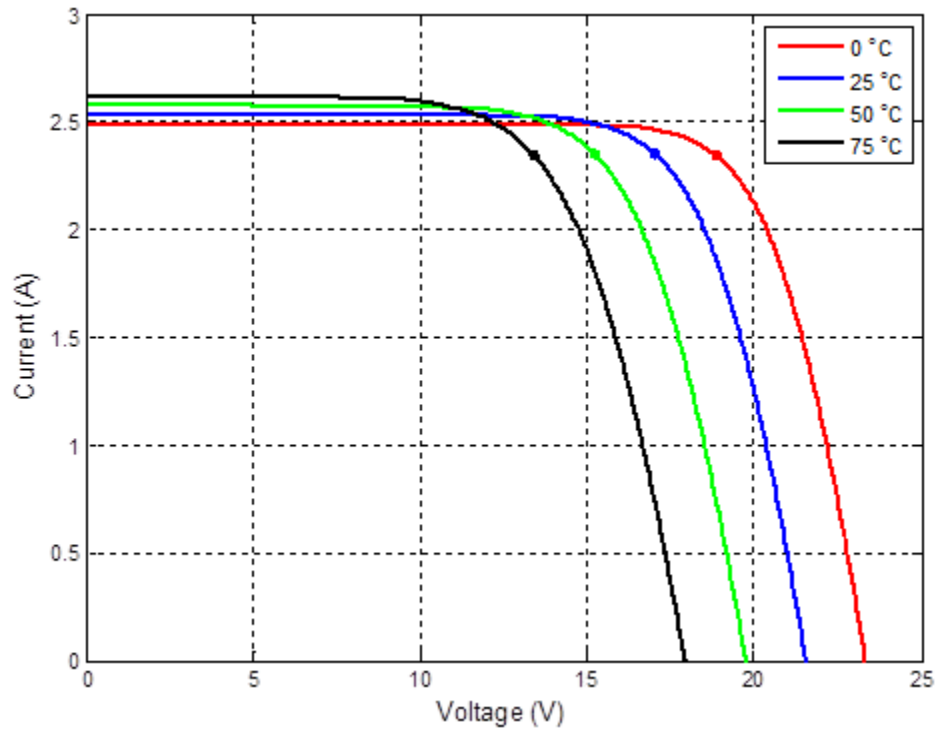
Figure 14.   Current versus voltage for varying levels of temperature at 1000 W/m^2.
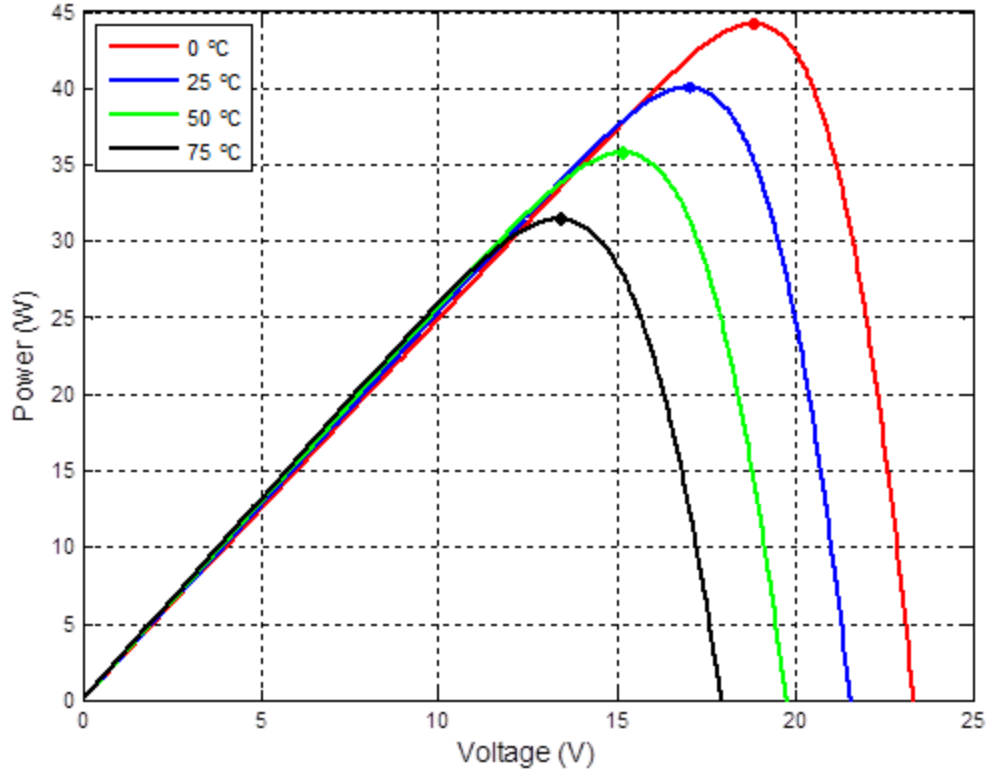
Figure 15.   Power versus voltage for varying levels of temperature at 1000 W/m^2.

On all of these plots, one can see a small dot, which denotes the MPP. The open-circuit voltage V_{oc} is found when the current is zero and is on the lower-right side of the I-V curve. The short-circuit current I_{sc} occurs when the voltage is equal to zero and is located on the far left side of the I-V curve. Examining Figures 12–15, one can make several key observations:

- The MPP occurs at the bend in the curve on the current versus voltage plot.

- To some degree, the open-circuit voltage V_{oc} and MPP voltage V_{mpp} decrease as solar irradiance decreases, and vice versa. This can be seen in Figures 12 and 13.

- Referring to Figure 12, one can observe that a change in the short-circuit current I_{sc} is directly proportional to a change in solar irradiance S. For example, when S decreases by 50%, I_{sc} decreases by 50%. This also applies to the current I_{mpp}.

- When the solar irradiance changes, the associated power at the MPP P_{mpp} varies by nearly the same percentage as seen in Figure 13. For instance, when S decreases from 1000 to 200 W/m^2, an 80% decrease, P_{mpp} decreases by almost 80% as well. In fact, it actually decreases by something slightly more than 80%.

- The slopes of the power versus voltage curve become steeper with higher levels of irradiance. This fact makes it easier to find the MPP at higher irradiance values.

- When the temperature of the solar cell increases, V_{oc} and V_{mpp} decrease noticeably as witnessed in Figures 14 and 15. These voltages change by about 0.072–0.075 V per ºC for this particular solar cell.

- Referencing Figure 14, one sees that the short-circuit current I_{sc} increases only slightly as the temperature is raised. As previously stated, I_{sc} increases by 0.0017 A per ºC when the temperature goes up.

- As temperature is varied, I_{mpp} stays about the same as is observed in Figure 14.

- As the temperature increases, P_{mpp} goes down significantly as in Figure 15. For this solar cell, P_{mpp} goes down by approximately 0.17 W per ºC.

- The slopes of the power versus voltage curve in Figure 15 stay relatively constant as temperature is changed.

B.   DC-DC POWER CONVERTER

In this portion of the thesis, the power electronics used in this research are discussed. The boost converter topology and associated mathematical equations are explained in accordance with [16]–[19]. Furthermore, several of the qualities of the interleaved boost converter as described in [20] and [21] are elaborated upon.

1.   Boost Converter

In this thesis, a DC-to-DC power converter was operated as an essential connection between the solar panel and the load. Moreover, the boost converter was selected as the baseline power converter. This power converter is the mechanism by which MPPT is achieved. One can examine the overall layout of the boost converter topology and how it interfaces with the rest of the solar PV system in Figure 16. Here, one observes that the solar panel connects to the input side of the converter while the load

and the battery connect to the output side. The battery was included in this system in order to produce a stable output voltage as well as demonstrate an energy storage capability. The values for the key components of the boost converter as well as operating parameters are listed in Table 3.
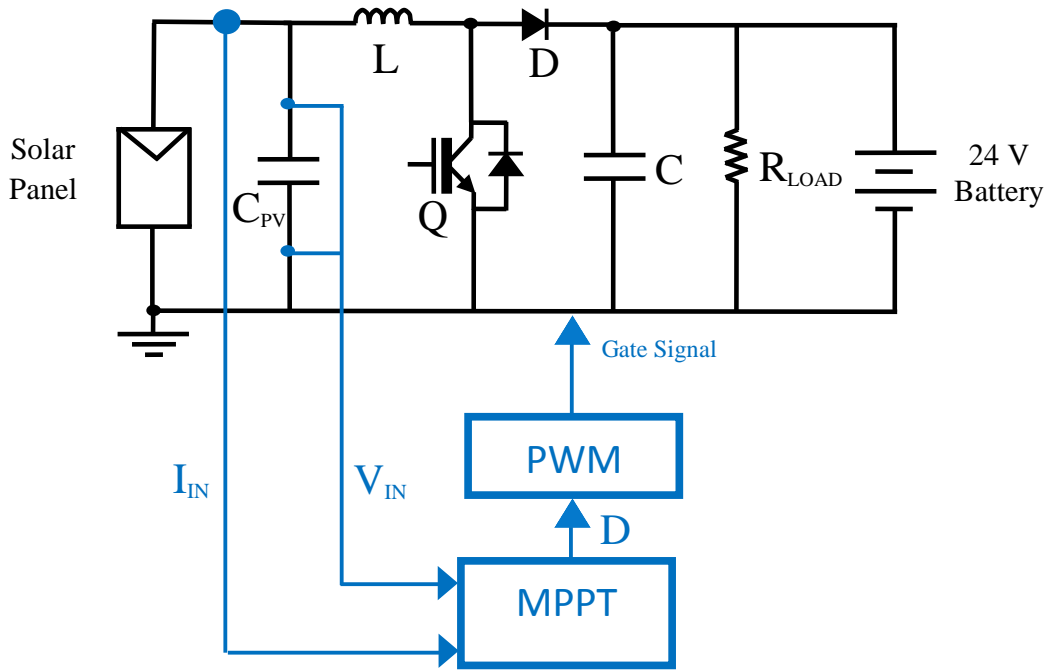
Figure 16.   Boost converter with solar panel, battery, and MPPT.

Table 3.   Boost converter parameters.

Parameter	Symbol	Value	Parameter	Symbol	Value
Input Capacitor	C_{PV}	650 μF	Input Voltage	V_{in}	14-20 V
Inductors	L	470 μH	Output Voltage	V_o	24 V
Output Capacitor	C	990 μF	Switching Frequency	f_{sw}	20 kHz
Load Resistance	R_{LOAD}	18.23 Ω	Switching Period	T_{sw}	50 μs

With so many different topologies available, one may ask, "Why the boost converter?" The following list, although not comprehensive, is presented as means to answer this question and compares the pros and cons of the boost converter with other topologies:

- The boost converter is relatively straightforward to comprehend. Certain other topologies tend to be more difficult to understand.

23

- The switch is connected to ground, which makes the insulated gate bipolar transistor (IGBT) easier to drive.

- The diode prevents current from the battery from flowing back into the solar panel and potentially causing damage [22].

- The boost converter increases the panel's voltage to that required to charge the 24 V battery; thus, it makes the panel's voltage compatible with the battery's voltage.

- A drawback of the boost converter is that it requires a ballast load [18]. If there is not at least a ballast load at the output, then the output voltage climbs excessively and damages the output capacitor.

- The boost converter can only increase the output voltage to a value that is higher than the input voltage. This fact makes the boost converter unsuitable for a system with an output voltage that is lower than the solar panel's V_{MPP}. In fact, one would want the output voltage to be, at least, slightly higher than the solar panel's V_{MPP} for control purposes.

a. ***Derivation of Parameters***

In order to gain some insight into the performance of the boost converter, the following derivation of some of its basic parameters is necessary. To simplify the derivation, the input voltage v_{IN} is assumed to be relatively constant over short periods of time since C_{PV} is large enough to handle the input ripple current. Likewise, the output voltage v_{OUT} is assumed to be relatively constant since C is large [16]. Furthermore, the resistive load and battery can be thought of as an equivalent load R, which is the output voltage v_{OUT} divided by the output current i_{OUT}. Also, for the meantime, the energy losses in the components are ignored, and the converter is assumed to operate in continuous conduction mode (CCM). CCM means that the inductor L is always conducting some current. With these assumptions in mind, one can redraw the circuit as in Figure 17.
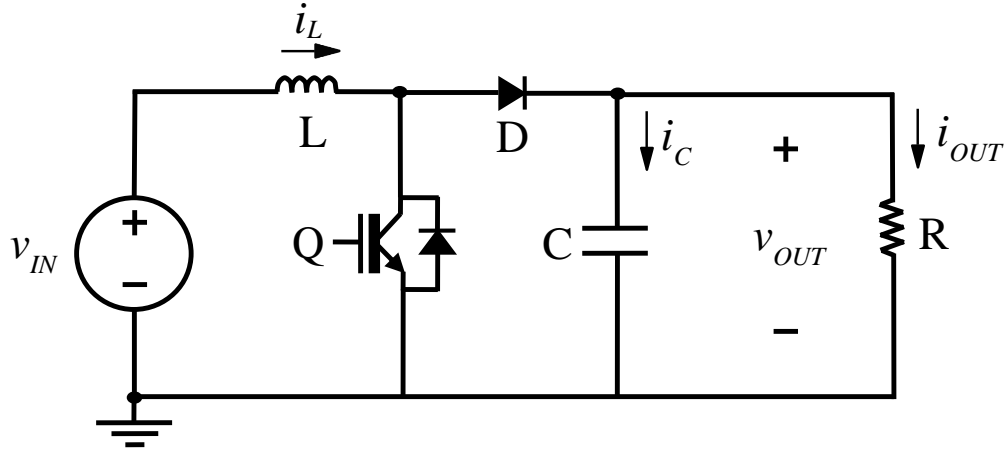
Figure 17.   Simplified boost converter schematic used for derivation, after [16].

For the regular boost converter, two different states apply – one where the transistor is on and one where the transistor is off. First, the situation where the transistor Q is on is considered. In other words, the transistor is conducting current. Additionally, it is assumed that the voltage drop across the transistor is negligible; thus, the circuit can be redrawn again as in Figure 18. Notice that the diode is not drawn in the updated circuit diagram since it does not conduct current.
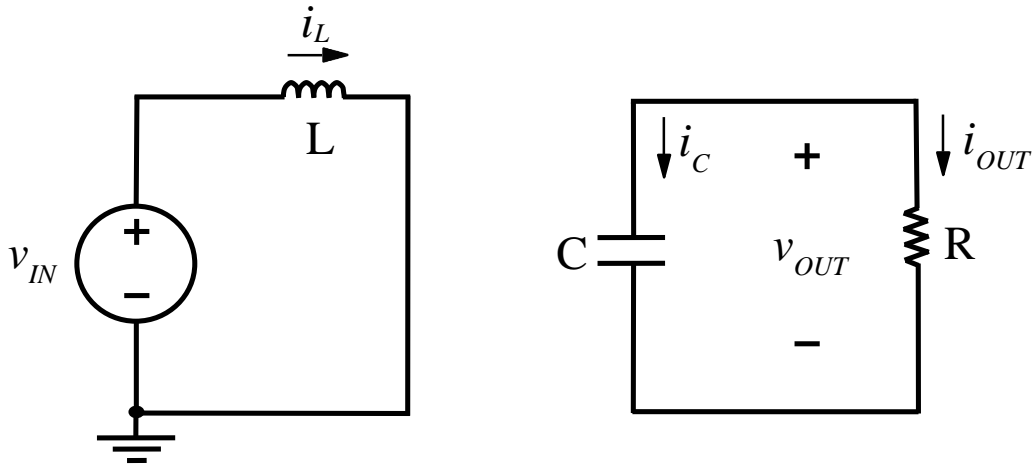
Figure 18.   Simplified boost converter schematic when transistor is on, after [16].

At this point, one can write down some basic differential equations to describe the operation of this converter. As outlined in [16]–[18],

$$v_{IN} = v_L = L \frac{di_L}{dt} \qquad (8)$$

can be found by using the left-hand side of the circuit subject to Kirchhoff's Voltage Law (KVL) and the simple definition of voltage across an inductor. Furthermore, di_L/dt can be approximated as the change in current divided by the change in time. If the change in time occurs only during the time the transistor is on, one can write

$$\frac{v_{IN}}{L} = \frac{\Delta i_L}{\Delta t} = \frac{\Delta i_L}{DT_{sw}} \qquad (9)$$

where D is the duty cycle of the transistor, and T_{sw} is the switching period. Logically, one can then obtain

$$\Delta i_L = i_{MAX} - i_{MIN} = \frac{v_{IN} DT_{sw}}{L}, \qquad (10)$$

which is a key equation that is used later to characterize the inductor current.

Next, if one looks at the right-hand side of the circuit,

$$i_C = C \frac{dv_{OUT}}{dt} \qquad (11)$$

can be established by using the basic definition of current through a capacitor. Using Kirchhoff's Current Law (KCL), one finds that i_C equals $-i_{OUT}$. Thus, one obtains

$$-i_{OUT} = C \frac{\Delta v_{OUT}}{DT_{sw}}, \qquad (12)$$

which further simplifies to

$$-\Delta v_{OUT} = -\left(v_{OUT(MIN)} - v_{OUT(MAX)}\right) = \frac{i_{OUT} DT_{sw}}{C} = \frac{v_{OUT} DT_{sw}}{RC} \qquad (13)$$

in accordance with [16]–[18]. When the transistor is on, the output voltage decreases so the Δv_{OUT} term is defined as $v_{OUT(MIN)}$ minus $v_{OUT(MAX)}$. Notice that R is the equivalent output resistance seen by the converter, as previously mentioned.

After examining the scenario where the transistor is turned on, the situation where the transistor is off is analyzed assuming CCM. In Figure 19, the equivalent circuit has been drawn with the diode missing since it is assumed that its voltage drop is negligible.

26

Also, since the transistor is off and not conducting, it was removed from the circuit as well.
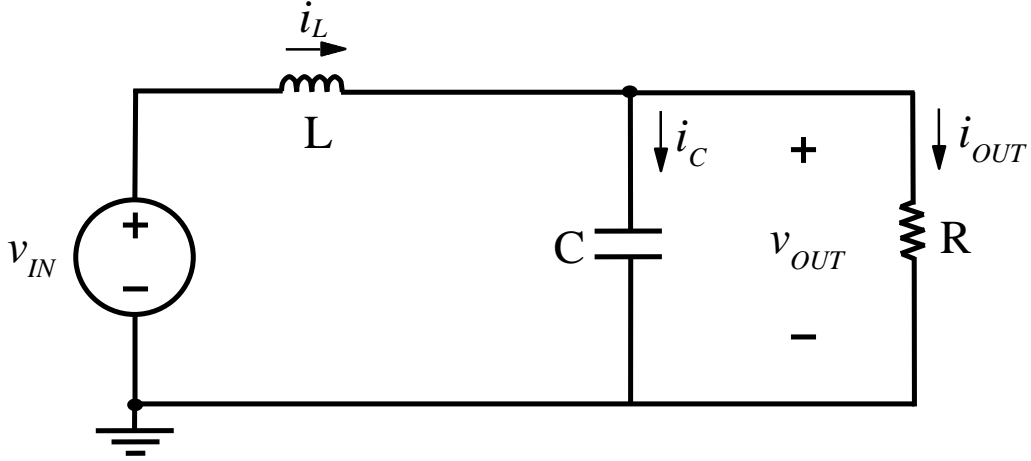
Figure 19.   Simplified boost converter schematic when transistor is off, after [16].

Initially, looking at the left-hand side of the circuit, one can use KVL to find

$$v_{IN} = v_L + v_{OUT} = L\frac{di_L}{dt} + v_{OUT},$$ (14)

which is approximated as

$$v_{IN} = L\frac{\Delta i_L}{(1-D)T_{sw}} + v_{OUT}.$$ (15)

Here, the *dt* term becomes *(1–D)T* since it refers to the time when the transistor is off. Rearranging terms, one gets

$$-\Delta i_L = -\left(i_{MIN} - i_{MAX}\right) = \frac{v_{OUT} - v_{IN}}{L}(1-D)T_{sw}.$$ (16)

Additionally, in the state where the transistor is off, the current in the inductor decreases so the Δi_L term is defined as i_{MIN} minus i_{MAX}. Setting the right sides of (10) and (16) equal to each other and doing some algebra yields

$$\frac{v_{OUT}}{v_{IN}} = \frac{1}{1-D},$$ (17)

which is in accordance with [16]–[18].

27

Subsequently, the right-hand side of the circuit in Figure 19 is analyzed. At this point, one can use KCL to sum the currents and produce

$$i_L = i_{OUT} + i_C = \frac{v_{OUT}}{R} + C\frac{dv_{OUT}}{dt}. \tag{18}$$

After a little manipulation, one gets

$$\frac{dv_{OUT}}{dt} = \frac{1}{C}\left[i_L - \frac{v_{OUT}}{R}\right], \tag{19}$$

which can also be written as

$$\Delta v_{OUT} = v_{OUT(MAX)} - v_{OUT(MIN)} = \frac{1}{C}(1-D)T_{sw}\left[i_L - \frac{v_{OUT}}{R}\right]. \tag{20}$$

If one equates the result in (20) to (13) and does a little arithmetic, one obtains

$$i_L = \frac{v_{OUT}}{R(1-D)}, \tag{21}$$

which is the average inductor current [16]. One can also write (21) as

$$i_L = \frac{v_{IN}}{R(1-D)^2} \tag{22}$$

by substituting in (17). Assuming the converter is operating in CCM, one adds half of Δi_L from (10) to (22), which gives

$$i_{MAX} = \frac{v_{IN}}{R(1-D)^2} + \frac{v_{IN}}{2L}\frac{DT_{sw}}{2L} \tag{23}$$

as shown in [15]. Likewise, subtracting half of Δi_L from (10) to (22) gives

$$i_{MIN} = \frac{v_{IN}}{R(1-D)^2} - \frac{v_{IN}}{2L}\frac{DT_{sw}}{2L}. \tag{24}$$

If one sets the i_{MIN} term equal to zero and solves for L, one gets

$$L_{crit} = \frac{RDT_{sw}}{2}(1-D)^2, \tag{25}$$

which is the critical inductance [16]–[18]. The critical inductance is the inductance where the converter operates on the border of CCM and discontinuous mode (DCM) [16]–[18]. In other words, the inductor is always conducting except for one small instant in time when its current reaches zero. After that moment, the inductor current does not remain at zero as in DCM but begins to climb again. Also, one can use (24) to solve for

28

$$R_{crit} = \frac{2L}{DT_{sw}(1-D)^2} \, , \tag{26}$$

which is the critical resistance. If the output resistance R gets larger than the critical resistance R_{crit}, the converter is forced into DCM.

Using some of these relationships, one can also solve for the ripple in the input voltage; however, the method to do so is more intuitive. First, consider the definition for the current through the input capacitor,

$$i_{C_{pv}} = C_{pv} \frac{dv_{IN}}{dt} \, . \tag{27}$$

One can take the integral of both sides and rearrange this formula to produce

$$\Delta v_{IN} = v_{IN}(t_2) - v_{IN}(t_1) = \frac{1}{C_{pv}} \int_{t_1}^{t_2} i_{C_{pv}} \, dt \, . \tag{28}$$

If one can integrate the input capacitor current over the correct time interval, then one can determine the ripple in the input voltage. Furthermore, one can see that there is an equal amount of area above and below the $i_{Cpv} = 0$ line by analyzing the input capacitor current waveform shown in Figure 20. Based on this plot, notice that this waveform makes a triangle when the current is positive (shaded in light blue). Thus, one just has to find the area under the input capacitor current curve by using the geometry of a triangle. The base of the triangle is given by the time that the current is positive and is half of T_{sw}. The height of the triangle is determined by the change in current, which is given by dividing the change in the inductor current Δi_L from (10) by two. Multiplying these two quantities together and dividing by $2C_{pv}$, one obtains the relationship,

$$\Delta v_{IN} = \left(\frac{1}{2}\right)\left(\frac{T}{2}\right)\left(\frac{v_{IN}DT_{sw}}{2L}\right)\left(\frac{1}{C_{pv}}\right) = \frac{v_{IN}DT_{sw}^{\,2}}{8LC_{pv}} \, . \tag{29}$$
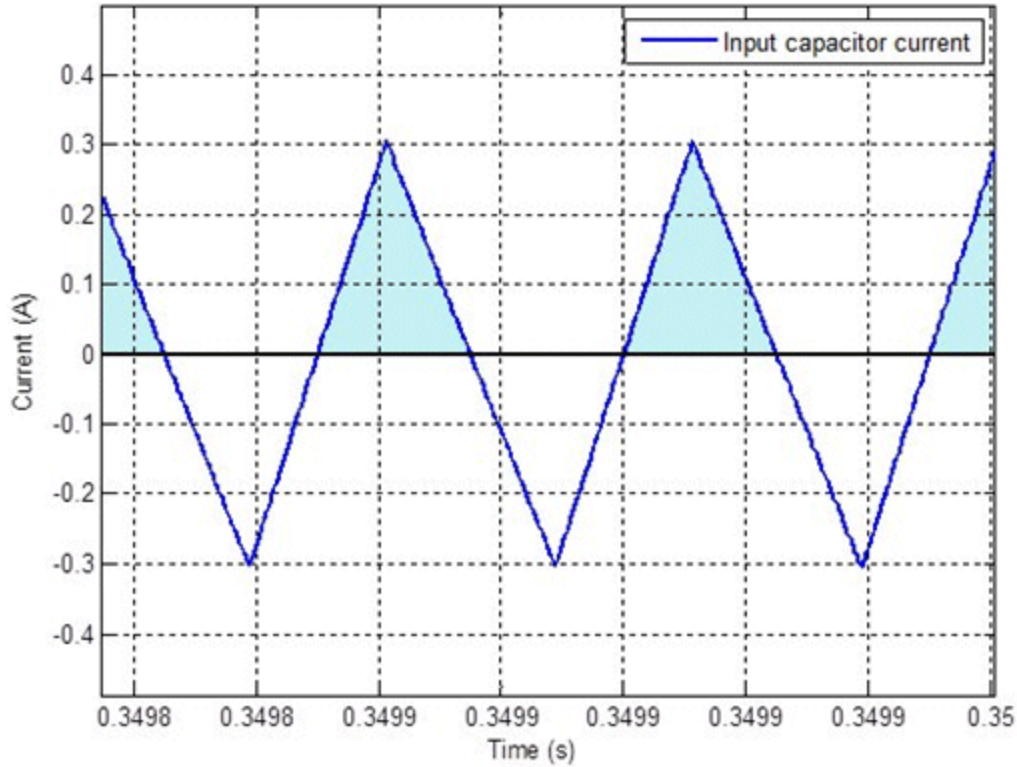
Figure 20.   Input capacitor current versus time.

b.   *Performance of the Boost Converter*

The equations presented in the preceding section are used to characterize the performance of the boost converter. It must be noted that these equations assumed zero losses in the circuit. While this approach may seem completely impractical, these computations are sufficiently close to the simulated and experimental results to be useful. Typically, the performance specifications are identified and then one solves for the components that make them possible. In this thesis, the opposite was done. The component values were already known, and the performance parameters were found via calculations.

In order to validate the boost converter's performance, the following example is given and is later compared to the simulation results in Chapter IV. Consider the situation where the converter is operating in CCM and is getting 35.77 W from the solar panel when at the MPP. Also, the converter's input voltage and current are 15.131 V and 2.364 A, respectively. The output voltage is 23.99 V, and, assuming zero losses, the output

current must be 1.491 A. Equation (17) is used to solve for the theoretical duty cycle, which is about 0.3693. Additionally, the theoretical equivalent resistance R is 16.09 Ω. Using (10), one estimates the change in the inductor current Δi_L to be 594.4 mA (peak-to-peak), or roughly 0.6 A. Likewise, the ripple in the output voltage Δv_{OUT} was found to be 27.8 mV using (13). Other values are found using the equations contained in the previous section, and these theoretical calculations are summarized in Table 4.

Table 4.   Theoretical Performance Parameters for the Boost Converter.

Parameter	Symbol	Value
Ripple in inductor current	Δi_L	594.4 mA
Ripple in output voltage	Δv_{OUT}	27.8 mV
Ripple in input voltage	Δv_{IN}	5.72 mV
Average inductor current	$i_{L(AVG)}$	2.364 A
Maximum inductor current	i_{MAX}	2.661 A
Minimum inductor current	i_{MIN}	2.067 A

The critical inductance L_{crit} and critical resistance R_{crit} terms were found for a worst-case scenario. Here, the duty cycle was assumed to 1/3, which is the value that maximizes the $D(1-D)^2$ term in (25) and (26) [17]. Also, the resistance was found by assuming that the input current was only 1/5 of what it had been, or 472.8 mA. Consequently, the output current is 315.2 mA since $i_{OUT} = (1-D)\ i_{IN}$. Since v_{OUT} is essentially 24 V, R equals 76.14 Ω. With that, the L_{crit} was found to be 282.5 μH, and R_{crit} was calculated to be 126.9 Ω.

As mentioned earlier, the efficiency of this converter was not 100%; thus, the values above are approximations. If one takes into account power losses, then one finds that these values change slightly. As outlined in [19], the duty cycle is better approximated with,

$$D = 1 - \frac{v_{IN}}{v_{OUT}}\eta \tag{30}$$

where η is the efficiency of the converter. It is important to note that this value for the duty cycle D was found with a different set of assumptions; thus, it cannot be used in the

previously derived equations. Using (30) with an efficiency of 86%, one finds the duty cycle to be 0.4576.

2. Interleaved Boost Converter

One of the main focuses of this thesis was to employ the interleaved boost converter as the primary power converter topology. In [20] and [21], this layout is chronicled extensively, where the interleaved topology consists of two parallel circuits – each with an inductor, a diode, and a semiconductor switch. This topology is used to control the power from the solar panel just like the regular boost converter but essentially involves two boost converters that are placed in parallel as shown in Figure 21. Each of these boost converters are fundamentally operated the same with the identical duty cycles except that the timing of their operation is precisely synchronized; thus, each parallel converter creates a current, which is interleaved to produce a total current to the load. Furthermore, each boost converter can be thought of as a separate phase of the IBC.
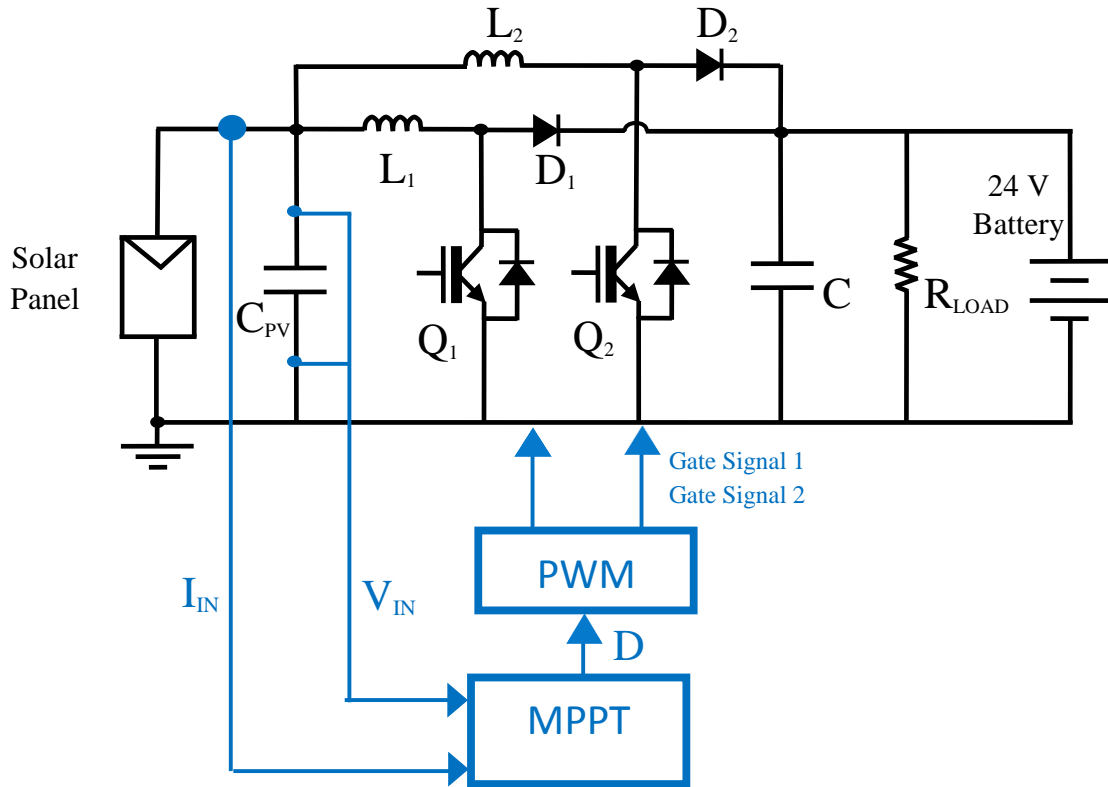
Figure 21.   Interleaved boost converter with solar panel, battery, and MPPT.

In Figure 22, the inductor currents are plotted for a time interval when the IBC is operating in continuous conduction mode. Here, one can see that the individual inductor currents look very much the same as the regular boost converter; however, they are shifted in time by half the switching period, or $T_{sw}/2$. Thus, to control a dual-phase IBC, one must separate each of the gating signals to the semiconductor switches by half of the switching period. In addition, one can interleave more than just two phases. In Figure 23, the inductor currents for a four-phase IBC are displayed; however, this topology was not used in this thesis. Here, it can be seen that the current for each phase has to be time-shifted by one quarter of the switching period. The STEVAL-ISV009V1 is a four-phase IBC, which uses the SPV1020 chip, and is produced by STMicroelectronics [23].
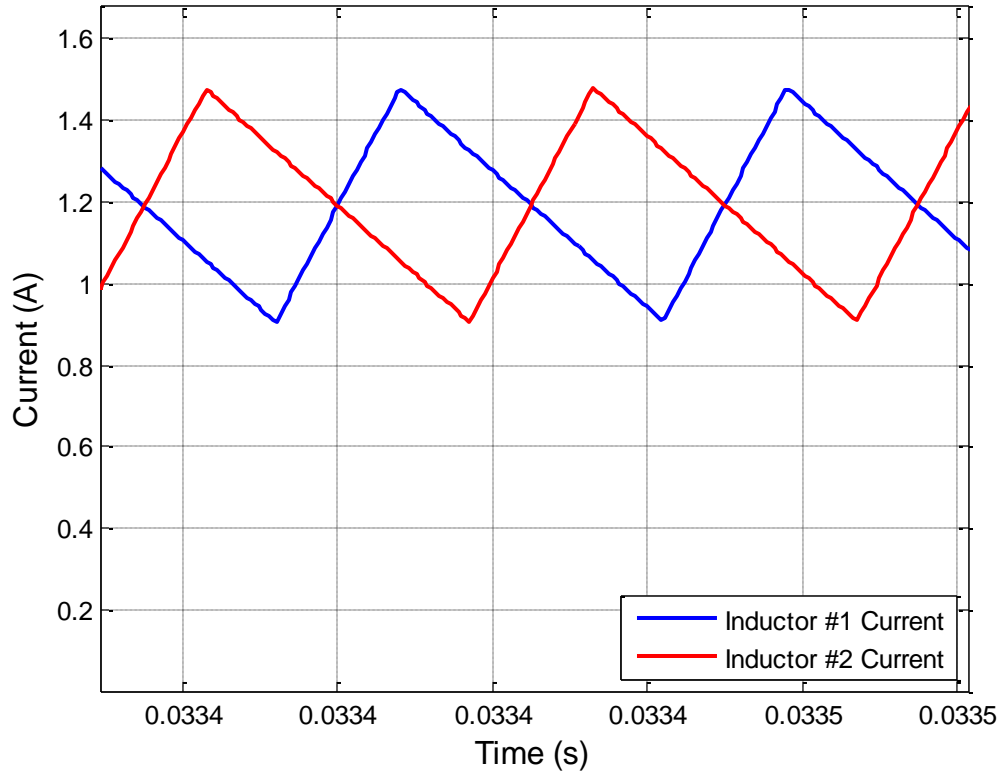
Figure 22.   Inductor currents versus time for an IBC with two phases.
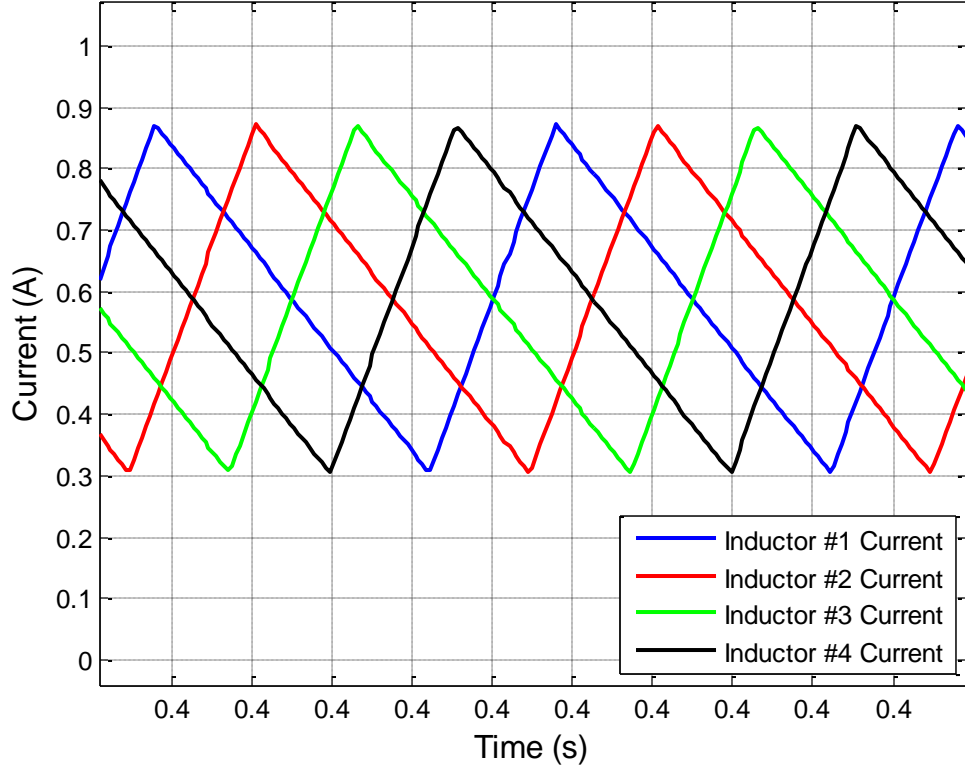
Figure 23.   Inductor currents versus time for an IBC with four phases, after [23].

a.   *Four States of the IBC while in CCM*

With the regular boost converter, there are only two possible states. Either the switch is conducting or the diode is conducting. Since the interleaved boost converter has two separate phases, there are several modes, or states, in which it can operate [21]. For the purposes of this discussion, it is assumed that the converter is in CCM. In Figure 24, the currents for both inductors is illustrated when the duty cycle is within the interval $0.00 < D < 0.50$ [21]. To be specific, the duty cycle here is 0.24. In this plot, one may notice that there are distinct moments in time where the converter is conducting current through the inductors in a specific way. In particular, the inductors are either in a state where they are charging, denoted by an increasing current, or they are in a state where they are discharging, denoted by a decreasing current. Also, the states that the IBC transitions through are labeled on this plot. To further this discussion, the same assumptions that were made about the regular boost converter in the previous section are

now adopted; hence, one can make a simplified schematic for the IBC as displayed in Figure 25.
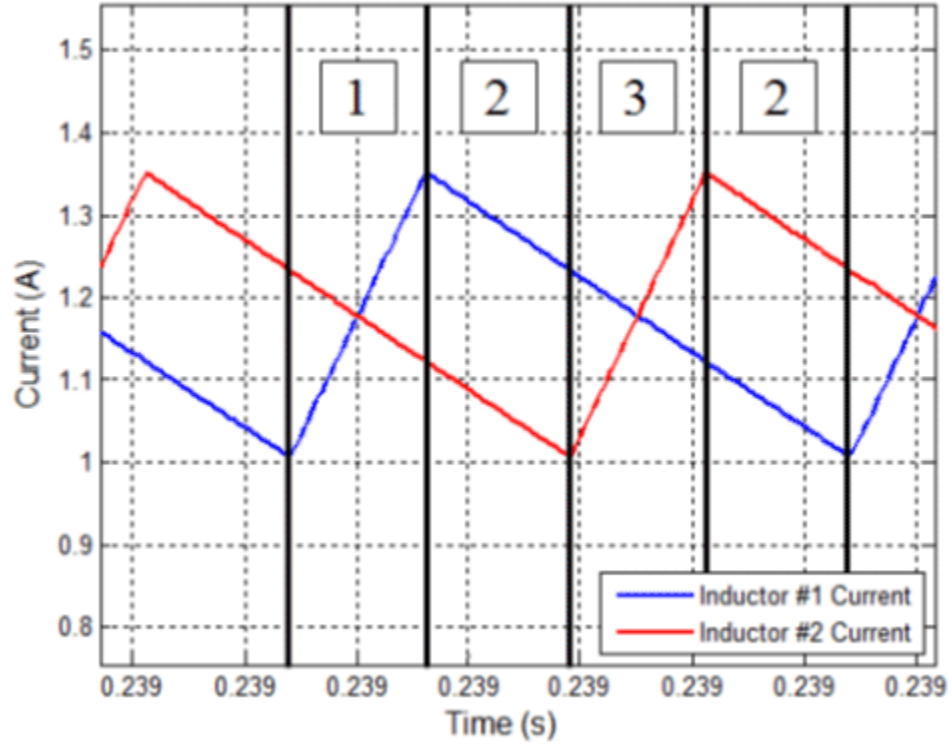
Figure 24.   States of the IBC illustrated in the inductor currents.
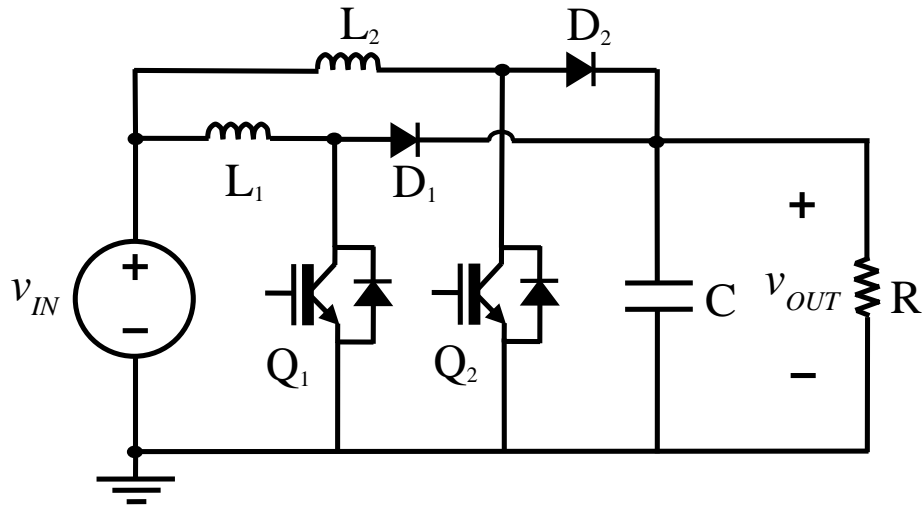
Figure 25.   Simplified interleaved boost converter schematic.

35

Next, each state is briefly discussed so that one may further understand how the IBC works. In addition, the schematic from Figure 25 is modified to show only the conduction paths for each state.

(1)   State 1: Q_1 is on, D_1 is off, Q_2 is off, and D_2 is on.

In state 1, the current in inductor #1 is rising and the current in inductor #2 is falling. In Figure 26, the schematic shows the paths that are conducting electricity. As one can see, the individual inductors are connected to the source in much the same way as the regular boost converter; however, in state 1, the output side is only connected to the source via phase 2 as seen by the conduction path made by inductor #2 and diode #2.
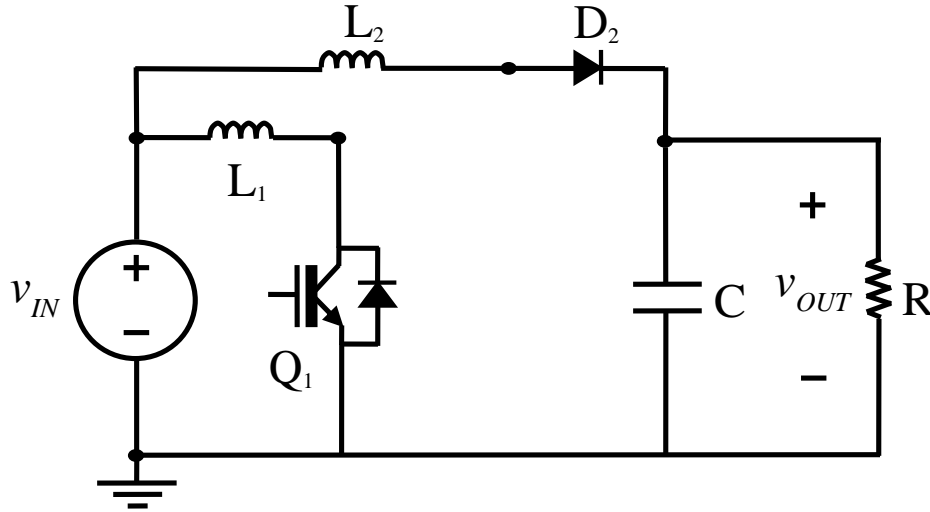
Figure 26.   IBC in State 1.

(2)   State 2: Q_1 is off, D_1 is on, Q_2 is off, and D_2 is on.

Once switch Q_1 turns off, the converter enters into state 2. In state 2, both inductor currents are decreasing since both switches are off. In Figure 27, one can see the conduction paths when both switches are off. Here, the output side is connected to the source via both inductor and diode pairs from phase 1 and 2; therefore, the current flowing into the output from both of these phases sums to be something significantly greater than the current flowing from just a single phase.
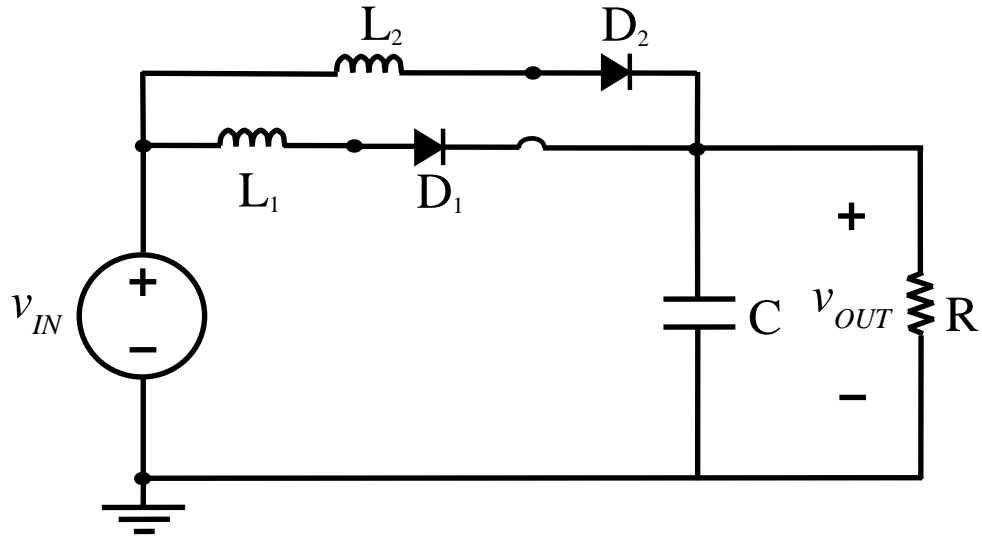
Figure 27.   IBC in State 2.

(3)   State 3: Q_1 is off, D_1 is on, Q_2 is on, and D_2 is off.

Subsequently, when switch Q_2 is turned on, the converter enters into state 3. One must realize that this happens exactly when switch Q_1 is at the halfway point of its switching period. State 3 is the same thing as state 1 except that the roles for each phase are reversed; thus, the current in inductor #2 is rising and the current in inductor #1 is falling. One can see what this role reversal looks like in Figure 28.
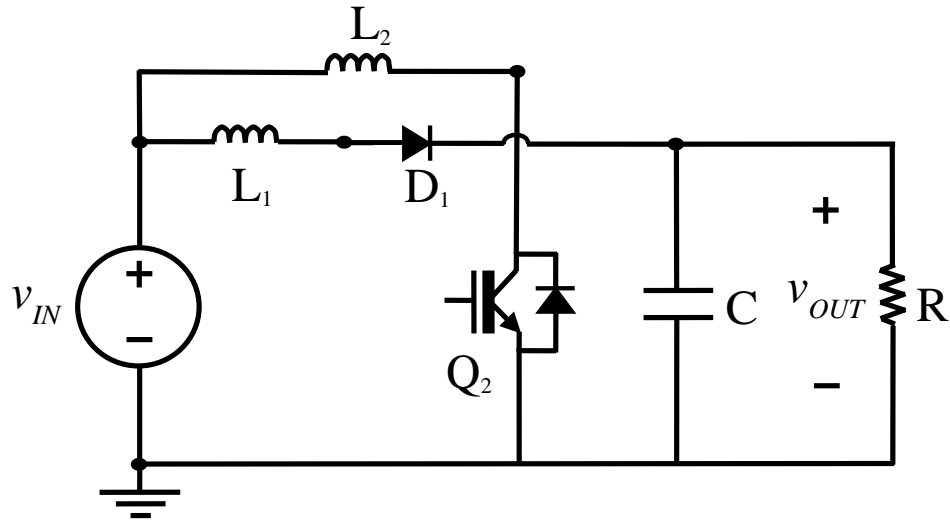
Figure 28.   IBC in State 3.

Notice that the schematic is essentially the same as Figure 26, but the conduction paths have traded places. Now, the output side is connected to the source via the inductor and diode in phase 1.

(4)   State 4: Q_1 is on, D_1 is off, Q_2 is on, and D_2 is off.

State 4 is only possible when both switches are on at the same time. Consequently, the current in both inductors is rising at the same time while in this state. The only time the IBC can do that is when the duty cycle D is within the interval, $0.50 < D < 1.00$. This mode was not experienced much in this thesis research. Based on the equivalent load resistance, the inductance value, and the fact that the converter operated in CCM, its duty cycle rarely exceeded 0.50. In addition, the output side is not connected to the input side as it was in the other states, and this can be observed in Figure 29; thus, state 4 is the only state in CCM where the output capacitor solely has to provide current to the load. Furthermore, during discontinuous conduction mode, the converter can be in additional states. This is not discussed since the focus of this thesis is the converter's operation while in continuous conduction mode.
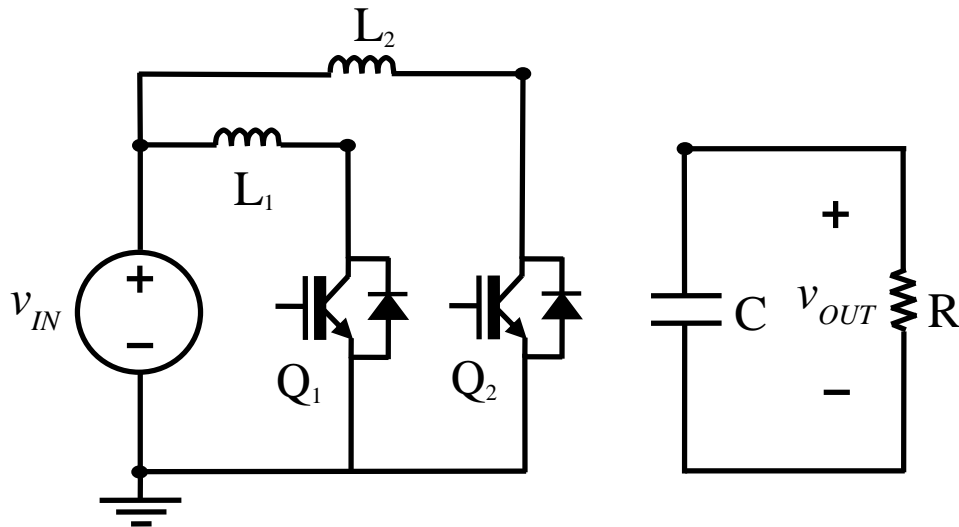
Figure 29.   IBC in State 4.

b. *Performance of the Interleaved Boost Converter*

Now that each state of the IBC has been briefly explained, one can make some inferences with respect to the performance of the IBC. Of note, the values for each component of the IBC were the same as the regular boost converter and are listed in Table 3. Remarkably, the change in current for each individual inductor remains the same. Equation (10) does not change from the perspective of each inductor; however, when one sums the current waveforms for each inductor, it is apparent that some very interesting things happen. In Figure 30, one can see the sum of the inductor currents in relation to the original plot of both currents.
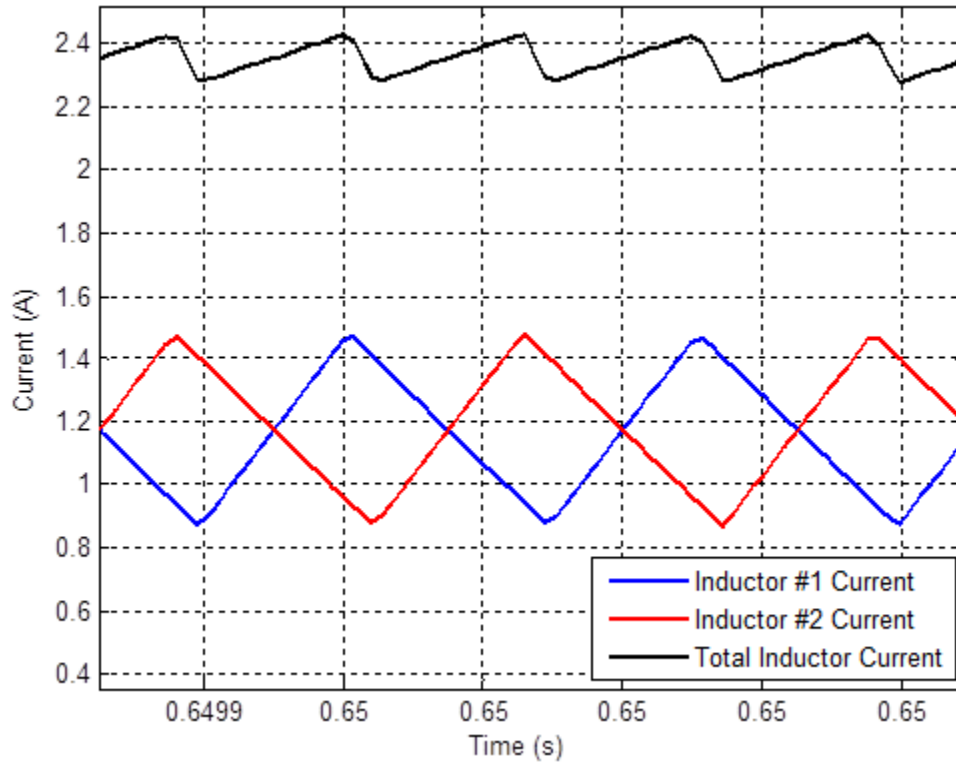
Figure 30.   Sum of the currents from inductor #1 and inductor #2.

The current ripple of the total inductor current is smaller than the ripple associated with each individual inductor. The amount of total inductor current ripple not only depends upon the input voltage and inductance value as it did in the regular boost converter but also on the relative timing between the individual inductor current

waveforms. In other words, the duty cycle as well as the phase shift between the two currents can alter the amount of total inductor current ripple significantly [20], [21]. This is because the ripple current in each phase tends to cancel each other out to some degree depending on the duty cycle value [20], [21]. According to [20] and [21], the ripple is at a minimum when the duty cycle is set to 50%.

The average current in the total current waveform is twice the average current of each inductor. In other words, the average inductor current for each phase is half of what it was previously when analyzing the regular boost converter [20], [21]. It is important to note that the average total inductor current of the IBC is the same as the average inductor current of the regular boost converter. Furthermore, the factor of two is absent in the critical inductance and critical resistance equations based on these revelations. Thus, (22)–(26) become

$$i_{L(per\ phase)} = \frac{v_{IN}}{2R(1-D)^2}, \tag{31}$$

$$i_{MAX} = \frac{v_{IN}}{2R(1-D)^2} + \frac{v_{IN}}{2L}DT_{sw}, \tag{32}$$

$$i_{MIN} = \frac{v_{IN}}{2R(1-D)^2} - \frac{v_{IN}}{2L}DT_{sw}, \tag{33}$$

$$L_{crit} = RDT_{sw}(1-D)^2, \tag{34}$$

and

$$R_{crit} = \frac{L}{DT_{sw}(1-D)^2}. \tag{35}$$

With these updated equations, one can now determine some of the performance parameters associated with the IBC, which are shown in Table 5. The ripple for the input and output voltages are not determined. This is because, with the interleaved boost converter, the ripple not only depends upon the component values and the duty cycle but also depends upon the interleaved phasing of the currents. As mentioned previously, the timing of the currents has a tendency to cancel out the ripple as the duty cycle approaches 50%; however, it is difficult to produce a closed-form equation that yields the input and output voltage ripples. Also, assuming the same worst-case scenario used for the regular boost converter, one discovers that L_{crit} and R_{crit} are 565 µH and 63.45 Ω, respectively.

Table 5.   Theoretical Performance Parameters for the IBC.

Parameter	Symbol	Value
Ripple in inductor current	Δi_L	594.4 mA
Ripple in output voltage	Δv_{OUT}	Not determined
Ripple in input voltage	Δv_{IN}	Not determined
Average inductor current	$i_{L(per\,phase)}$	1.182 A
Maximum inductor current	i_{MAX}	1.479 A
Minimum inductor current	i_{MIN}	0.885 A

c.   Benefits of the IBC

So far, some of the attributes of the interleaved boost converter have been explained in detail. In this section, the advantages of the IBC are highlighted further. Theoretically, the IBC is more efficient since it has fewer conduction losses as compared to a single boost converter; however, the losses due to the switching action remain the same. To understand why this is, first, examine Figure 31, which illustrates the concept of switching losses. Based on Figure 31, the power losses due to switching is characterized by

$$P_{sw} = \frac{1}{2} V_{off} I_{on} \left(t_{sw(on)} + t_{sw(off)} \right) f_{sw}, \tag{36}$$

where I_{on} is the average current conducting through the switch when it is on, and V_{off} is the average voltage across the switch when it is turned off [17], [18]. The symbols $t_{sw(on)}$ and $t_{sw(off)}$ are the time it takes to turn the switch on and the time it takes to turn the switch off, respectively [17]. This equation can be extended to the switching action across either the transistor or the diode, but one must realize that the values used in the equation will be somewhat different since one is dealing with different components. If one thinks about the switching losses across one single switch in the IBC, one realizes that the average current is half of what it was in the regular boost converter; thus, the switching losses associated with that particular switch are also cut in half. In the IBC, there is twice the number of switching components as compared to the regular boost converter; therefore, while the switching losses of a single component are half of what they are in the regular boost converter, the total switching losses remain the same.
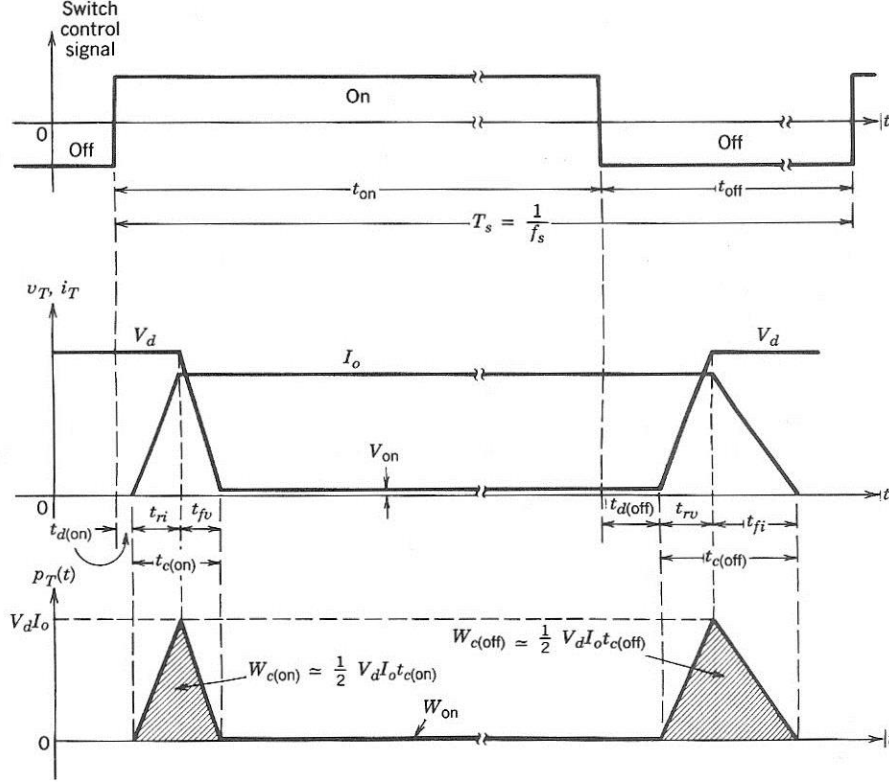
Figure 31.   Switching losses, from [17].

As stated previously, the conduction losses are significantly less for the IBC than for the regular boost converter. In (37) and (38), the conduction losses are summarized as

$$P_{conduction} = \left(V_F I_{on} + I_{on}^2 R_{sw}\right) D + I_L^2 R_L \tag{37}$$

where

$$V_{on} = V_F + I_{on} R_{sw}, \tag{38}$$

V_F is the nominal forward voltage drop across the switch when it is barely conducting, R_{sw} is the on-state resistance associated with the switch, I_L is the average current in one of the inductors, and R_L is the resistance of that inductor [17], [18], [21]. Examining the conduction losses in (37), one sees that there are a few I^2R terms. These terms represent the power losses due to the level of current conduction. If the current goes up, the power losses associated with these components also goes up. Since there is only half of the current in each phase of the IBC, the I^2R losses go down by a factor four as compared to the regular boost converter. As stated previously, the number of switching components in the IBC is twice that of the regular boost converter; therefore, when using a two-phase

42

IBC, the I^2R losses are only half of what they are for the regular boost converter. This is the main reason why the IBC is more efficient. The reduction in the inductor's AC losses is also a reason for the increased efficiency, but that is not examined in this thesis [20].

Another key feature of the interleaved boost converter is the fact that the output voltage and current do not have as much ripple as the regular boost converter. Through simulation, the output behavior of a regular boost converter was compared to that of the IBC. The simulated waveforms in Figures 32 and 33 demonstrate that the IBC's output ripple is significantly reduced compared to a regular boost converter. In particular, the regular boost converter has an output voltage ripple of about 29.2 mV, while the IBC has a ripple of 3.7 mV. Also, the regular boost converter has an output current ripple of about 192 mA, while the IBC has a ripple of 24 mA. This is essentially a decrease in the output ripple by a factor of eight. Note that this was when the converter was operating in CCM with a duty cycle of around 45%.
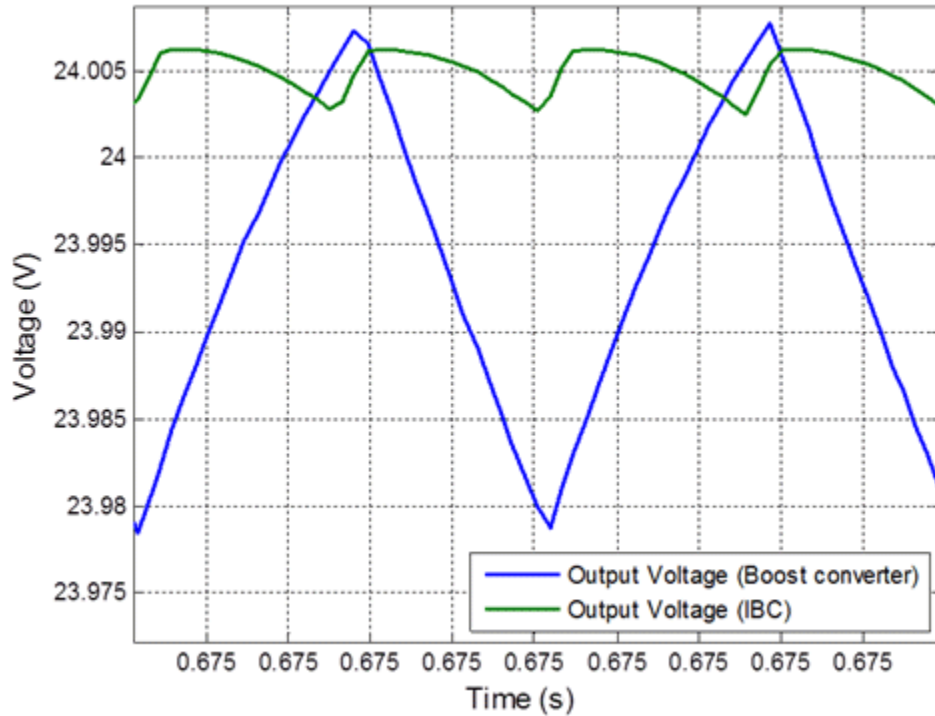
Figure 32.   Output voltage ripple of the boost converter (blue) and the IBC (green).
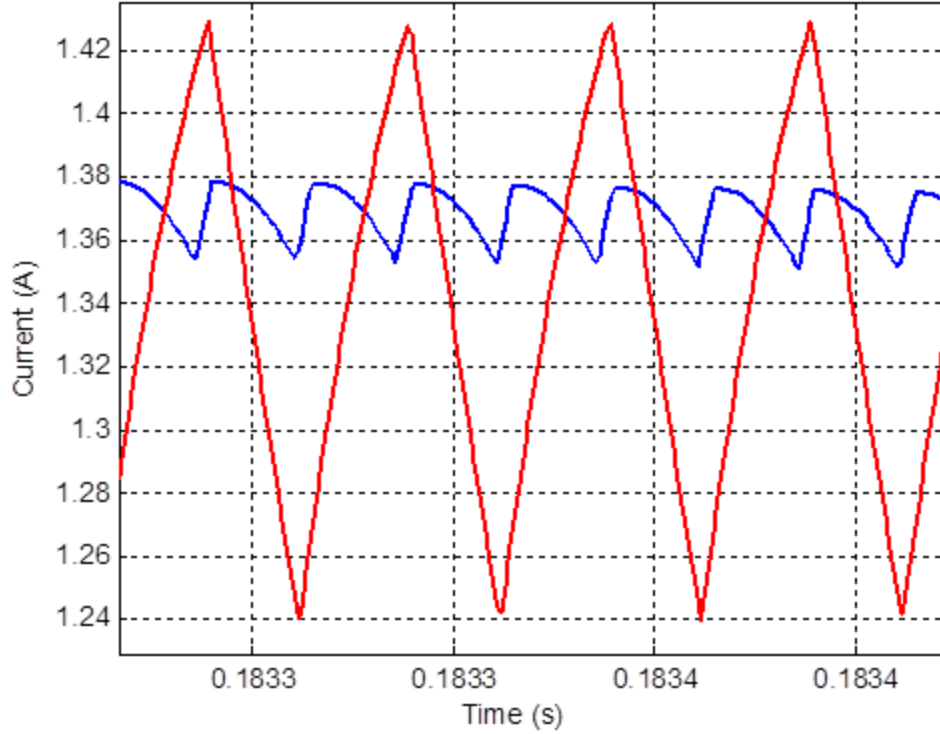
Figure 33.   Output current ripple of the boost converter (red) and the IBC (blue).

From Figures 32 and 33, one can also notice that the waveforms associated with the IBC have twice the frequency when compared to the regular boost converter. Also, in Figure 30, the frequency of the total current waveform is twice that of each individual inductor.

C.   MAXIMUM POWER POINT TRACKING

In this thesis, two of the most prevalent MPPT algorithms, perturb and observe as well as incremental conductance, were used to control the converter and solar panel so that the panel operated at its MPP. The logic within these algorithms determines the state of the solar panel's power in relation to its voltage and then decides how to modify the control parameters in order to find the MPP. Once the algorithm determines what needs to be done, there are several variables that can be controlled to force the system to the MPP. The basic theory behind maximum power point tracking is described in this section, and several of the most widely used MPPT algorithms are explained. Lastly, the

44

different ways a power converter's duty cycle can be modified in order to implement these algorithms is discussed.

1.   Perturb and Observe

Perturb and observe is probably the most commonly utilized MPPT method [24]. The basic premise for P&O is to continually perturb or alter the power converter's operating point and then to observe or sense the ensuing effects. In other words, the settings within the converter are changed so that the solar panel's voltage and current are changed. Then, the system senses the panel's voltage and current to see if its power has increased or decreased. Subsequently, the algorithm makes a decision on how to further adjust the converter's settings. Typically, the settings that are modified are either a reference voltage or the duty cycle. A reference current may also be used, but this method is less common for reasons that are explained later.

In Figure 34, the P&O flowchart is presented in order to understand the finer details of this algorithm. As one can see from Figure 34, the algorithm reads in the voltage measurements $V[k]$ and the current measurements $I[k]$ at a specified time interval called the MPPT period. This time interval governs how often the algorithm makes a decision to change the operating point of the system. Subsequently, the algorithm calculates the power $P[k]$, the change in power ΔP, and the change in voltage ΔV. The ΔP and ΔV values are found by using the measurements at the present moment $V[k]$ and $I[k]$ as well as the previous measurements $V[k-1]$ and $I[k-1]$. From there, the algorithm uses basic logic in order to decide what to do. The ΔP and ΔV values are each compared against zero to determine if they have increased or decreased. Next, if one uses an XNOR logic gate, this decision is relatively simple as shown in Table 6. Here, a "0" constitutes a false answer to the logic, while a "1" represents a true answer. For example, in the input columns of Table 6, a "0" means that the quantity has decreased and a "1" means that the quantity has increased. The output column is the logical result of the XNOR gate, and this is used to drive either the duty cycle or the reference voltage according to the algorithm. To summarize, if the power goes up after a certain perturbation, then the next

perturbation should remain unchanged; however, if the power goes down, then the ensuing perturbation should be in the opposite direction [25].
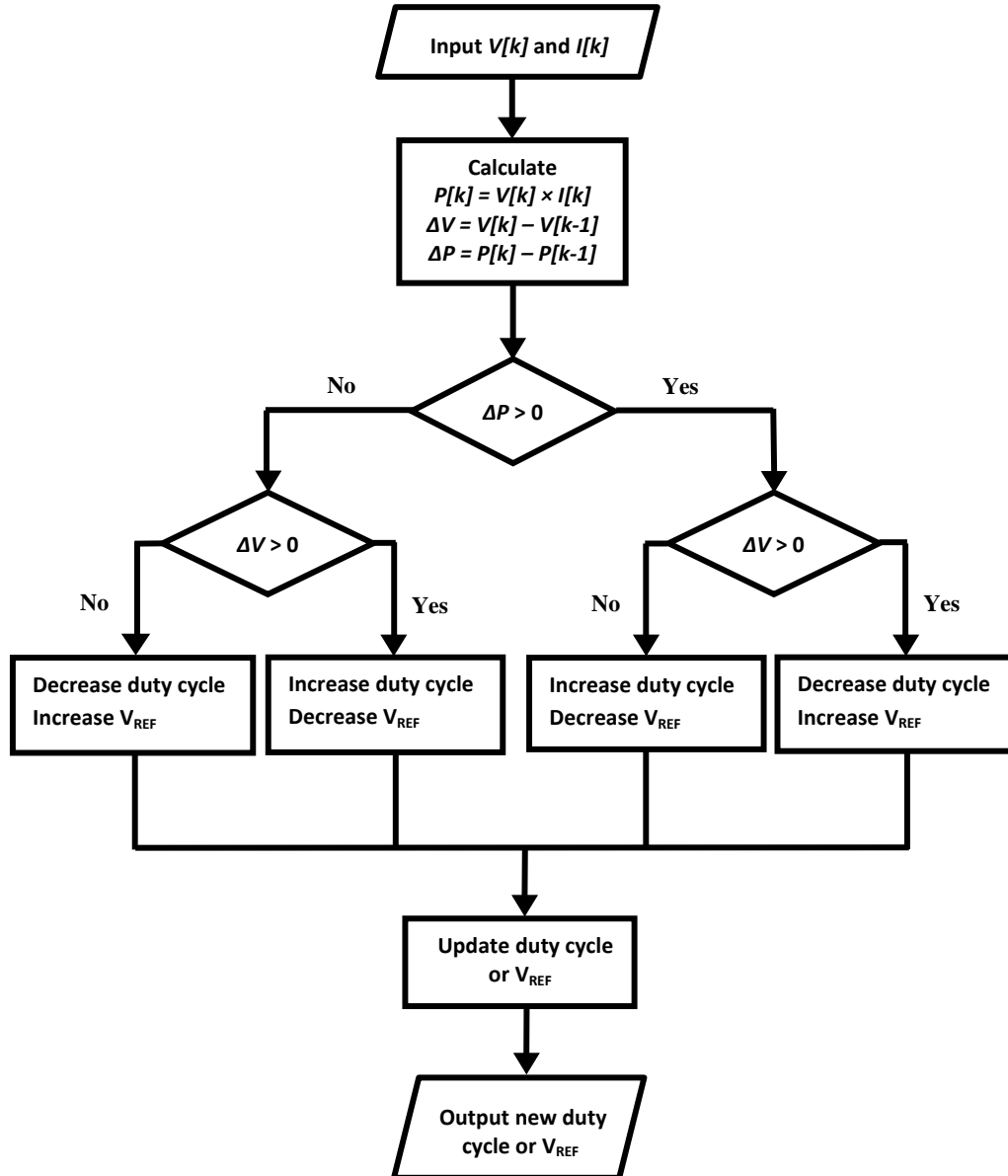
Figure 34.   Perturb and observe flowchart, after [24].

Table 6.   XNOR logic used in the P&O algorithm.

Input		Output	Results	
$\Delta P > 0$	$\Delta V \geq 0$	$\Delta P > 0$ XNOR $\Delta V \geq 0$	Duty Cycle	Reference Voltage
0	0	1	Decrease	Increase
0	1	0	Increase	Decrease
1	0	0	Increase	Decrease
1	1	1	Decrease	Increase

Utilizing the P&O algorithm has several benefits. For one, it is a reliable approach to MPPT, which means that it finds the MPP in almost all circumstances. Also, it is relatively simple and easy to implement [25]. Additionally, it does not require a lot of logic or computational calculations when compared to other methods; however, it does require two sensors – one for the voltage and one for the current [25]. On the other hand, there are a few shortcomings of the P&O MPPT method. For one, this MPPT algorithm always oscillates about the maximum power point and is never truly stable at the MPP [22], [25], [26]. This may result in a reduced amount of power that can be generated by the system [22], [26].

Furthermore, P&O may command the wrong perturbation during rapidly changing solar irradiance conditions. As explained in detail by [25] and [26], the algorithm may decide to command the opposite of what should be done. Consider the situation where the solar irradiance is at 800 W/m^2 and the system is very close to the MPP as depicted at point A in Figure 35. Due to the nature of P&O, the algorithm commands a perturbation even though it is very close to the MPP. Suppose that its command causes the voltage to increase to point B, assuming the solar irradiance stayed the same. Consequently, the algorithm would correctly decide to reduce the voltage since the power decreased when the voltage was increased. Now consider a different scenario. This set of circumstances starts out exactly the same as the first situation. The algorithm decides to perturb the system away from the MPP, which results with an increase in voltage. Assume the solar irradiance rapidly increases to 1000 W/m^2 prior to the next MPPT decision. This causes the algorithm to sense that both the power and the voltage have increased, as is shown by the transition from point A to point C. Consequently, the algorithm commands the system to increase the voltage. As one can see in Figure 35, this is not what should be done to

reach the new MPP. The P&O algorithm quickly recovers from this situation after one MPPT period provided the solar irradiance does not change again. Nevertheless, these circumstances cause the P&O algorithm to take extra time to find the new MPP, and some energy that could have been harvested is lost.
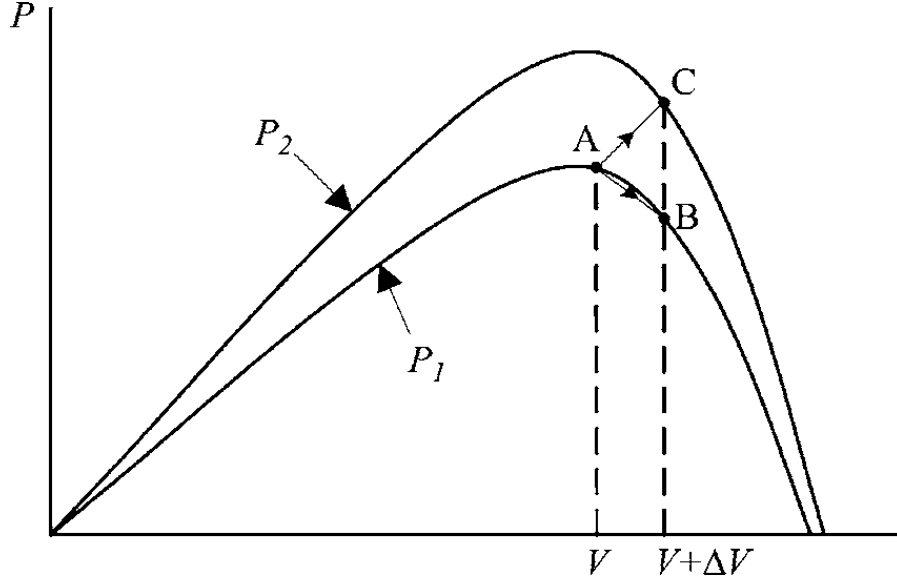
Figure 35.   P&O executing the wrong decision due to a rapidly changing solar irradiance condition, from [25].

2.   Incremental Conductance

The main idea behind the incremental conductance algorithm is that one is trying to drive dP/dV to zero in order to reach the maximum power point. First, one must recognize that the solar panel's power P is just its voltage V times its current I, and its current is a function of its voltage. Furthermore, one must exercise a little calculus to expand this partial derivative. The resulting equation,

$$\frac{dP}{dV} = \frac{dVI(V)}{dV} = I + V\frac{dI}{dV},$$ (39)

is found using the product rule. Next, if dP/dV is set equal to zero, one obtains

$$\frac{I}{V} + \frac{dI}{dV} = 0$$ (40)

48

after a little manipulation. One must calculate the left side of (40) between each MPPT period. To be mathematically correct, one cannot write the derivative term as a pure derivative in the continuous-time sense. One must write it as the change in current over the change in voltage, which occurs between one MPPT period; thus,

$$\frac{I}{V} + \frac{\Delta I}{\Delta V} = 0 \,. \tag{41}$$

The fundamental requirement to be at the maximum power point is concisely specified in (41). Stated another way, the instantaneous conductance (I/V) plus the incremental conductance ($\Delta I/\Delta V$) must equal zero [24], [25]. The $I/V + \Delta I/\Delta V$ calculation determines where the system is on the power versus voltage curve. In other words, one can develop general rules based on this quantity such as

$$\frac{I}{V} + \frac{\Delta I}{\Delta V} > 0 \qquad \textit{left of the MPP} \tag{42}$$

and

$$\frac{I}{V} + \frac{\Delta I}{\Delta V} < 0 \qquad \textit{right of the MPP} \tag{43}$$

as shown in [22], [24]–[26]. In Figure 36, the incremental conductance flowchart is illustrated, and these rules are utilized to execute the algorithm. For instance, if one is left of the MPP, the $I/V + \Delta I/\Delta V$ calculation must be greater than zero, and the duty cycle is decreased while the reference voltage is increased. If the system is operating to the right of the MPP, the $I/V + \Delta I/\Delta V$ calculation must be less than zero, and the duty cycle is increased while the reference voltage is decreased. When the system converges on the MPP, the $I/V + \Delta I/\Delta V$ calculation theoretically equals zero. Consequently, the system's settings remain unchanged, and the perturbations cease.

In practice, the $I/V + \Delta I/\Delta V$ calculation virtually never equal zero due to the limitations of digital computing resolution [27]. In other words, due to noise, measurement error, quantization, and signal processing, the $I/V + \Delta I/\Delta V$ calculation does not equal zero even if the system is perfectly at the MPP. So, one must employ a threshold below which this quantity is considered zero. In this thesis, the threshold for the absolute value of the $I/V + \Delta I/\Delta V$ calculation was 0.012 S. To clarify, when this calculation is within 0.012 of zero, the algorithm considers it to be zero, and the settings

are not changed. Furthermore, the system is so close to the MPP at this point that it is completely reasonable to stop perturbing the system.

Once the $I/V + \Delta I/\Delta V$ calculation is within the threshold, the algorithm commands the system to stop changing the voltage and current for one MPPT period. If after that MPPT period the algorithm determines that the ΔV and ΔI are both zero, then the algorithm keeps the system operating at that point. Practically, ΔV or ΔI is never exactly zero for the reasons mentioned earlier. When determining if ΔV or ΔI is equal to zero, it is necessary to utilize another threshold. This threshold is a small value that is sufficiently close to zero but allows for small deviations due to noise and measurement errors. In this thesis, the thresholds for ΔV and ΔI were set to 0.007 V and 0.006 A, respectively. When ΔV is less than 0.007 V and ΔI is also less than 0.006 A, the algorithm does not change the duty cycle. Unless either the ΔV or the ΔI subsequently changes enough to exceed their thresholds, the system is locked at the MPP.

Additionally, when the ΔV is close to zero, then the $I/V + \Delta I/\Delta V$ calculation may be abnormally large. Typically, this occurs when ΔI is also small but slightly larger in magnitude than ΔV due to noise; however, faulty calculations can take place in other circumstances. For instance, erroneous calculations may take place due to biases in the measurements. The bottom line is that this can cause some problems for the control algorithm; hence, it is necessary to offer a logical alternative in this case. That is why the algorithm first asks if ΔV equals zero. If ΔV is large enough, then the $I/V + \Delta I/\Delta V$ calculation is used to find the MPP. If ΔV is small enough to be considered zero, then the alternate logic path is taken. Then the algorithm checks if ΔI is close enough to zero. If it is, the system does not change its settings. If ΔI exceeds its threshold due to a change in irradiance or random noise, then the system is perturbed according to the $\Delta I > 0$ logic.

Primarily, the alternate logic path exists to account for changing irradiance levels when the ΔV does not exceed its threshold. Referencing Figure 37, one can visualize what happens with respect to the power versus voltage curve in this situation. If the irradiance level goes up while the voltage does not change, the current and the power increase; however, on this new power versus voltage curve, the system is now left of the MPP, and the algorithm is programmed to increase the reference voltage (or decrease

duty cycle). A similar argument can be made for when the irradiance decreases in order to determine what the IC algorithm decides to do. In this case, it decreases the reference voltage (or increases the duty cycle).
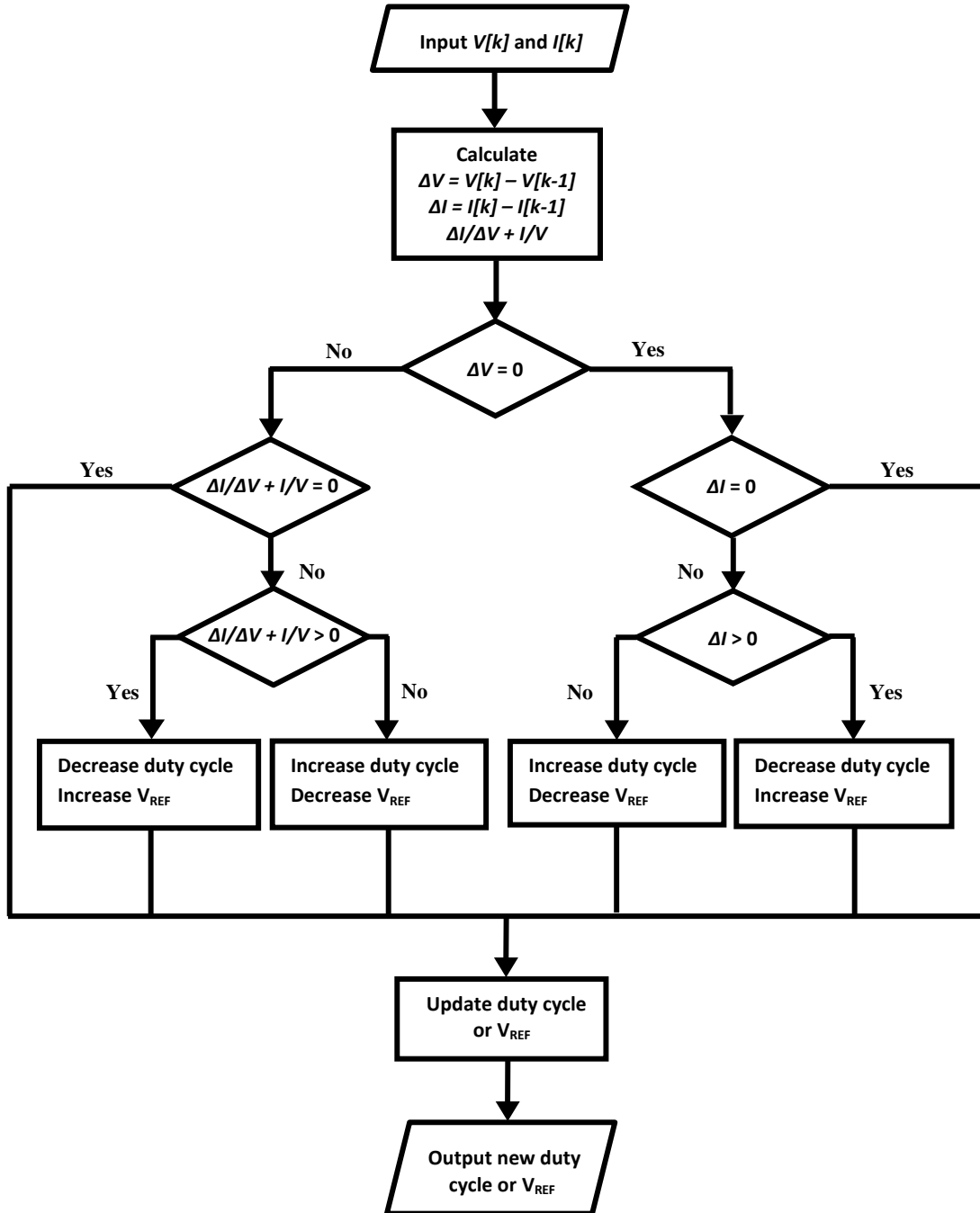
Figure 36.   Incremental conductance flowchart, after [24] and [25].
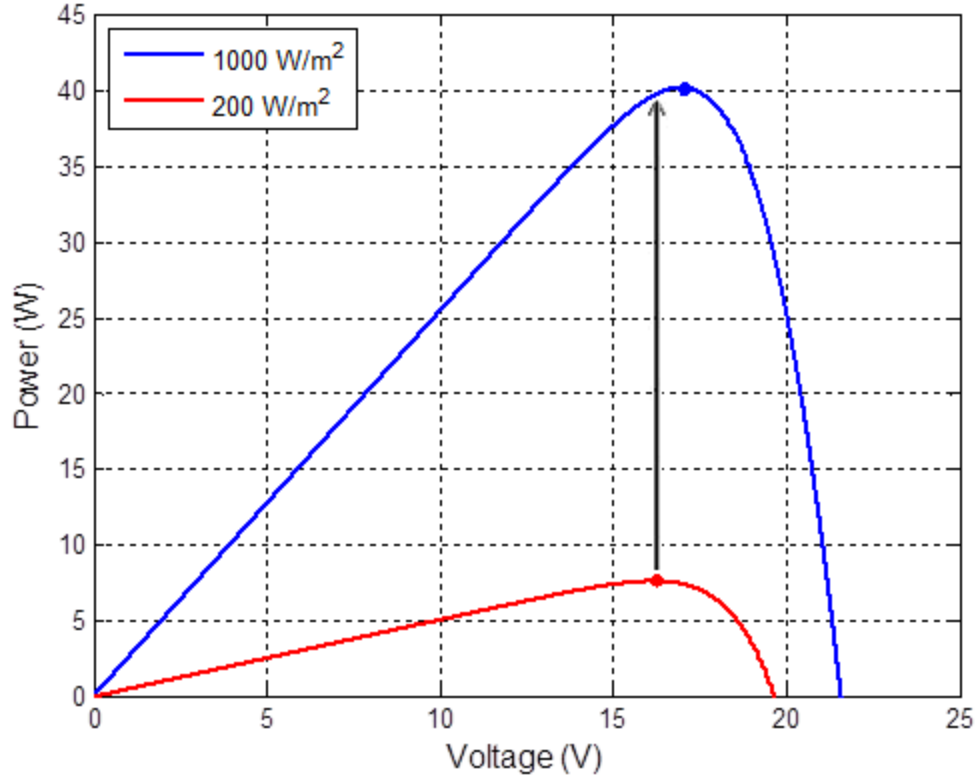
Figure 37.   Power versus voltage curves that show how the system is to the left
of the MPP when the irradiance rises and the voltage remains the
same.

There are certain advantages and disadvantages associated with the incremental conductance algorithm. For instance, IC can lock on to the MPP.   In other words, it finds the maximum power point and then stops perturbing the system unless conditions change. This causes the converter's input as well as its output to be steadier and more constant. While the algorithm is more complicated than P&O, it is still moderately simple to understand. Additionally, just like P&O, this algorithm requires one to measure both the voltage and the current [25]. An obvious drawback to the IC algorithm is the increased requirement for computation and logic when compared to P&O. Also, this algorithm can command the wrong perturbation just as the P&O algorithm but for a slightly different reason. When the solar irradiance increases, the $I/V + \Delta I/\Delta V$ calculation can continually yield a positive answer. This happens if the ΔV and ΔI are repeatedly both positive, and the algorithm causes the reference voltage to increase even if it should not. Yet, just like P&O, the algorithm quickly recovers from a situation such as this once the irradiance is

52

relatively stable. On the other hand, when the solar irradiance decreases, the $I/V + \Delta I/\Delta V$ computation tends to alternate between a positive and negative value, and the algorithm essentially keeps the reference voltage where it was prior to the decrease in irradiance. As a final point, IC can possibly lock onto the wrong setting. If an erroneous $I/V + \Delta I/\Delta V$ calculation causes the algorithm to command no change in the duty cycle, then the algorithm may detect ΔV and ΔI below their thresholds after the next MPPT period. This causes the algorithm to stay at the current operating point indefinitely even if it is not the MPP. Either a change in irradiance or excessive noise in the current or voltage signal may cause the algorithm to exit this adverse mode of operation.

3. Other MPPT Methods

There are many other MPPT methods employed, and they are chronicled in the literature. In [4] and [22], many of these techniques are discussed. In this section of this thesis, some of these methods are explained.

(1) Constant Duty Cycle or Constant Reference Voltage

One of the simplest means of controlling a solar module is to select a constant duty cycle that drives the solar module's voltage close enough to the MPP. Since the duty ratio does not change, there is nothing to alter; thus, it does not require any measurements or feedback [27]. Alternatively, one can select a constant reference voltage. Here, the solar panel's voltage must be measured in order to drive it towards the preselected reference voltage [22], [26]. Both of these methods assume that changing temperature and irradiance conditions are not relevant and can be ignored [22], [26]. Even though these techniques are simple, they do not track the MPP but merely get the panel's output close enough to the MPP so that most of the power available can be harvested. It must be noted that, at low levels of irradiance, these methods may prove to be better than any other [22], [26].

(2) Open-Circuit Voltage or Short-Circuit Current

Another simple, yet sometimes inaccurate, way to control a solar module is to measure either the open-circuit voltage, short-circuit current, or both. The voltage at the

MPP is typically about 70–80% of the open-circuit voltage [25], [27]. Likewise, the current at the MPP is around 78–92% of the short-circuit current [25]. These percentages are based on the type of solar panel and can be measured for various temperatures and irradiance. By knowing the open-circuit voltage or short-circuit current, the algorithm can approximate the MPP. A drawback of these methods is that the system must cease to power the load during the time it is measuring these variables. During this time, the system does not operate at the MPP, and the load does not receive any energy from the solar panel during these measurements.

(3)   Temperature and Irradiance Models

Some systems measure the temperature, irradiance, or both. With this information, the controller can implement mathematical equations to determine the voltage at the MPP. For example, if one knows how the V_{MPP} changes with respect to temperature, then

$$V_{MPP}(T) = V_{MPP,\ ref} + K_{V/T}(T - T_{ref}) \qquad (44)$$

can be used to find the V_{MPP} for the actual temperature T as explained in [27], where $K_{V/T}$ is the change in voltage over the change in temperature. The parameter $V_{MPP,\ ref}$ is the MPP voltage at the reference temperature T_{ref}. If the user wishes to make this method even more robust, they can utilize the solar irradiance measurement as well. Now, one can develop a set of equations to describe how both temperature and irradiance relate to V_{MPP}. As an alternative, one can measure the V_{MPP} for many different solar irradiance levels and temperature settings. At that point, one can enter these values into a look-up table. The control algorithm can then simply look up the desired voltage for maximum power based on the measurements of solar irradiance and temperature. If they do not match up exactly, then interpolation can be used to approximate the desired voltage.

(4)   Fuzzy Logic

Fuzzy logic can be used to formulate a matrix of possible outcomes based on certain input parameters. As explained in [25], one can create an error signal E that is the change in power divided by the change in voltage between MPPT periods, and one can

calculate the change in this error signal ΔE. As presented in [25], an example of these calculations is

$$E[k] = \frac{P[k] - P[k-1]}{V[k] - V[k-1]}$$ (45)

and

$$\Delta E = E[k] - E[k-1].$$ (46)

With these calculations, one can proceed to the next step, which is to categorize these inputs using a fuzzy logic table as depicted in Figure 38.

E \ ΔE	NB	NS	ZE	PS	PB
NB	ZE	ZE	NB	NB	NB
NS	ZE	ZE	NS	NS	NS
ZE	NS	ZE	ZE	ZE	PS
PS	PS	PS	PS	ZE	ZE
PB	PB	PB	PB	ZE	ZE

Figure 38.   An example of a fuzzy logic table, from [25].

In Figure 38, NB is negative big, NS is negative small, ZE is zero, PS is positive small, and PB is positive big [25]. The programmer has to decide the numerical thresholds for defining what constitutes NB vs. NS and so on. Once the algorithm determines how to categorize the inputs E and ΔE from the look-up table, a change to the control parameters may be applied. For instance, PB may mean that a 2% change in duty cycle ΔD is warranted, while PS may mean that only a 1% increment is necessary. If the fuzzy logic table determines that the inputs fall into the ZE category, then the increment in duty cycle (or reference voltage) is zero.

(5)   Current Sweep

The current sweep method involves systematically varying the current from the solar panel at certain intervals [25]. By doing this, the controller can take several voltage

and current measurements in order to determine the voltage that produces the MPP [25]. Once this is known, the controller attempts to drive the solar panel's voltage to the MPP voltage. The disadvantage of this method is that the system must take time to run the current sweep. Just like the open-circuit voltage and short-circuit current methods, the system does not operate at the maximum power point at all times.

(6)   Ripple Correlation Control

Ripple Correlation Control is similar to other MPPT methods except one measures the AC ripple in the panel's voltage and current. Using this information, one can correlate the time rate of change of the power $\dot{p}$ with either the time rate of change of the voltage $\dot{v}$ or the current $\dot{i}$ [25]. As outlined in [25],

$$d(t) = -K_{RCC} \int \dot{p}\dot{v} \; dt \tag{47}$$

describes a control law that uses the voltage and power ripple to determine the duty cycle $d(t)$, where K_{RCC} is a proportionality constant. From (47), one notices that when $\dot{p}$ and $\dot{v}$ are either both positive or both negative, the duty cycle decreases. The result is that when the panel operates to the left of the MPP, the duty cycle decreases in order to increase the panel's voltage. Conversely, when $\dot{p}$ is positive and $\dot{v}$ is negative (or vice versa), the duty cycle increases. In this case, the panel operates to the right of the MPP, and the duty cycle increases in order to decrease the panel's voltage.

(7)   *dP/dV* or *dP/dI*

A more intuitive way of controlling the panel is to calculate a partial derivative, either *dP/dV* or *dP/dI*. It is important to note that these derivatives are simply the slope of the power versus voltage curve or the power versus current curve, respectively. One can see from those plots that the MPP occurs when the slope equals zero. By using this method, one can drive the partial derivative to zero and reach the MPPT [25].

(8)   Maximize Output Current or Voltage

Still another method of MPPT is to maximize either the output current or output voltage. By doing this, the converter also maximizes the input power from the solar panel. As explained in [28], the load can be voltage-source type, current-source type,

resistive-type, or a combination. In this thesis, the output is voltage-source type due to the inclusion of a battery in the circuit; thus, one can attempt to maximize the output current and arrive at the MPP. An advantage of this type of control methodology is that only one sensor is required [25].

(9)   IC or *dP/dV* by Proportional-Integral Control

There is yet another method for conducting MPPT that involves using a proportional-integral (PI) controller [25], [27]. Here, the *I/V + ΔI/ΔV* is calculated just as in the IC method. This calculation is subtracted from a reference value of zero, and this error signal is then fed into a PI controller to drive the error to zero [25]. This same method can be used for the *dP/dV* calculation. Note that the output from the PI controller is the duty cycle value as depicted in [27].

D.   METHODS OF CONTROLLING DUTY CYCLE

How the controller calculates where the system is with respect to the MPP and how, at that moment, it decides to adjust the duty cycle (increase, decrease, or neither) in order to track the MPP was explained in the previous section. The various ways the duty cycle can be realized once the MPPT algorithm makes a decision is described in this section.

1.   Direct Duty Cycle Control

The most straightforward way to adjust the duty cycle in response to the command given from the MPPT algorithm is control it directly. Using this method of control involves simply incrementing or decrementing the duty cycle in order to find the MPP; however, there is an opposite correlation between the input voltage, which is solar panel's voltage, and the duty cycle. For instance, the input voltage decreases while the duty cycle increases and vice versa. To understand why this is so, one must first recall the input and output relationship for the voltages of a boost converter from (17), which can be transformed to yield

$$D = 1 - \frac{v_{IN}}{v_{OUT}}. \tag{48}$$

57

If the output voltage v_{OUT} is constant, then increasing the converter's input voltage v_{IN} decreases the duty cycle D according to (48). Also, decreasing the input voltage increases the duty cycle; thus, the direct duty cycle control method must take this into account when updating the commanded duty cycle. To summarize, this method controls the panel's voltage by changing the duty cycle, and consequently, the MPP can be found.

In Figure 39, a hypothetical power versus duty cycle curve is displayed for this system when the irradiance is 1000 W/m^2 and the temperature is 25 °C. One notices that the slope in the vicinity of the MPP is somewhat flat. In other words, the duty cycle can vary a considerable amount before there is a significant change in power. As a case in point, if the duty cycle was to stay within ± 0.05, the power only varies by about ± 3 W. Typically, for P&O, the duty cycle only varies by about ± 0.01–0.02 once the MPP is found. In the vicinity of the MPP, the power does not drop off significantly as the duty cycle varies. This fact is an important point and is why direct duty cycle control works.
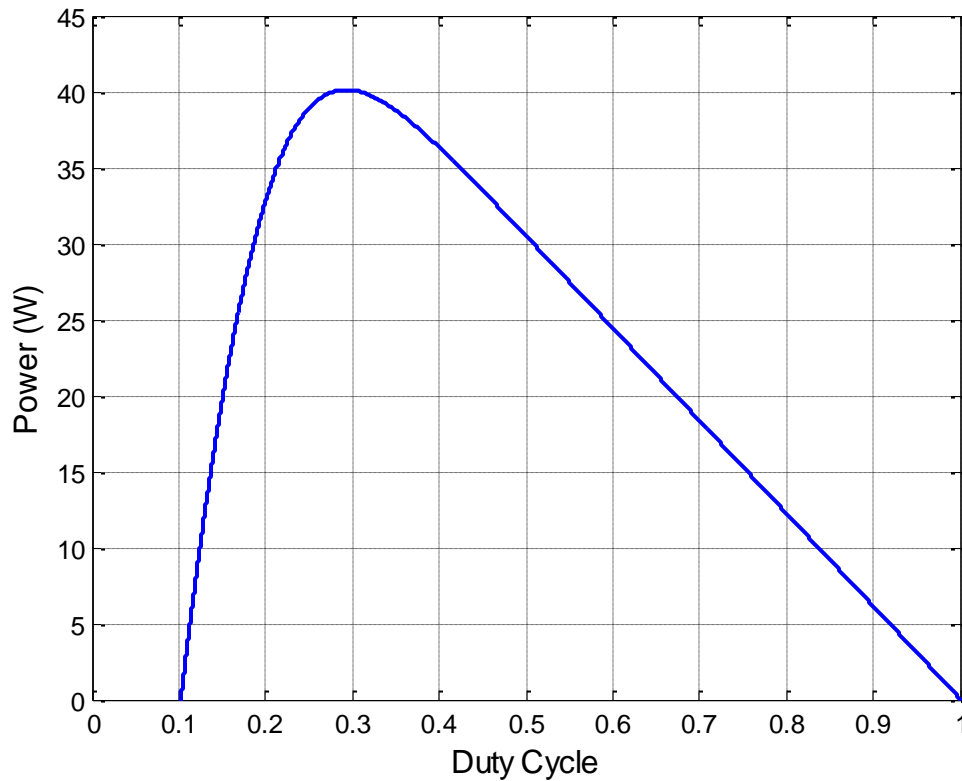
Figure 39.   Power versus duty cycle for 1000 W/m^2 and 25 °C.

2. Voltage Reference Control

In the previous section, the inverse relationship between the input voltage and the duty cycle was explained. Since the reference voltage is used to alter the input voltage, it follows that the reference voltage also has this contrary relationship with the converter's duty cycle. For instance, when referring to the commanded perturbation, the duty cycle increases while the reference voltage decreases and vice versa. A block diagram of this method is shown in Figure 40 in order to better illustrate the concept of voltage reference control.
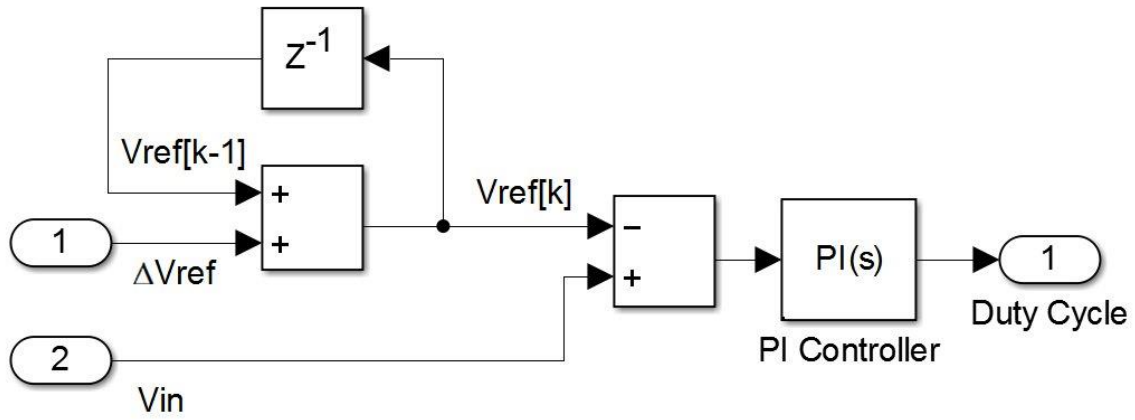
Figure 40.   Block diagram of voltage reference control.

To execute this type of control, one increases or decreases the reference voltage in order to find the MPP. The change in the reference voltage ΔV_{REF} is fed in from the MPPT algorithm and is then added to the previous voltage reference to find the new voltage reference. As one can see from the block diagram, the voltage reference is subtracted from the actual input voltage. From there, this difference is compensated for using a PI controller to produce a value for the duty cycle. It is assumed that between MPPT periods the input voltage v_{IN} gets sufficiently close to the reference voltage V_{REF}. Otherwise, this method may take longer than desired to converge on the MPP. Additionally, the reference is subtracted from the actual value so that the duty cycle is driven in the correct direction. For instance, consider the situation where V_{REF} increases since the system operates to the left of the MPP. The difference between v_{IN} and V_{REF} should now be negative. This decreases the duty cycle, which increases the input voltage as desired. On the other hand,

59

if the system operates to the right of the MPP, the MPPT algorithm commands V_{REF} to decreases, which creates a positive difference between v_{IN} and V_{REF}. This causes the duty cycle to rise, and the input voltage goes down.

3. Current Reference Control

Another method that can be used to control the duty cycle is current reference control. In Figure 41, a block diagram for current reference control is displayed so that one may understand the subtle differences between voltage reference control and current reference control. One can see that this method is very similar to voltage reference control, but the control variable is now current vice voltage. Also, the convention for finding the difference between the input and the reference is not reversed. In other words, one subtracts the input current from the reference current to find the difference, which is fed into the PI controller. The reason for this can be explained rather easily. Normally, the input current changes in the direction opposite to the input voltage unless there is a significant change in irradiance; thus, increasing the current requires that the duty cycle also increases. Conversely, if the current goes down, then the duty cycle should go down as well.
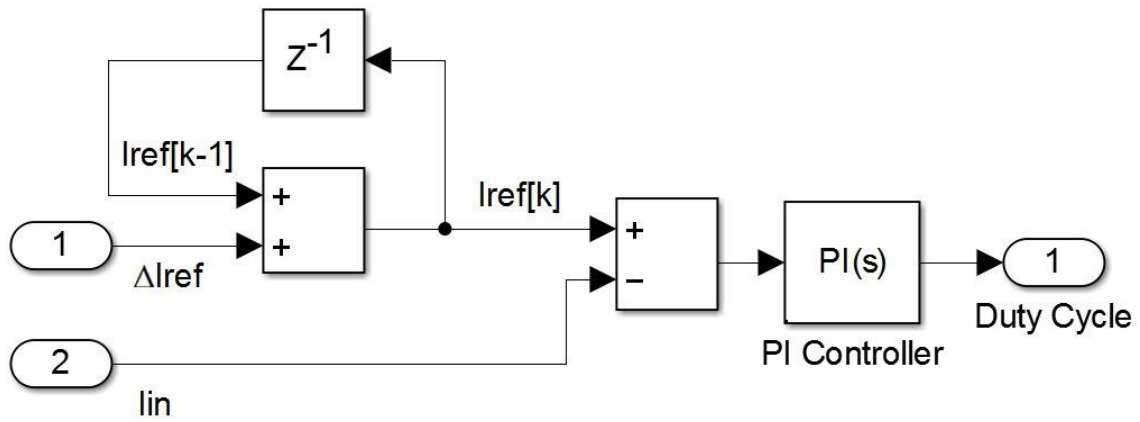
Figure 41. Block diagram of current reference control.

As alluded to earlier in this thesis, current reference control is not commonly used. This method has a significant drawback according to [4]. In Figure 42, one will

notice the sharp drop in power on the right side of the power versus current curve. This means that altering the input current by even a little may cause the power to change drastically, and the system's performance suffers [4]. Furthermore, during rapidly changing irradiance conditions, the solar panel's current changes significantly [4]. This makes it difficult for the reference current to catch-up with the actual input current. Consequently, the system may be commanded to move away from the new MPP when it should not do so.
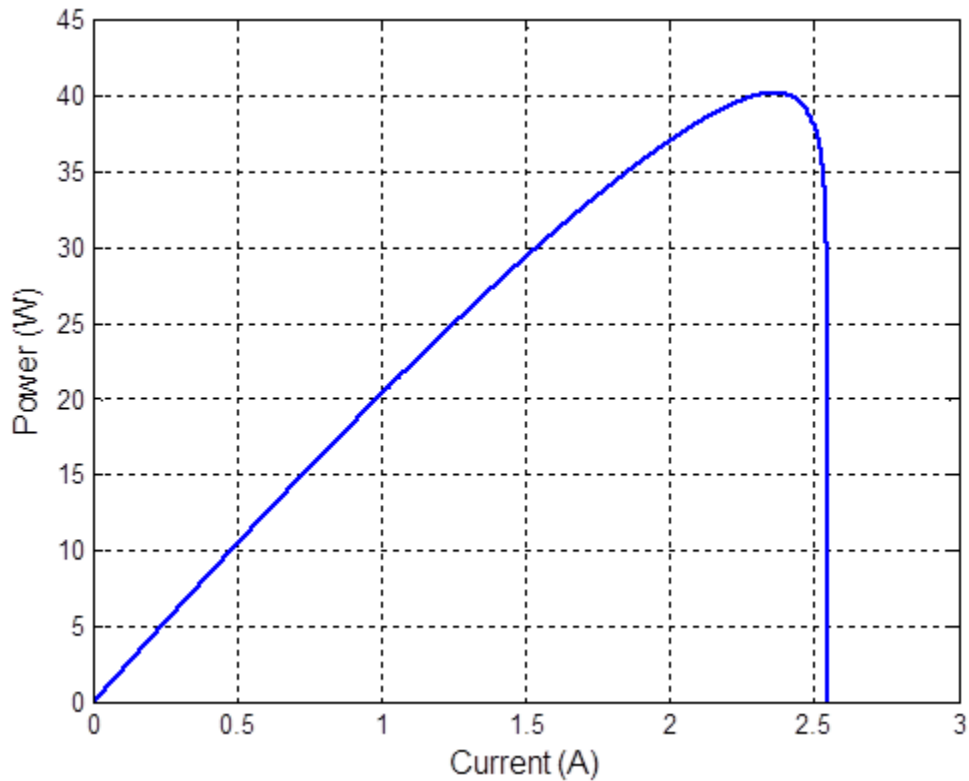
Figure 42.   Power versus current at 1000 W/m^2 and 25 °C, after [4].

4.   Fixed Step versus Variable Step

For each type of the control methods discussed above, one must determine the step-size of the control variable. In direct duty cycle control, one changes the duty cycle between each successive MPPT period, and one must choose by how much the duty cycle changes when given a command to increase or decrease. Also, voltage reference changes a voltage level while current reference modifies a current setting. When using these

control methods, one must decide by how much to alter the reference setting. One can use a fixed step-size where the change in duty cycle (or reference level) is constant regardless of the operating point. For example, one may elect to change the duty cycle by 0.005 every time the algorithm determines a change needs to be made. On the other hand, one may elect to use a variable step-size. Here, the step-size is varied based on how far away the operating point is from the MPP. The control parameter's step-size, in part, determines the speed of the algorithm. A larger step-size causes the algorithm to converge on the MPP more quickly than a smaller one, but too large of a step-size may cause the algorithm to fluctuate around the MPP too much. A variable step-size uses a larger step when further from the MPP and a smaller step when close to the MPP. The other component that determines the algorithm's speed is the frequency of the MPPT update rate f_{MPPT}, which is the inverse of the MPPT period. When these two parameters are multiplied together, the time rate of change of the control parameter is the result. As stated in [27, pg. 1158], "This rate is a parameter that should be adjusted to allow the balance between faster response and less fluctuation in steady state."

5.   Discrete Step versus Integration

Up to this point, it has been assumed that the change in the control parameter is handled as a discrete step. In other words, when the MPPT commands a perturbation, the duty cycle instantaneously changes to the new value without taking on any intermediate value. This can be called a discrete step-size, but there is another way to implement the transition to the new value. This procedure involves using an integrator which ramps the duty cycle up (or down) to the new value over one MPPT period. In this way, the shift to the new duty cycle is more gradual and smoother than a discrete jump.

E.   TYPES OF SYSTEMS USED FOR SOLAR PHOTOVOLTAIC POWER CONVERSION

The differences between centralized, string, and micro-converter systems are explained in this portion of this thesis. The advantages and disadvantages of each type of system are highlighted. In addition, a theoretical example is given to show how a system

with micro-converters may be able to extract the maximum amount of power from two solar panels when one of them is shaded.

1.   Centralized System

A centralized system consists of several solar panels that are assembled in series and in parallel to create a solar array [4], [29]. This entire array is fed into a power converter in order to execute the MPPT. An example of a centralized system is seen in Figure 43. The dashed lines are intended to indicate that the size of the array can be variable. In other words, one can connect several solar modules in a variety of different series and parallel combinations.
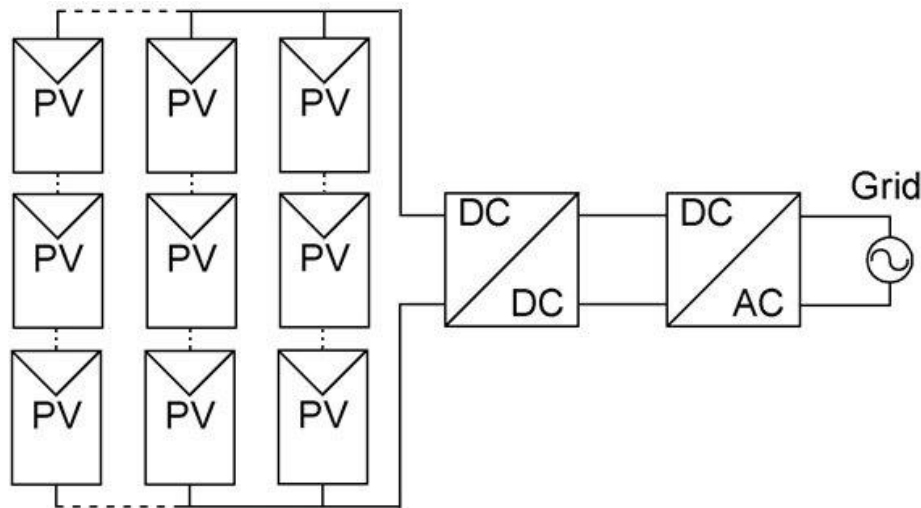
Figure 43.   Schematic diagram of a centralized system, after [29].

The system displayed in Figure 43 can be referred to as a two-stage topology since it employs two separate power converters [29]. The DC-DC converter conducts the MPPT, while the DC-AC inverter allows for the rest of the system to interface with the AC grid. It is important to realize that for all of these systems a single-stage topology, which contains only one DC-AC inverter, can be used as well [29].

There are several pros and cons of a centralized system. For instance, since this system does the MPPT for the entire array, it cannot account for individual panels that are operating differently; thus, while individual panels may not be operating at their MPP,

the array is driven to its MPP [30]. The disadvantage of this construct is that some of the available power is not extracted from the array because each individual panel is not at its MPP. An advantage of this type of system is that the components used to realize such a system are minimized [4]. As one may realize from Figure 43, this type of system uses only a DC-DC converter and a DC-AC inverter for the entire array. Later, it is demonstrated that other topologies typically use more power electronic components. Another benefit of using a centralized system is that the control methodology is relatively simple when compared to other systems since it only has to control one or two converters vice multiple converters.

2. String System

In Figure 44, the schematic diagram of a string system is shown. Here, the solar panels are assembled in series to create a string [4], [29]. From there, the string is connected to a converter that conducts the MPPT for the entire string of solar panels [4], [29]. Additionally, multiple strings can be assembled in parallel to generate even more power.
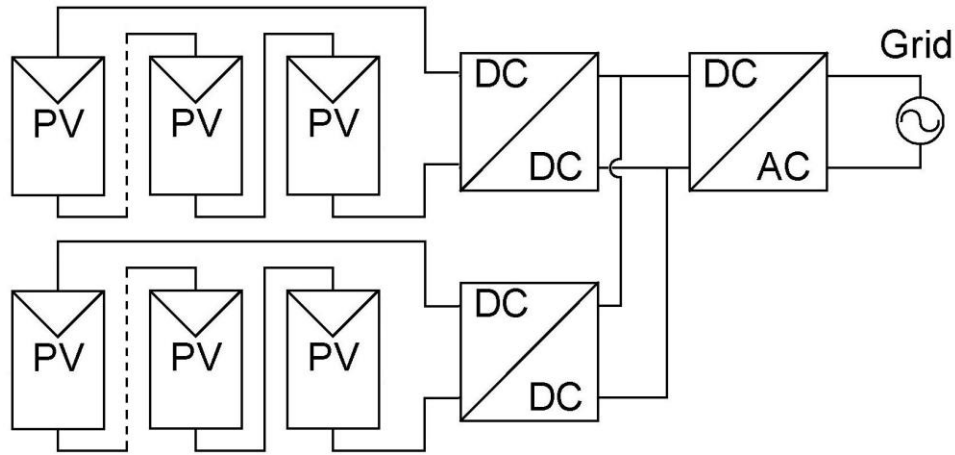
Figure 44.   Schematic diagram of a string system, after [29].

There are a few pros and cons associated with this type of system. For one, since the panels are placed in series, the maximum amount of current following in a string is dependent on the solar panel that harvests the least amount of irradiance. This concept is

64

developed later in this section, but the main point is that a string system, like the centralized system, may not produce all of the available power; however, it performs better than a centralized system [4]. Since a dedicated converter does the MPPT for each string, the efficiency of power generation is improved when compared to the centralized system [4], [29]. Another positive aspect of this type of system is that it allows for more flexibility and modularity [4]. For instance, each string is its own section, which can be modified or even shutdown without affecting other strings. A disadvantage is that the number of power electronic components is larger than the number of components for a centralized system. Additionally, the system has to monitor and control more converters.

3.   Micro-converter System

Finally, the micro-converter system, which employs a MPPT converter for each individual solar panel, is displayed in Figure 45. There are two different schematic diagrams contained in Figure 45. The one on the left shows a micro-converter system, where each panel with its own micro-converter is placed in parallel. On the right, each panel and micro-converter combination is connected in series. Here, only two panels are shown per diagram. One must realize that it is possible to connect several of these in series and in parallel to form an entire array made up of many solar panels each with its own micro-converter.
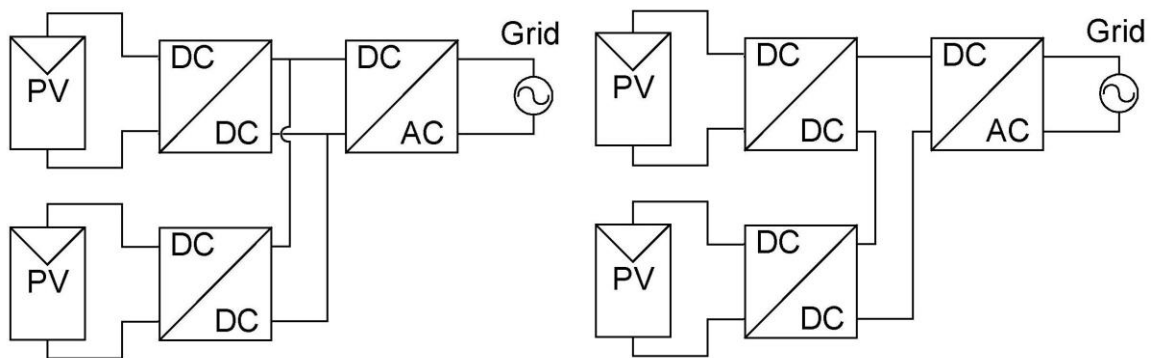
Figure 45.   Schematic diagrams of a micro-converter system in parallel and a
micro-converter system in series, after [29].

The advantage of this type of system is that it has the ability to obtain the maximum power from each solar panel. In addition, if one of the panels is degraded, then the rest of the system does not suffer [30]. A panel can operate in a degraded state for a variety of reasons. For instance, it may be old and deteriorated. Also, the module may be shaded due to debris, snow, trees, or other objects [30]. This type of system epitomizes flexibility and modularity. For instance, the layout of the system is easily expanded or reduced without affecting other parts of the system [30]. The micro-converter has some negative aspects as well. For one, this system, like the string system but more so, employs several power electronic components. It is important to note that since each converter interfaces with only one panel, the size of these components can be scaled down. Furthermore, each panel has a converter that must be controlled, which increases the complexity.

4.   Theoretical Analysis of These Types of Systems

Consider the situation where two solar panels are connected in series. One of the panels is not shaded and receives 1000 W/m^2 from the sun. The other panel is uniformly shaded such that it effectively experiences just 200 W/m^2 of solar irradiance. For this scenario, the plots of the current versus voltage and the power versus voltage look like the curves in Figures 46 and 47, respectively. As one can see, the maximum attainable current is the short-circuit current of the shaded panel. Since the panels are connected in series, a current mismatch affects the performance of the unshaded panel. In this case, the resulting power of approximately 16.2 W is significantly lower than the power attainable from one unshaded panel operating alone. This demonstrates a potential drawback associated with the centralized and string systems.
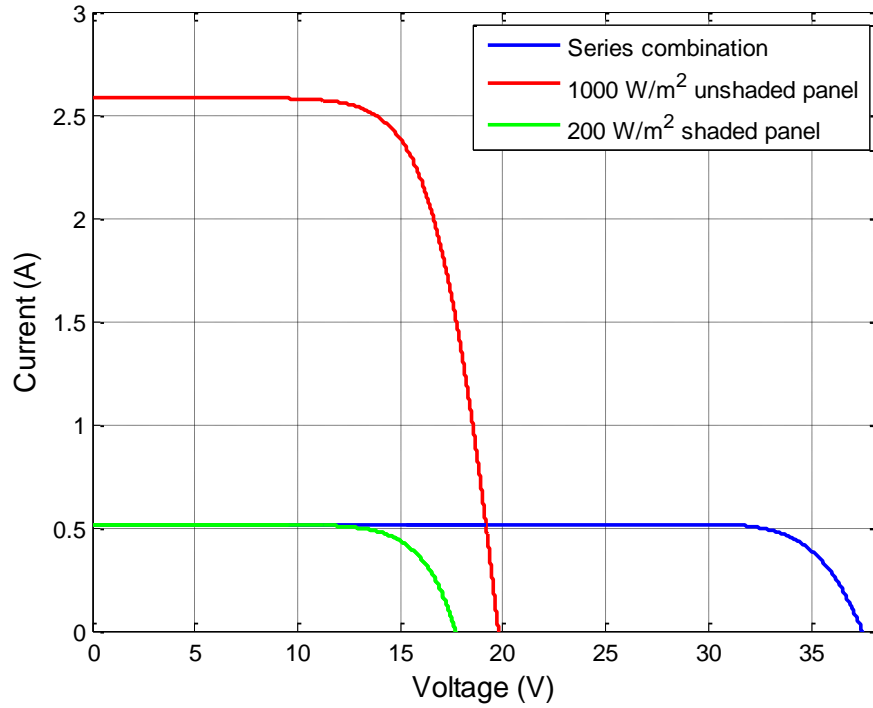
Figure 46.   Current versus voltage for an unshaded and a shaded solar panel connected in series.
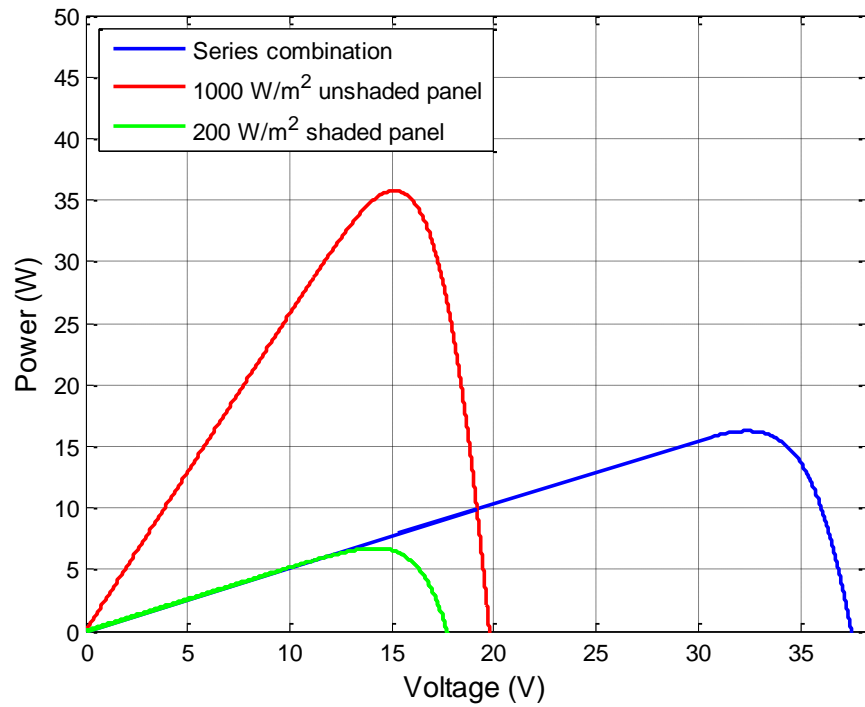
Figure 47.   Power versus voltage for an unshaded and a shaded solar panel connected in series.

Next, consider the scenario where these two panels are assembled in parallel. Here, the current versus voltage and power versus voltage resemble Figures 48 and 49, respectively. One can see that the resultant power is very good. For instance, the power attained in this parallel combination is about 42.3 W. In this situation, the maximum available power is 42.5 W if one gets the maximum power out of each panel. Since the panels are in parallel, they do not operate perfectly at their respective MPPs [4]. Instead, there is a mismatch between their corresponding MPP voltages, and the actual voltage experienced by this parallel combination ends up somewhere in between. In this case, the mismatched panels are not far from their individual MPP voltages. If all of the modules are placed in parallel, it may be possible to set up a system that produces most of the available power; thus, it may be acceptable to operate this type of parallel setup and not have to place a MPPT converter on each panel.
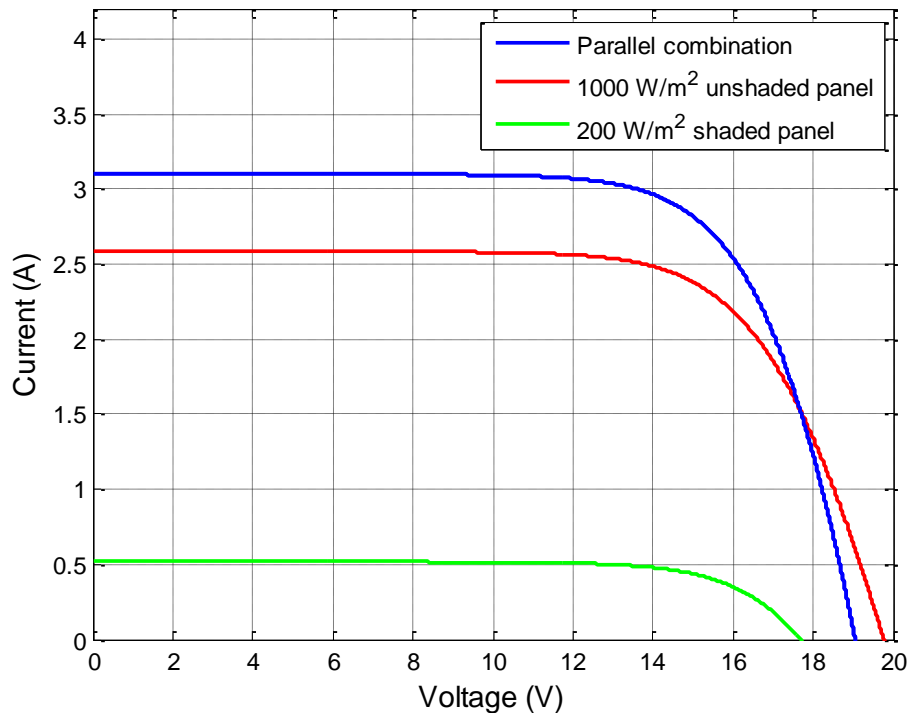
Figure 48.   Current versus voltage for an unshaded and a shaded solar panel connected in parallel.
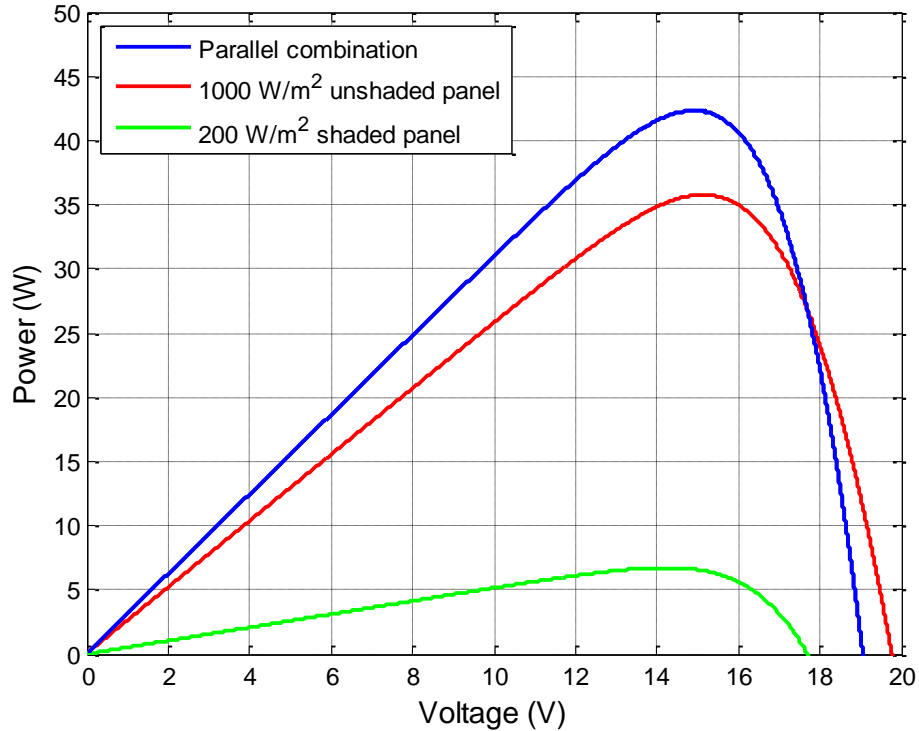
Figure 49.   Power versus voltage for an unshaded and a shaded solar panel
connected in parallel.

In most applications, the voltage across the solar array is desired to be larger than
just one panel can offer. Thus, it is necessary to stack modules in series in order to
achieve a higher voltage. To avoid the effects of series-connected solar cells that are
shaded, one may elect to use bypass diodes. Bypass diodes are placed in parallel with a
group of solar cells within a panel or a whole panel as seen in Figure 50. They allow
current to flow around underperforming cells. In other words, when a group of solar cells
operate in a degraded state, the bypass diode becomes forward biased at some point and
offers a path for the current that has less resistance [31], [32]. In this simplified example,
the shaded panel is bypassed entirely through the use of a bypass diode. In Figures 51 and
52, the current versus voltage and power versus voltage is shown for two series-
connected panels, where the shaded panel utilizes a bypass diode. In this scenario, the
shaded panel is completely bypassed for currents above about 0.5 A. Below that, the
bypass diode does not conduct, and current is allowed to flow through the shaded panel.
One can see that 34.1 W is attainable assuming the MPPT converter forces the system to

operate at the true MPP. While this does not harvest the maximum power of 42.5 W, it is a significant improvement compared to the two series-connected panels that did not use bypass diodes. Moreover, using an individual MPPT converter on each panel allows the system to get the additional 20% of available energy.
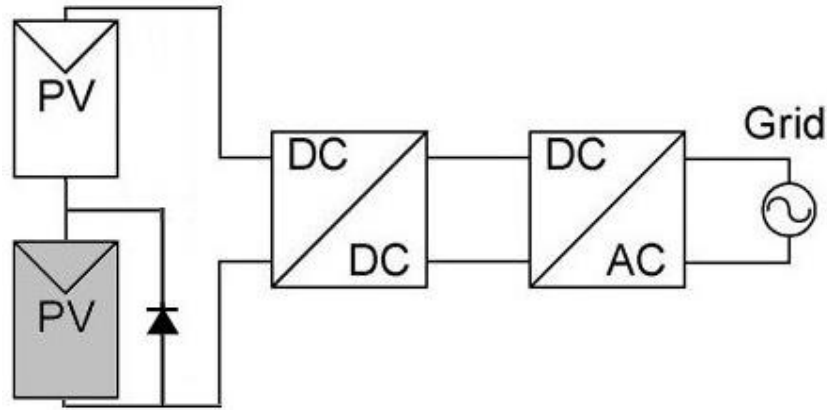
Figure 50.   Schematic diagram for two series-connected panels where the shaded panel is utilizing a bypass diode.
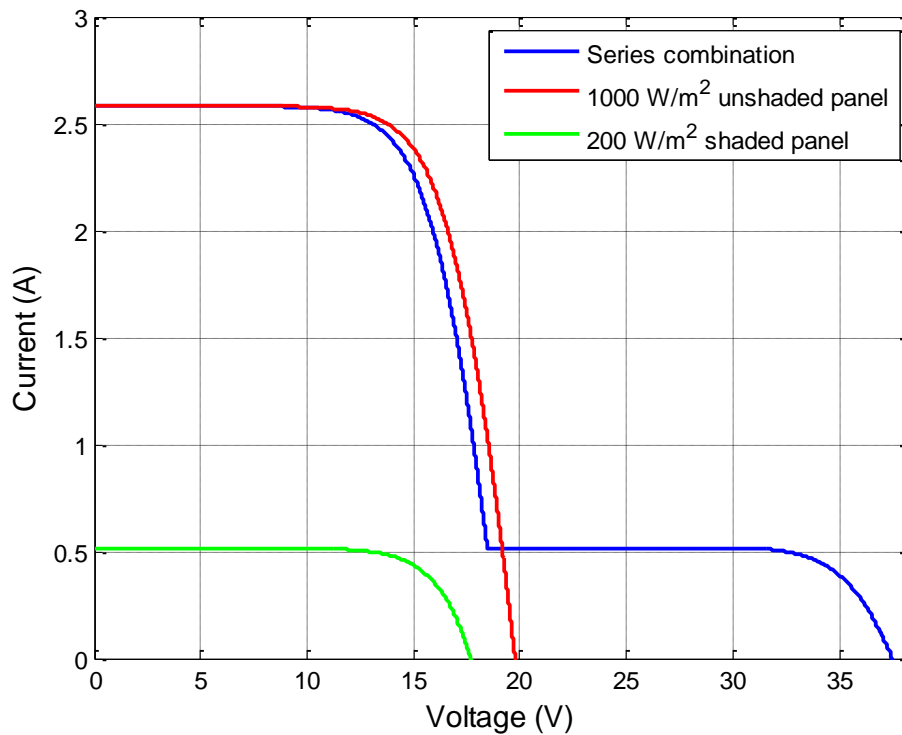
Figure 51.   Current versus voltage for an unshaded and a shaded solar panel connected in series where the shaded panel uses a bypass diode.

Another deficiency is that the two panels are now required to operate around 14.5 V to be at their MPP. If these solar panels are in a string system, then this may not be a problem. If these panels are part of a centralized system, then the repercussions can be significant. Consider two other series-connected panels that are operating at 1000 W/m^2. The MPP voltage across these two panels is 30.3 V. If these two panels are connected in parallel with the other two panels, a voltage mismatch exists. As explained previously, the voltage mismatch causes the system to operate somewhere between 14.5 V and 30.3 V.
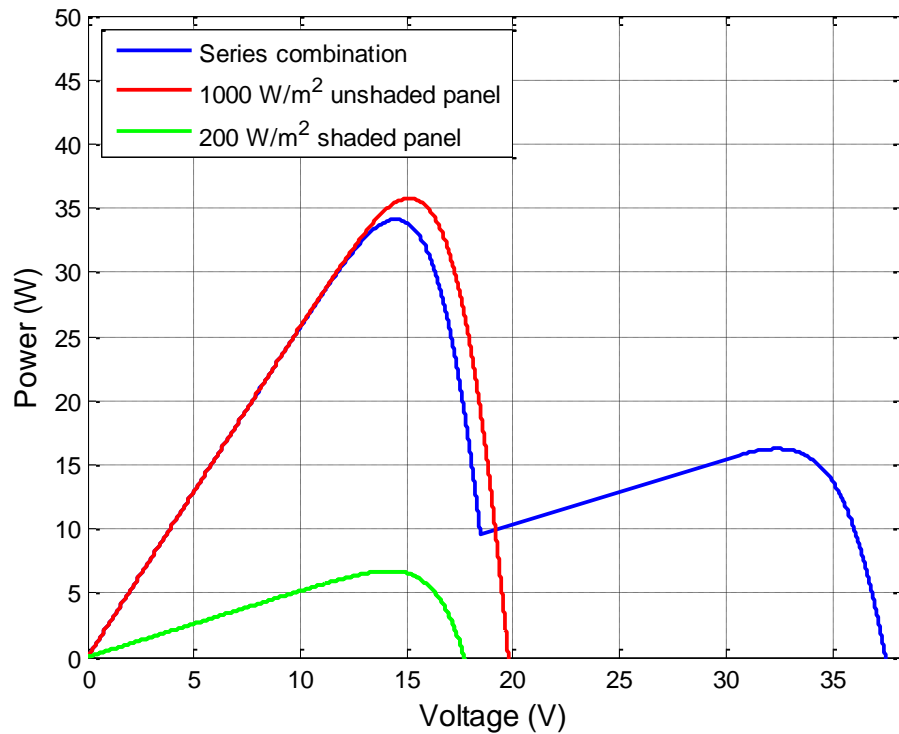
Figure 52.   Power versus voltage for an unshaded and a shaded solar panel connected in series where the shaded panel uses a bypass diode.

If the voltage mismatch between parallel-connected elements is too large, the use of blocking diodes may be necessary. A blocking diode is placed in series with a string of solar cells and prevents current from flowing in the opposite direction back into the panel [31], [32]. If the voltage mismatch is large enough due to either damage or severe shade, some of the current from the unshaded panels can flow back into the degraded panels

[31]. This is undesirable since the energy flowing back into the degraded panels, which are consuming power in this scenario, is wasted [31], [32]. While the blocking diode prevents certain unwanted conditions from occurring, it draws additional power from the system during normal operation. Employing a boost converter on each panel or with a string system eliminates the need for blocking diodes.

Finally, certain MPPT algorithms can possibly lock onto the wrong point if there are multiple local maxima. Typically, there is only one maximum power point; however, in the presence of mismatched conditions due to shading and bypass diodes, it is possible to have more than one local maximum as depicted in Figure 52 [4], [25]. In this situation, the algorithm can possibly oscillate around a local maximum that is not the MPP. Of note, the centralized and string systems are susceptible to this situation. One possible solution is to use an algorithm that can find the MPP. With that said, the algorithms used in this thesis are relatively simple and are not suitable for this task. An alternative solution is to operate a MPPT converter on each panel as is demonstrated in this thesis.

III. IMPLEMENTATION

How the digital MPPT algorithms were implemented using a field-programmable gate array are explained in this chapter. Furthermore, some of the key topics as well as the required actions that were necessary to implement these designs are discussed.

A. XILINX FPGA

The Xilinx Virtex-4 XC4VLX25-10SF363 FPGA was used in this thesis to handle all of the digital signal processing, computation, and logic. In addition, the FPGA was programmed so that Chipscope Pro could be utilized. Chipscope Pro is a Xilinx computer program that allows the user to control the system and interface with it so that one can sample real-time data and export it for analysis. Furthermore, the FPGA was used to generate the logic signals that went to driver circuits that operated the IGBTs. A picture of the Xilinx board used in this thesis is shown in Figure 53.
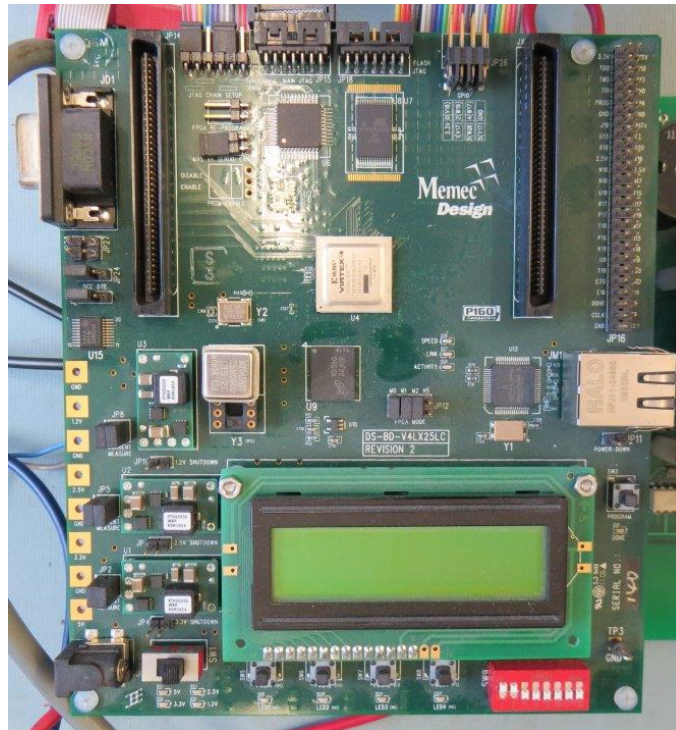
Figure 53.   Xilinx board used in this thesis research.

In order to generate the VHDL code that was loaded into the FPGA, the Xilinx blockset in Simulink was utilized. A few of the logic designs and algorithms using the Xilinx blockset in Simulink are contained Appendix B. Once the Xilinx-based design was complete, the system generator block was utilized to create a Xilinx ISE project file. This file was then passed to the Xilinx Project Navigator in order to synthesize the VHDL code used in the FPGA. Finally, Chipscope Pro loaded the VHDL file into the FPGA and was used to control the system and record data.

B. FIXED-POINT BINARY NUMBERS

Using the Xilinx blockset with this particular FPGA required the use of fixed-point binary numbers. Binary numbers are chronicled in countless textbooks and papers. As such, it is not the intent to recount every minuscule detail on the subject. Nevertheless, a brief explanation of fixed-point binary numbers is essential in order to explain some of the design considerations that are necessary.

This particular FPGA does not allow for the use of floating point numbers, where the binary point can be moved in a way similar to how a decimal point is shifted when using scientific notation. Since the FPGA does not allow this format, fixed-point numbers were employed. This is where the binary point remains fixed. For each signal, it was necessary to specify the number of integer bits and the number of fractional bits. In Figure 54, an example of these options is shown from the output tab on an adder/subtracter module. Here, one can see that the total number of bits is 23, and the binary point is placed to the left of the 17th bit; therefore, there are 17 fractional bits in the output of this module. The other six bits are used to express the integer part as well as the sign bit. Moreover, it was necessary to specify whether the number was a signed two's complement number or an unsigned number. Unsigned numbers mean that the number can only be expressed as a positive value. Signed two's complement allowed the number to be positive or negative. Mostly, signed two's complement was used in the algorithm, but counters, which were used to make the MPPT clock signal for example, employed unsigned numbers.

Figure 54.   Xilinx output tab showing the fixed-point options.

One of the most important considerations was to ensure that there were enough bits in the integer part of the number so that the value could be correctly represented. Otherwise, the value would be at the saturation limit, and inaccurate calculations would result. For example, if a certain variable such as the input voltage did not go above about 22 V, then one only needs six bits (including the sign bit) in the integer part to represent that number. If only five bits were used, the saturation limit would be 16 V. Thus, any time the value for the voltage went over 16 V, the algorithm would use a value of 16 V. Obviously, one can see how this can cause a problem. Also, it was vital to achieve enough precision when specifying the fractional part of a number. Based on the information contained in [33], one can develop and utilize the relationship

$$2^b \geq 10^d \tag{49}$$

to determine how many fractional bits are necessary, where b is the number of fractional bits and d is the number of decimal places. Basically, the number of fractional values that the binary representation can express must be equal to or greater than the amount of fractional values that the decimal representation can express. Equation (49) can be manipulated to obtain

$$d \leq b \, \log_{10}(2), \tag{50}$$

75

which is similar to what is described in [33]. Looking back at the example presented by Figure 54, one sees that there are 17 fractional bits b. From (50), this implies that no more than five decimal places can be represented accurately; thus, if one wants to represent the fractional part of a binary number more accurately, then more fractional bits are necessary.

C.   SENSOR CALIBRATION

While testing the system, it was noticed that the values for voltage and current measured by Chipscope Pro were inaccurate when compared to those taken from a multimeter. It was deemed necessary to correct for some of the deviations within the digital algorithm. First, there was a problem with the scaling of the digital signals. After the analog-to-digital converter (ADC) samples the voltage and current, the conversion process normalizes them to a value between negative one and one. It is necessary to multiply this digital value by a corresponding gain in order to get the correct value. Theoretically, these gains should have been accurate, but they were not and had to be adjusted by multiplying them by a scaling factor. Also, there was a DC bias in the average value of the Chipscope measurements. After applying the gain and scaling factor, the algorithm attempts to add an offset to account for this bias. The gains, offsets, and scaling factors are documented in Appendix A. While this technique proved fairly useful, it was not perfect. One can see that some of the measurements were not correct. For instance, when the system is turned off, the current still reads about 33 mA.

D.   DIGITAL FILTERING

The presence of noise made it difficult to run the MPPT algorithms since it was unable to produce precise measurements for the input voltage and current. This noise was due to many possible factors. For instance, the quantization process inherently caused random errors in the value of the measurements. Since the ADC has to, in essence, round the sampled value to a discrete value, the true value is lost, and error is introduced. Additionally, the components used to measure these values are not perfect; thus, they impart some added uncertainty to the measurements. Moreover, the converter introduces a ripple on the input voltage and current due to the switching taking place. While the

ripple is not random, it does produce a deviation from the average value. If one measures these values in the presence of a substantial ripple, then the measurements can appear to be grossly different from the average values that are desired. Lastly, small changes in temperature can cause the voltage and current to fluctuate randomly with noise.

As recorded in laboratory testing, the voltage measurements showed a standard deviation of about 0.07 V at any constant voltage level. Also, the current measurements for the boost converter had a standard deviation of approximately 0.05 A at high current settings around 2.35 A. In addition, the current measurements for the interleaved boost converter showed a standard deviation of about 0.08 A at high current settings. It makes sense that the interleaved boost converter has a higher standard deviation. Since the IBC has an additional transistor, it produces more noise. When the current was fairly low, at about 0.4 A, the standard deviation was in the vicinity of 0.01 A.

1. First-Order Digital Filter

Consequently, a digital filter was added to the algorithm in order to smooth out the measured values. The filter took care of two main things. First, it drastically mitigated the noise that was present in the measurements. Also, it attenuated the ripple that was present due to the switching action of the converter. For simplicity and ease of computation, a first-order infinite impulse response (IIR) filter was used. This type of filter can be described with the difference equation

$$y[n+1] = \left(2\pi f_c T_s\right) x[n] + \left(1 - 2\pi f_c T_s\right) y[n], \tag{51}$$

where f_c is the cutoff frequency and T_s is the sampling period.

In order to understand how this difference equation was developed, the following derivation is presented in line with [34]. First, consider the transfer function of a low-pass filter in the Laplace domain such as

$$\frac{Y(s)}{X(s)} = \frac{2\pi f_c}{s + 2\pi f_c}. \tag{52}$$

If (52) is converted back into its time-domain equivalent, one gets

$$\frac{dy(t)}{dt} + \left(2\pi f_c\right) y(t) = \left(2\pi f_c\right) x(t). \tag{53}$$

Using the forward-difference relation to obtain an expression for the time derivative as done in [34], one can write

$$\frac{dy(t)}{dt} = \frac{y(t+T_s) - y(t)}{T_s}. \tag{54}$$

Furthermore, if one were to let $t = nT_s$ in accordance with [34], one obtains the corresponding discrete-time domain equation

$$\frac{y[nT_s + T_s] - y[nT_s]}{T_s} + (2\pi f_c) y[nT_s] = (2\pi f_c) x[nT_s]. \tag{55}$$

Applying some algebra and allowing T_s to be implied when inside brackets, one gets

$$y[n+1] = y[n] - (2\pi f_c T_s) y[n] + (2\pi f_c T_s) x[n], \tag{56}$$

which is the same result as found in (51). Using this difference equation, one can implement a first-order IIR digital filter in Simulink with the Xilinx blockset. In Figure 55, the graphical layout of the filter is depicted.
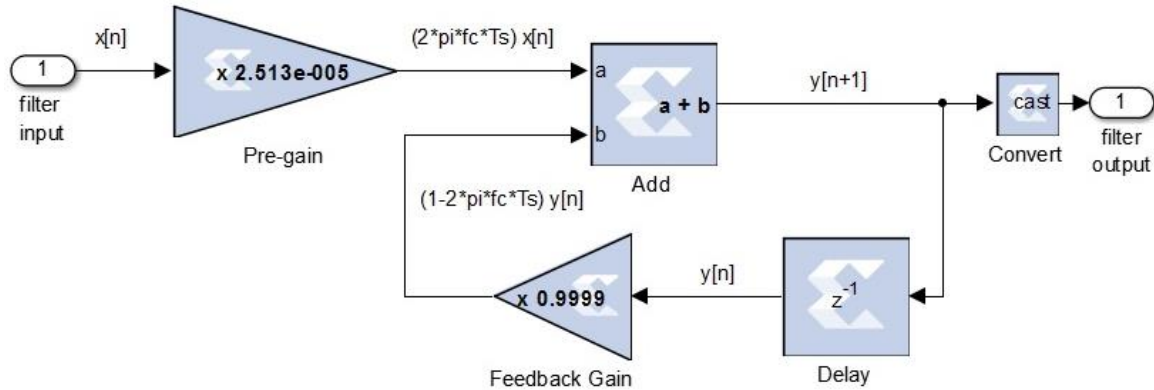
Figure 55.   First-order infinite impulse response filter constructed in Simulink
using the Xilinx blockset.

For this thesis, a cutoff frequency of 100 Hz was used to attenuate the noise. While this may seem like a very low cutoff frequency, it proved to be necessary. Furthermore, it must be noted that it was not necessary to reconstruct every fine detail of the desired signal. It was only important that the algorithm could detect relative changes in the voltage and current. Thus, it was possible to filter out some of the desired signal in order to adequately suppress the unwanted noise, while ensuring that the algorithm still

worked. In Figure 56, the frequency response for this filter with a cutoff frequency of 100 Hz is displayed in linear magnitude format. In this plot, a few things must be pointed out. For one, below the cutoff frequency, at least 70% of the original signal's amplitude remains. This is important because this is where most of the desired signal lies. At the switching frequency f_{sw} and higher, the signal's amplitude is attenuated by a factor of 0.01 or less. This means that the ripple due to switching as well as the noise that is at that frequency or higher is diminished a great deal. Lastly, this plot shows that the digital low-pass filter that was designed functions as expected.

2.   Results of Filtering

Incorporating this first-order IIR filter was very successful. Additionally, it allowed the algorithm to run effectively. If the filter was not used, and the noise remained at its unfiltered levels, this entire research would not have been possible. The frequency response of the first-order IIR filter in linear magnitude format is displayed in Figure 56. From this plot, one observes how the higher frequency components are designed to be attenuated. An example of how this filter suppressed the noise is illustrated in Figure 57. To create this plot, the measurement noise was incorporated into the Simulink model by using the random number block. The simulation generates a Gaussian random number that is scaled appropriately based on the standard deviation in the unfiltered voltage (or current) measurements. Then it adds that random number to the true value of the measured parameter. Even though this was a simulation, one can see the difference between the unfiltered voltage and the filtered voltage. The unfiltered voltage, shown in blue, has excessive deviations in voltage from the filtered value. As pointed out earlier, this would potentially confuse the MPPT algorithm and make it virtually impossible to control the power from the solar panel. In contrast, the filtered voltage, shown in red, more accurately represents the true value of the actual voltage. Using this signal, one can adequately control the solar panel with little problems due to noise.
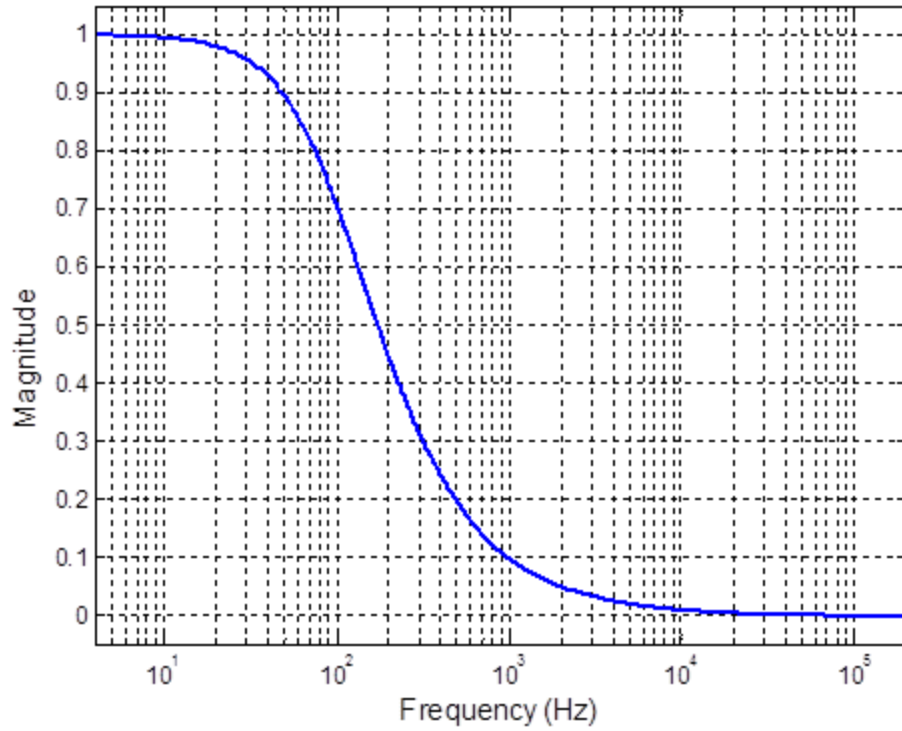
Figure 56.   Frequency response of the first-order IIR filter in linear magnitude
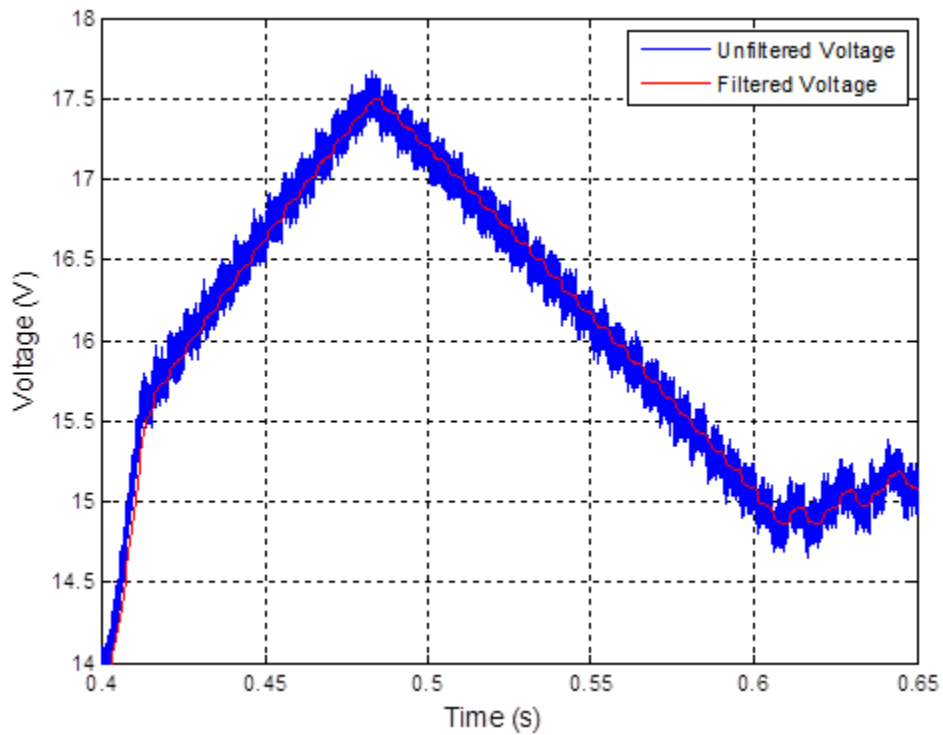format.

Figure 57.   Filtered input voltage superimposed on the unfiltered input voltage.

E. MPPT ALGORITHMS AND DUTY CYCLE CONTROL USING XILINX BLOCKSET

At first, the MPPT algorithms were developed using strictly Simulink blocks, but then they were converted to Xilinx blocks so that they could be loaded into the FPGA. In Figures 93 and 94 from Appendix B, the MPPT algorithms using the Xilinx blockset are displayed. Here, it can be observed that there are three distinct stages to the algorithm. First, the algorithm calculates the desired variables in accordance with the respective MPPT algorithm as detailed in Figures 34 and 36. Here, it is necessary to calculate the change in power $\varDelta P$, the change in voltage $\varDelta V$, or the change in current $\varDelta I$. To do that, registers, which operated at the MPPT frequency, were utilized. Also, a delay block was placed between the registers to guarantee that the correct data was sampled when determining the $\varDelta V$, $\varDelta I$, or $\varDelta P$. Next, the algorithm compares these variables against certain programmed settings to produce logic signals. Finally, these logic signals go to a multiplexer or a set of multiplexers, which cause the algorithm to output a number that changes the control variable. The MPPT algorithm block yields a value of one to increase the control variable, a value of negative one to decrease the control variable, or a value of zero to keep the control variable the same. From there, the output from the MPPT algorithm, which is entitled "increment," is passed onto the direct duty cycle control block that can be analyzed in Figure 58. Here, the "increment" is multiplied by the specified amount for the change in duty cycle $\varDelta D$, which is 0.005 in this case. Consequently, the possible results are 0.005, −0.005, or 0 assuming the incremental conductance algorithm is being used. A register block is employed to sum up these changes to the duty cycle. This summation occurs at the MPPT frequency f_{MPPT} and is used to find the commanded duty cycle. Basically, the register holds its previous value until the next MPPT period. At that point, it updates its value, which gets added to the new value for the change in duty cycle. This summation is then passed through the register again at the next MPPT clock cycle. Next, as is shown in Figure 58, an initial condition for the duty cycle is added to this summation to find the commanded duty cycle D. Also, the block entitled "Limits on D" sets saturation limits on the values for D and is presented in Appendix B. In the end, this block outputs the commanded duty cycle D, which is forwarded to the pulse width modulation (PWM) block.
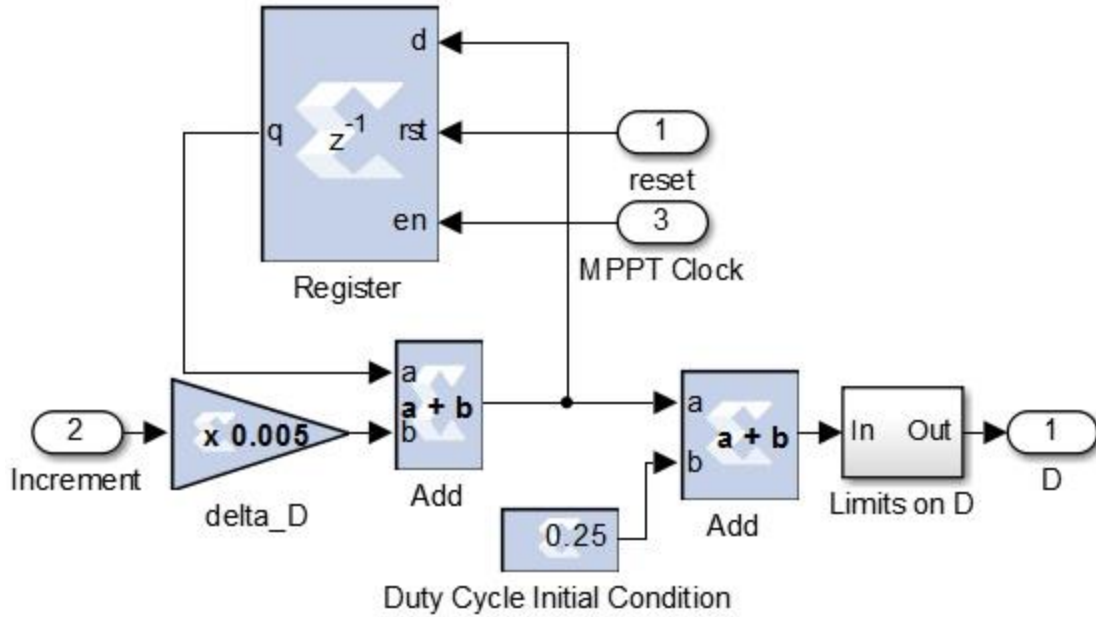
Figure 58.   Method used for direct duty cycle control in Simulink using the
Xilinx blockset.

F.   PULSE WIDTH MODULATION SCHEME

The pulse width modulation scheme, which is used to formulate the logic signals that are sent to the driver circuits, is described in this section. This scheme generated a digital triangle wave with the Xilinx blockset in order to create the signals that are compared against the instantaneous duty cycle. In Figure 59, one can see the overall construction of the PWM scheme.
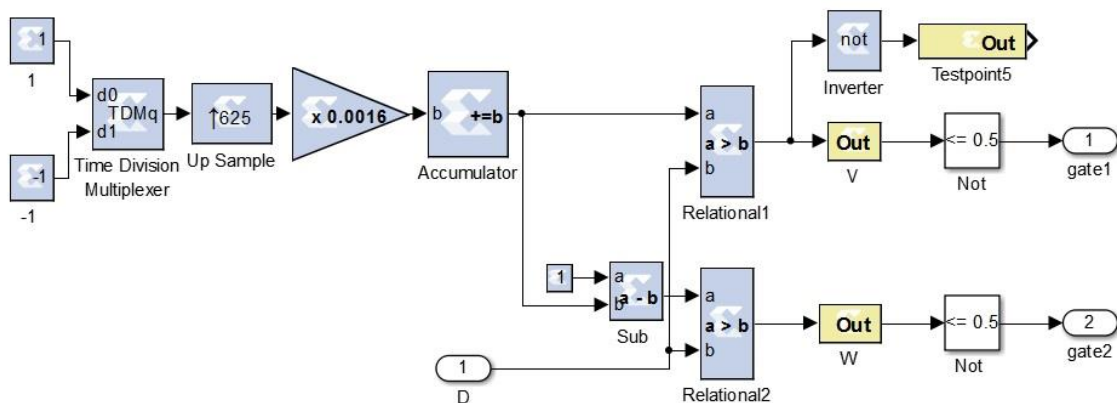
Figure 59.   PWM scheme used to drive the gate signals.

The triangle wave is produced by using a time-division multiplexer that switches between one and negative one. It does this at a time interval that corresponds to half of the switching period T_{sw}. Next, the output from the multiplexer is up-sampled 625 times within half of T_{sw}. This makes it so that the samples coming from the multiplexer are at the clock's rate of 25 MHz. After that, the signal must be multiplied by 1/625 so that the accumulator integrates the signal as desired. Over one switching period T_{sw}, this produces a triangle wave that starts at zero, ramps up to one, and then ramps down back to zero. From there, an interleaved triangle wave is made for the realization of the IBC. Here, the wave must be shifted in time by half of T_{sw}. To do this, a simple mathematical trick was employed. The original triangle wave is inverted by multiplying it by negative one. Then, an amount equal to its amplitude, which is a value of one in this case, is added to this inverted triangle wave. The resulting signal is a triangle wave with the desired phase shift. After that, the two triangle waves are compared against the instantaneous duty cycle to make the appropriate logic signals for each phase.

The logic signals that are sent to the gate drivers on the actual hardware are the inverse of what is normally used. For instance, when this logic signal is high, the switch is actually turned off. When this signal is low, the switch is turned on. While this is counterintuitive, this is how the design of the gate drivers was meant to operate. In the simulation as well as what is seen on the oscilloscope, this convention was reversed by the NOT gates, which inverted the logic signals, as is evident in Figure 59.

THIS PAGE INTENTIONALLY LEFT BLANK

IV. MODELING AND SIMULATION

A. MODELING

The purpose of this chapter is to explain the modeling and simulation used in this thesis. More specifically, the simulation tools used are described in detail and the results of those simulations are presented.

1. Modeling the Power Converters using SimPowerSystems in Simulink

SimPowerSystems is a special and powerful library of electrical components and analysis tools within Simulink that can be assembled to model virtually any electrical power system [35]. It is a simple and convenient method to simulate a power converter. One merely has to assemble the correct parts in the appropriate place within the schematic. In addition to laying out the system correctly, certain settings within each component must be modified to represent the desired characteristics. In Figure 60, one sees how the entire system is laid out. Starting from the left, the solar panel is modeled as a variable current source since the variable that it receives from the solar panel model is a current. In addition, each component of the IBC is assembled exactly as the schematic from Figure 21. In the simulation, the inductors are assumed to be lossy while the capacitors are not. Accordingly, the inductor has an equivalent series resistance (ESR), and the capacitors do not. Of note, the battery is modeled as a DC voltage source with an ESR. This allowed the output voltage to resemble the real system to some extent. The IGBTs and diodes have several settings, which are all detailed in Appendix A. One of these key features is the fact that both the IGBTs and diodes can be set up to accommodate losses. In other words, the user can enter an on-state resistance and forward voltage drop for these components. Finally, the measurement blocks, which have a plus sign and a minus sign on them, simply enable the simulation to record and report the value of certain parameters; hence, these blocks are not akin to actual voltage or current sensors that affect the system. As a final point, the 2nd generation of SimPowerSystems was used in this thesis.
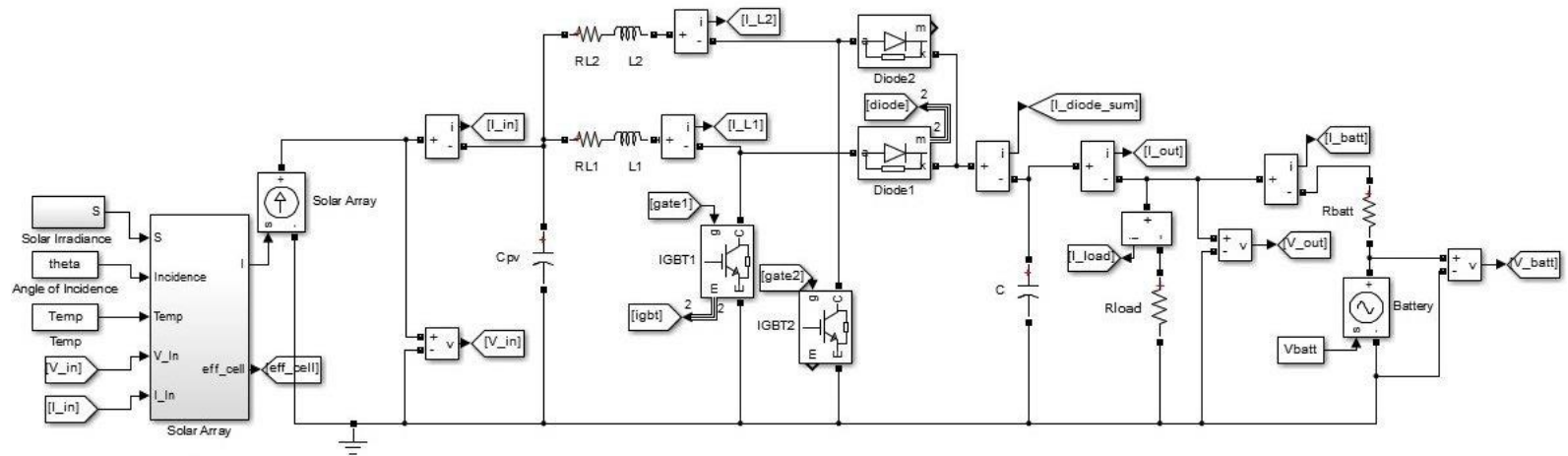
Figure 60.   IBC in Simulink using the SimPowerSystems blockset.

2.   Solar Panel Model in Simulink

In this next section, the modeling of the solar panel is explained. Since most of the theory and equations were presented in Chapter II, this section focuses on how those equations were constructed in Simulink. In Appendix B, one can examine the way the solar model equations were implemented using Simulink. This model accepts the solar irradiance, the temperature, the angle of incidence, the input voltage, and the input current as inputs. As stated before, this method takes the input voltage and current and finds the equivalent voltage and current on one cell assuming all other cells are operating the same. From there, it implements the equations that govern the solar cell. Equations (3) and (4) can be seen at the top of Figure 91, and in Figure 92, (5) can be identified. The model is built to accept the two-diode model, so it may seem like there are two versions of (5) within Figure 92. In this thesis research, only the single-diode model was used by setting the reference reverse saturation current for diode #2 $I_{s2,ref}$ to zero as seen in Appendix A. Equation (6) is throughout this entire model in various elements, which can be recognized in both Figures 91 and 92. After executing the equations, the current through the entire array is calculated as described in Chapter II near (7). Additionally, this model finds the solar cell efficiency, which is the amount of power the panel puts out divided by the amount of power incident upon its surface. This calculation can be seen in the lower right portion of Figure 92. Finally, it outputs the updated input current as well as the solar cell efficiency.

B.   SIMULATION

In this section, the specific details of the simulation profile and parameters are described. The results of these tests are presented and explained thoroughly. For instance, the speed of each algorithm's power response is analyzed, and how each algorithm tracked the MPP is shown. Furthermore, differences in the two algorithms are pointed out. Of note, these simulation results only concentrate on the interleaved boost converter because it is one of the main emphases of this thesis.

1. Simulation Parameters

The parameters used for the simulation exactly match those contained in Table 3, but there are a few extra component values that have to be defined. In Table 7, the additional parameters used in the simulation are shown. While Table 7 in conjunction with Table 3 is very comprehensive, the complete list of all variables used for the simulation is contained in Appendix A.

Table 7.   Additional parameters used in the simulation.

Parameter	Symbol	Value
Initial Input Voltage	$V_{IN}\,IC$	19.77 V
Initial Output Voltage	$V_{OUT}\,IC$	23.77 V
Inductor Resistance	R_L	0.25 Ω
Diode Resistance	R_{diode}	0.15 Ω
Diode Forward Voltage	VF_{diode}	0.6 V
IGBT Resistance	R_{IGBT}	0.15 Ω
IGBT Forward Voltage	VF_{IGBT}	1.2 V
Battery Voltage	V_{BATT}	24.0 V
Battery Resistance	R_{BATT}	0.175 Ω
Solar Cell Temperature	$Temp$	50 °C

In Figure 61, a typical profile for the simulated solar irradiance is displayed. In the simulation, the initial solar irradiance is 1000 W/m^2 while the PV system attains the initial MPP setting. After that, the irradiance is dropped to 200 W/m^2 for a period of time to see how the simulated system performs at a lower power setting. Eventually, it is raised back to 1000 W/m^2 where it stays until the end of the simulation. The transitions are admittedly somewhat unrealistic, but the main intent is to see how the algorithms function in the steady-state. Additionally, the solar cell's temperature was assumed to be 50 °C. While this temperature may be a bit higher than experienced in this thesis, it simulates the performance of the system in a slightly warmer condition.
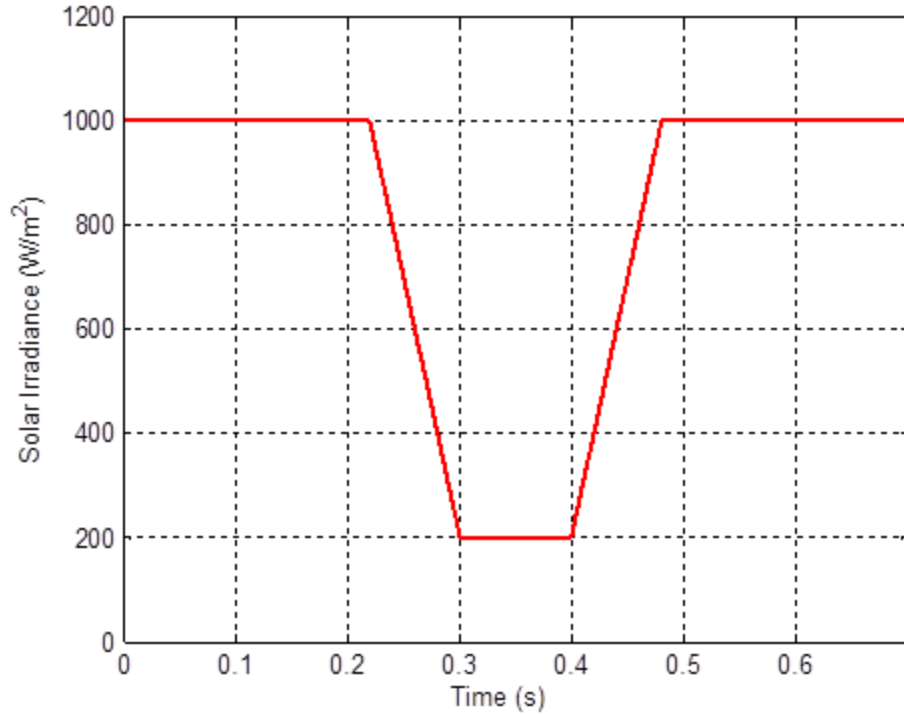
Figure 61.   Typical solar irradiance versus time profile used during the
simulations.

2.   Perturb and Observe Simulation Results

In this subsection, the P&O simulation results are discussed. First, the various plots of current, voltage, duty cycle, and power are examined. In Figure 62, the input current and the output current are shown versus time. Comparing this with Figure 61, one notices that the input current and the output current directly respond to the amount of irradiance present on the solar panel. Also, the load current, which is the current through the resistive load, stays essentially constant throughout the simulation. When the irradiance falls to 200 W/m^2, the output current from the converter decreases by about 1.0 A. Thus, an alternate source of power such as a battery, which is depicted in Figure 21, must supply the difference.

89
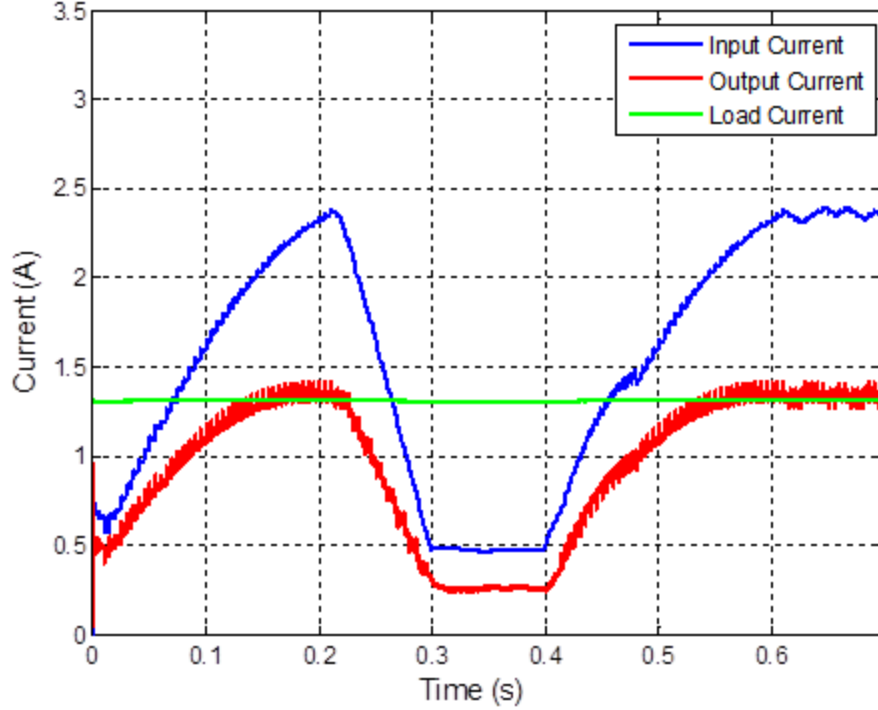
Figure 62.   Current versus time for the P&O simulation using the IBC where ΔD
equals 0.005 and f_{MPPT} equals 200 Hz.

Next, the duty cycle versus time in Figure 63 and the voltage plots versus time in Figure 64 are analyzed. At the start, one can see that the initial duty cycle is at 25% but rapidly climbs to the MPP. In Figure 64, the plot of the input voltage versus time illustrates its inverse relationship with respect to duty cycle. One observes that the voltage starts at the V_{oc} and is quickly reduced to the V_{MPP}. Here, the MPP was at a voltage of approximately 15.15 V. As the irradiance changes, the duty cycle is changed appropriately to find the new MPP. From 0.3 to 0.4 seconds, the system oscillates about the new MPP voltage, which is 14.23 V in this case. Next, the irradiance goes back up, and the system adjusts itself to the original MPP. During the last 0.1 seconds of the simulation, the P&O algorithm oscillates around the original MPP. To get a better idea of what this looks like, a zoomed-in version of the input voltage versus time plot is shown in Figure 65. One sees that the voltage is commanded by the P&O algorithm to fluctuate about the MPP voltage of 15.15 V.

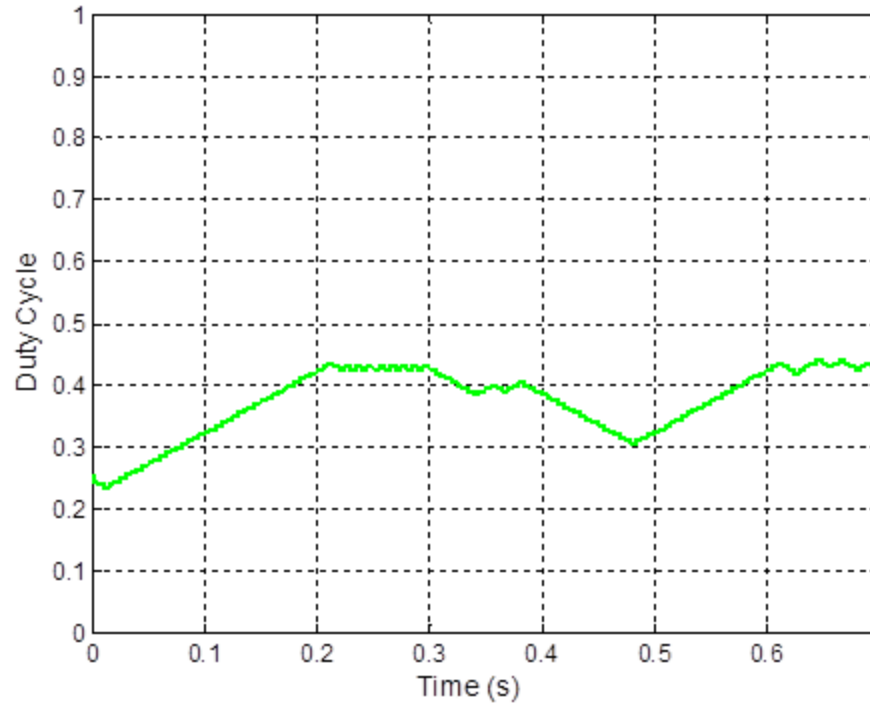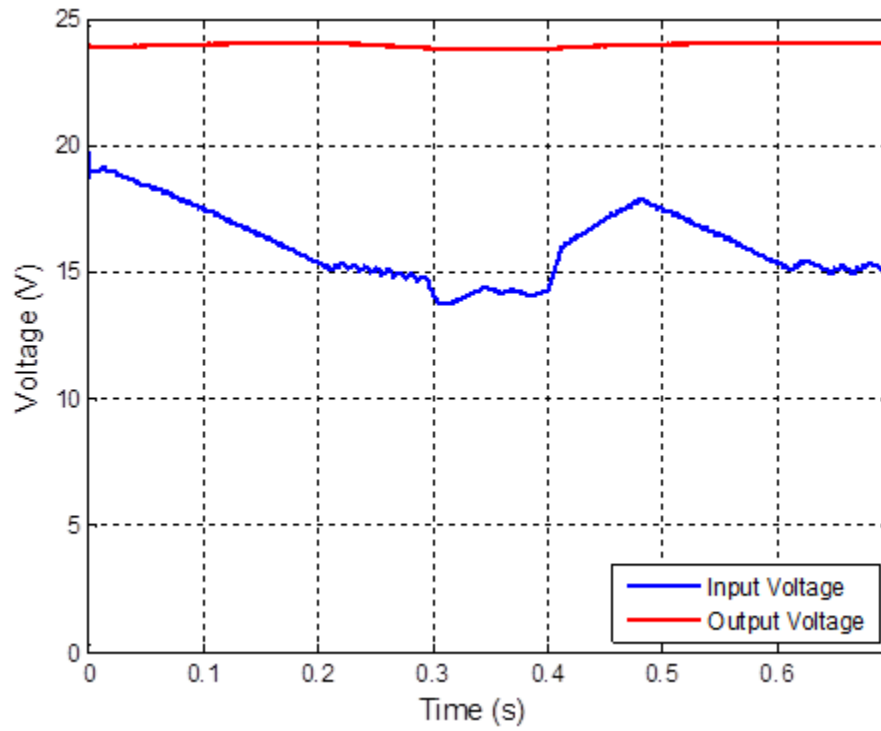Figure 63.　Duty cycle versus time for the P&O simulation using the IBC where $\mathit{\Delta D}$ equals 0.005 and f_{MPPT} equals 200 Hz.

Figure 64.　Voltage versus time for the P&O simulation using the IBC where $\mathit{\Delta D}$ equals 0.005 and f_{MPPT} equals 200 Hz.

91
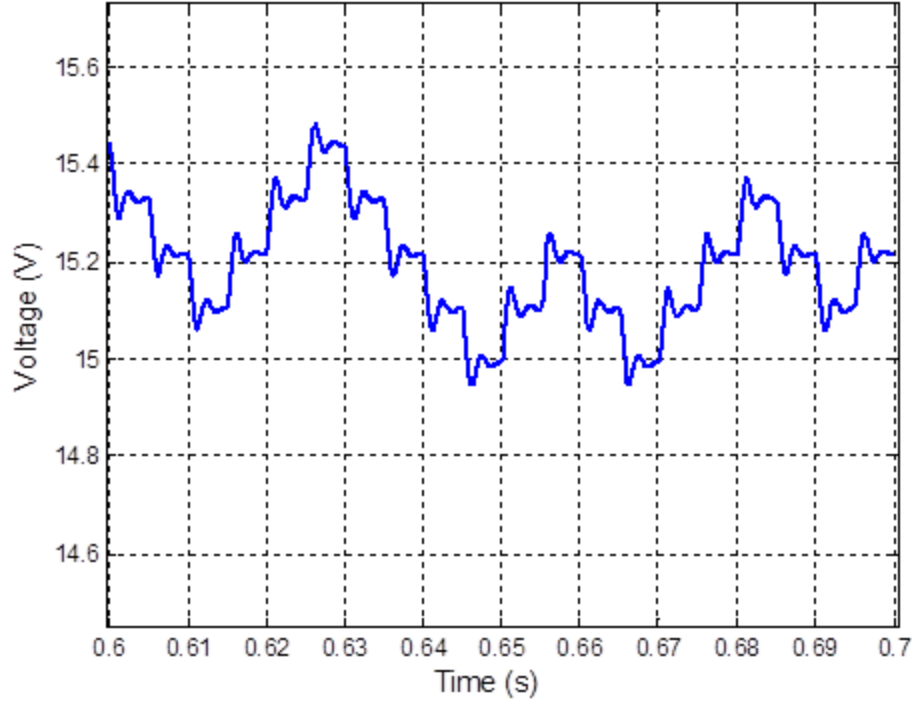
Figure 65.   Zoomed-in version of the input voltage versus time for the P&O
              simulation using the IBC where ΔD equals 0.005 and f_{MPPT} equals
              200 Hz.

Next, the input and output power curves versus time are displayed in Figure 66. Here, the amount of input power harvested from the solar panel as well as the amount of output power coming out of the converter is shown in Figure 66. Similar to the current, the power essentially mirrors the solar irradiance from Figure 61.

The power versus time plots for various control settings are compared against each other in Figure 67. While one can learn some key things from Figure 67, it is easier to comprehend what is shown by calculating the settling time for each of these plots. In the traditional context, the settling time is the time it takes for the system to reach 2% of its final value. In Table 8, the settling time of the power response is tabulated for various P&O settings. This set of data in Table 8 can be interpreted as the speed of the algorithm. Essentially, it documents how fast the algorithm reached 2% of its steady-state value from when the system was turned on. As expected, the settling time increases when the ΔD or the f_{MPPT} decrease, and vice versa.

92
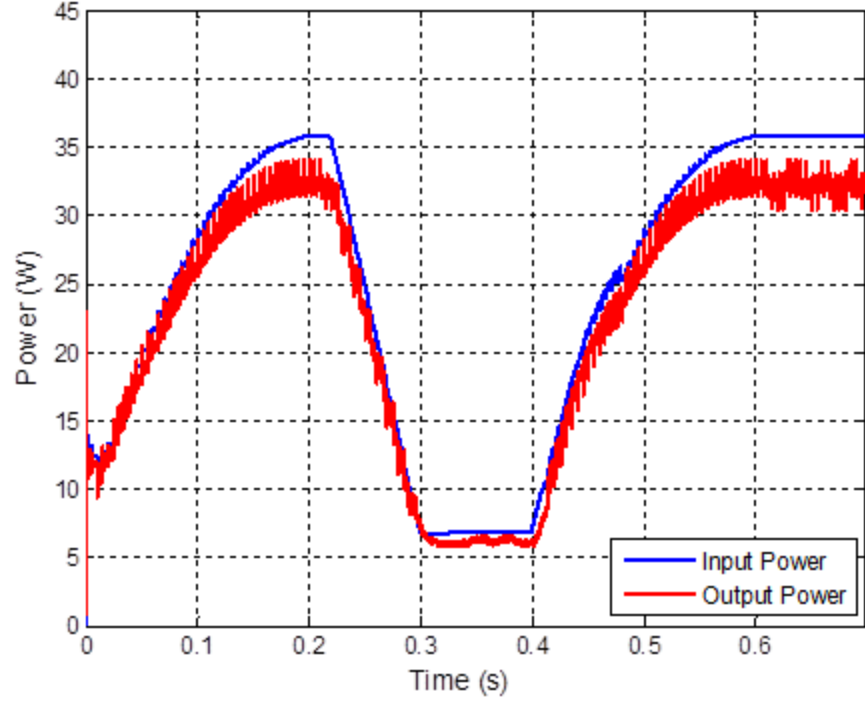
Figure 66. Power versus time for the P&O simulation using the IBC where ΔD equals 0.005 and f_{MPPT} equals 200 Hz.
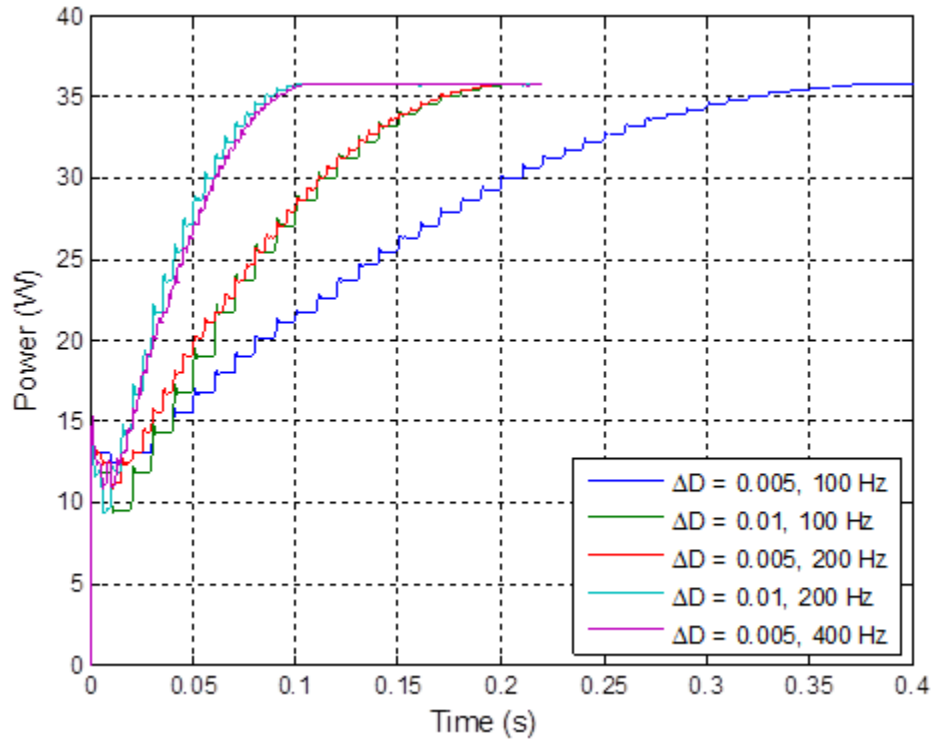
Figure 67. Input power versus time for the P&O simulation using the IBC under various settings.

Table 8.   Settling time of the input power for the P&O simulation using the IBC under various settings.

Scenario	Settling Time (s)
$\mathit{\Delta}D = 0.005, f_{MPPT} = 100$ Hz	0.3302
$\mathit{\Delta}D = 0.01,\ \ f_{MPPT} = 100$ Hz	0.1802
$\mathit{\Delta}D = 0.005, f_{MPPT} = 200$ Hz	0.1752
$\mathit{\Delta}D = 0.01,\ \ f_{MPPT} = 200$ Hz	0.0902
$\mathit{\Delta}D = 0.005, f_{MPPT} = 400$ Hz	0.0928

Finally, the power versus voltage data is analyzed. In Figure 68, the plot of the power versus voltage is displayed. With the simulated data, two theoretical curves are shown as well. One of them is the power versus voltage curve when the solar irradiance is 1000 W/m^2. The other one is based on when the solar irradiance is 200 W/m^2.
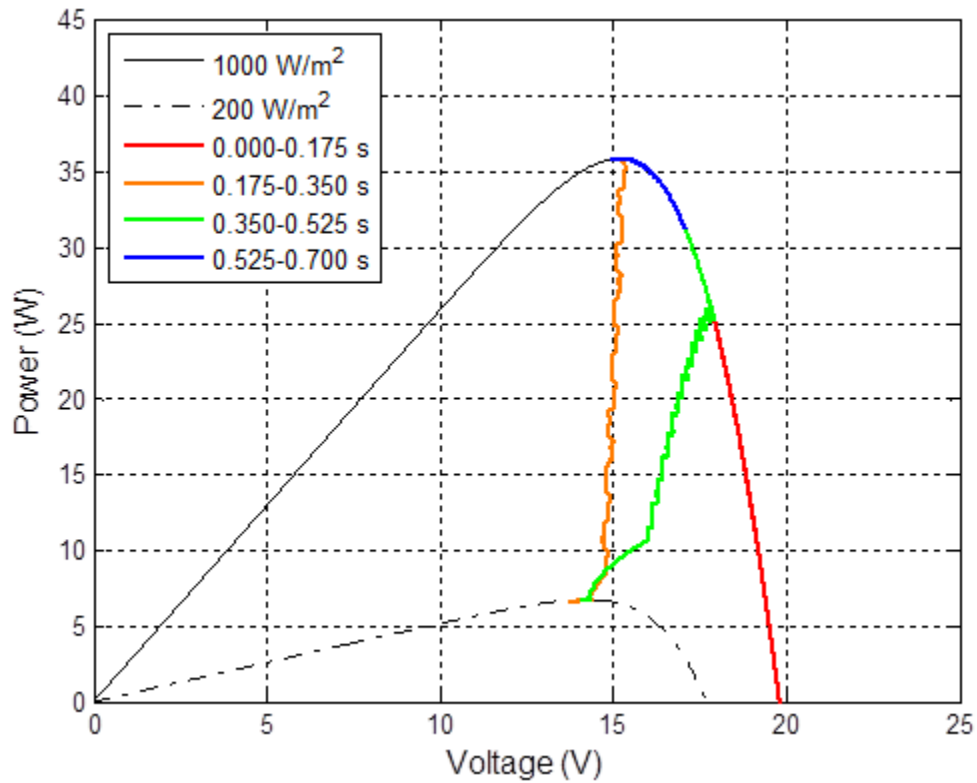
Figure 68.   Power versus voltage for the P&O simulation using the IBC where $\mathit{\Delta}D$ equals 0.005 and f_{MPPT} equals 200 Hz.

Additionally, a color code that can be comprehended using the legend is used in Figure 68. To clarify, the different colors represent the different times within the

simulation. For example, the red color corresponds to time in the simulation from 0.0 to 0.175 seconds. This color code aids the reader in determining the chronological order of the data within the curve. For instance, the simulation initially rises towards the MPP according to the red line. When the irradiance is reduced, the orange line depicts the power falling as the voltage slightly decreases. Next, one observes that the simulation operates in the vicinity of the MPP at 200 W/m^2. After that, the green and blue lines show how the simulated system recovers to the original MPP.

3. Incremental Conductance Simulation Results

In this section the results from simulating the IC algorithm with the IBC are presented. First, the current plots are shown versus time in Figure 69. Notice how this looks essentially the same as the current plots in Figure 62. The main difference is that the IC algorithm locks onto a specific setting at the maximum power point. Thus, the input and output currents stop fluctuating so much.

Figure 69.   Current versus time for the IC simulation using the IBC where $\varDelta D$ equals 0.005 and f_{MPPT} equals 200 Hz.

In Figures 70 and 71, the duty cycle versus time and the voltage curves versus time, respectively, are shown. Initially, when the irradiance is 1000 W/m^2, the duty cycle rises to acquire the MPP. As expected the input voltage quickly falls to lock onto to a voltage of 15.216 V, which is very close to the MPP voltage of 15.15 V. After the irradiance is lowered, the duty cycle is adjusted in an attempt to find the new MPP. At 200 W/m^2, the system does not successfully find a definite operating point. Instead, it fluctuates slightly below the MPP voltage. From there, the irradiance rises, and the duty cycle is adjusted to return the system to the original voltage of 15.216 V. Even though the system does not perfectly find the MPP, the system still operates sufficiently close to the MPP so that almost all of the available power is harvested. Specifically, the system is around 4 mW shy of the MPP. Next, the input power and the output power are plotted versus time in Figure 72. Here, one sees that these plots are very similar to the power versus time graphs from the P&O simulation; however, there is less variation in the output power once the IC algorithm locks onto its operating point.
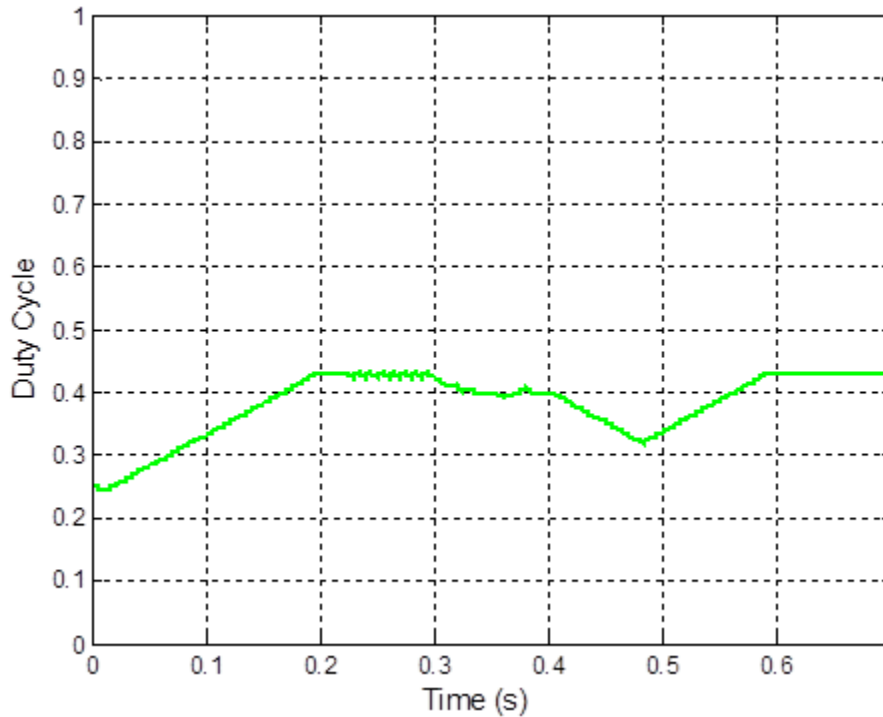
Figure 70.   Duty cycle versus time for the IC simulation using the IBC where ΔD equals 0.005 and f_{MPPT} equals 200 Hz.

96
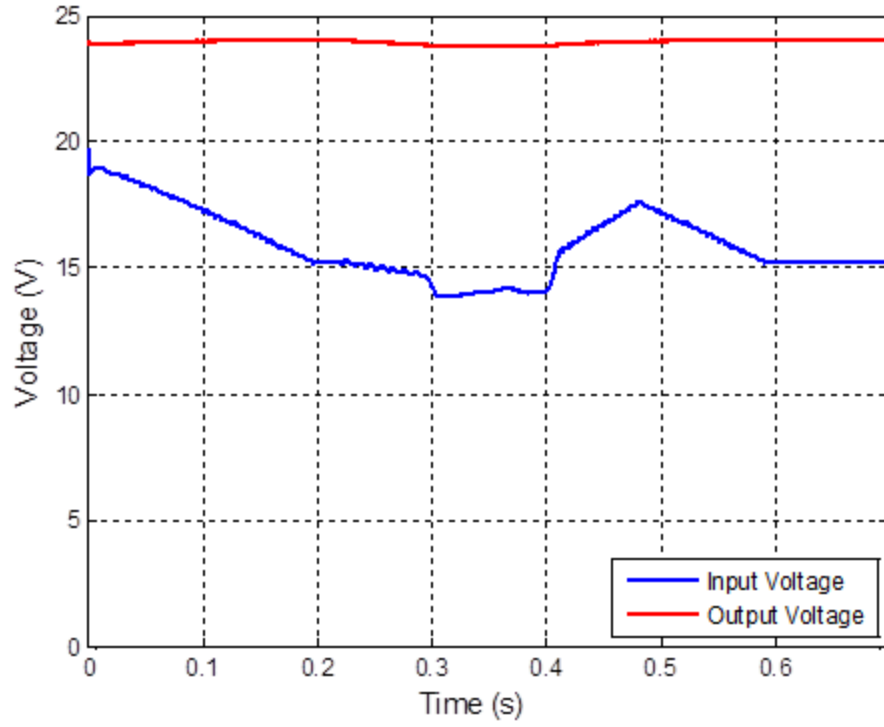
Figure 71. Voltage versus time for the IC simulation using the IBC where ΔD equals 0.005 and f_{MPPT} equals 200 Hz.
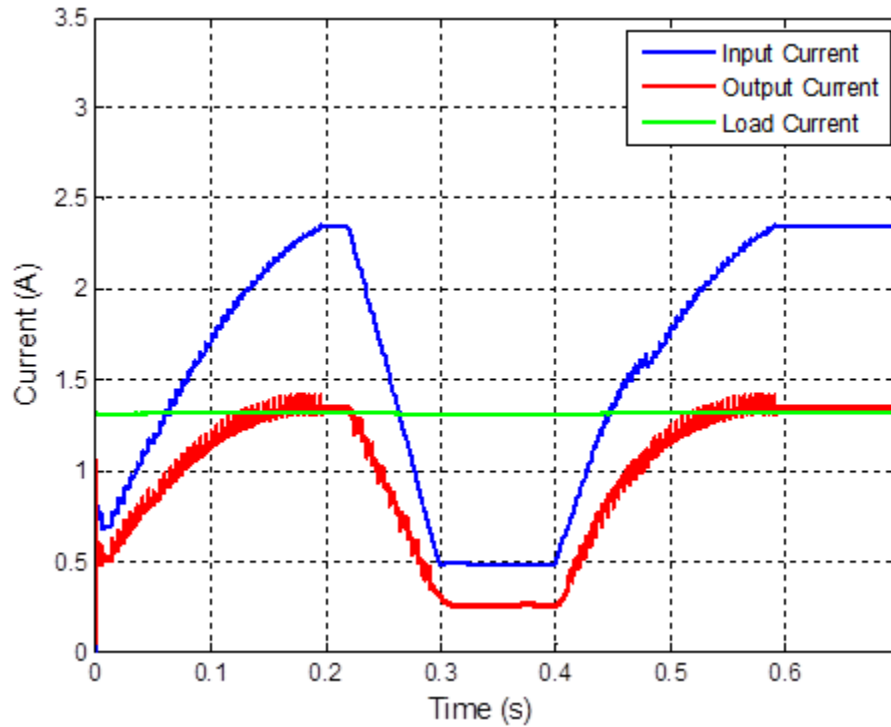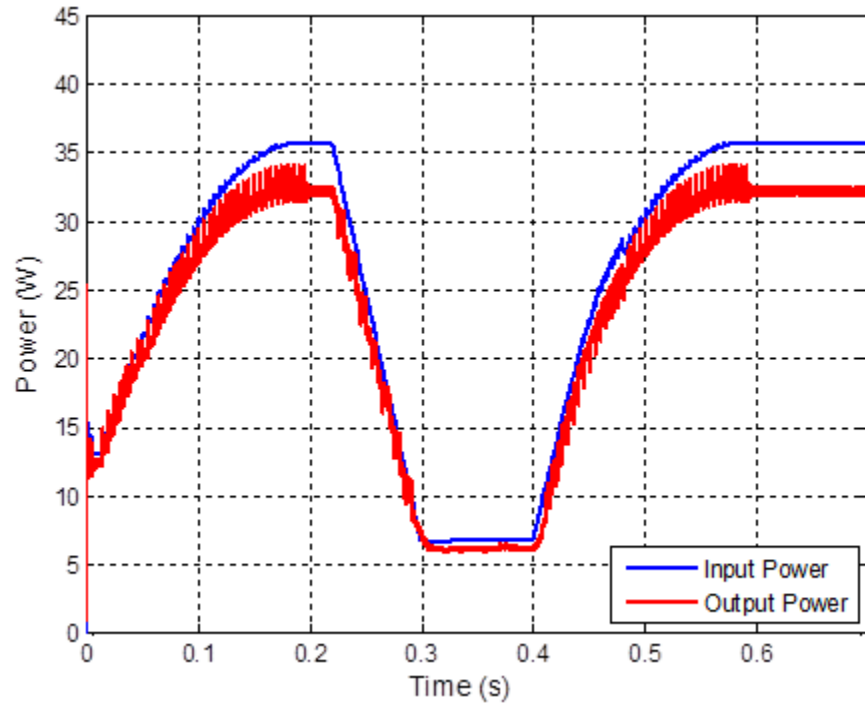

Figure 72. Power versus time for the IC simulation using the IBC where ΔD equals 0.005 and f_{MPPT} equals 200 Hz.

In Figure 73, the input power versus time plots for numerous settings are juxtaposed with each other. Again, these plots look similar to the simulated results from Figure 67 in the P&O section. In Table 9, the settling times for each of the settings used in the simulation are summarized. It is interesting to note that both the P&O and the IC algorithms performed similarly. In simulation, the IC algorithm had a slightly faster settling time than the P&O algorithm.
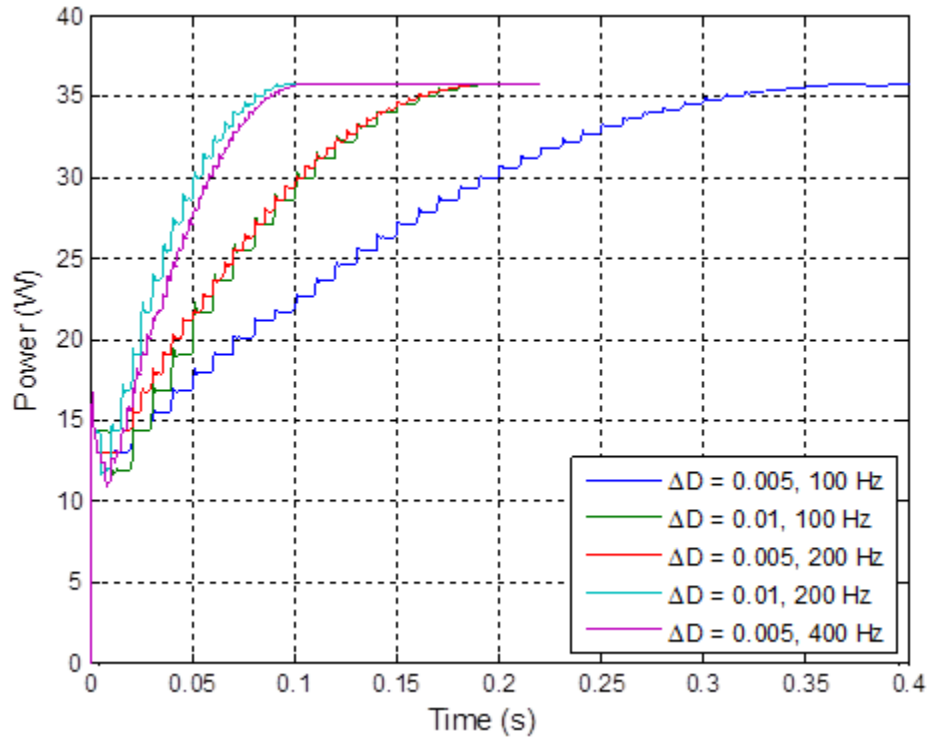
Figure 73. Input power versus time for the IC simulation using the IBC under various settings.

Table 9. Settling time of the input power for the IC simulation using the IBC under various settings.

Scenario	Settling Time (s)
$\Delta D = 0.005, f_{MPPT} = 100$ Hz	0.3202
$\Delta D = 0.01, \ f_{MPPT} = 100$ Hz	0.1702
$\Delta D = 0.005, f_{MPPT} = 200$ Hz	0.1652
$\Delta D = 0.01, \ f_{MPPT} = 200$ Hz	0.0852
$\Delta D = 0.005, f_{MPPT} = 400$ Hz	0.0903

Lastly, in Figure 74, the power versus voltage plot is presented. In this graph, it can be deduced that the IC algorithm's performance is almost identical to the performance of the P&O algorithm. The main point is that the IC algorithm initially captures the MPP. When the irradiance is reduced, the algorithm makes adjustments in order to reduce voltage so that the system operates at the new MPP. Once the irradiance goes back up, the system returns to the original MPP.
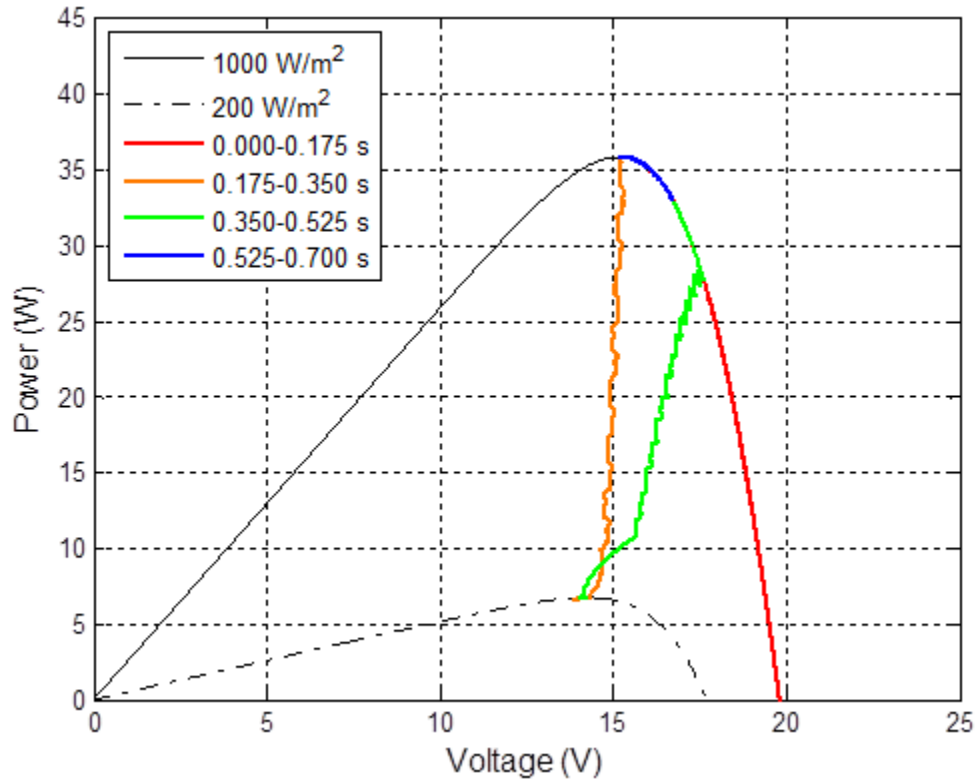
Figure 74. Power versus voltage for the IC simulation using the IBC where ΔD equals 0.005 and f_{MPPT} equals 200 Hz.

THIS PAGE INTENTIONALLY LEFT BLANK

V. EXPERIMENTAL TESTING

The purpose of this chapter is to describe the experimental testing that was conducted in this thesis. More precisely, the experimental setup is explained, and the results of those experiments are displayed.

A. EXPERIMENTAL SETUP

In order to understand how the experimental testing was conducted, one must first reference Figure 21. The main components of the PV system were connected as depicted in this schematic diagram of the interleaved boost converter except that a DC voltage source was used primarily instead of a battery. This was done to simulate a battery that had a consistent 24 V output voltage. It must be noted that the system was briefly hooked up to an actual battery in order to prove that it worked. During this short test, the system operated just the same as using the DC voltage source.

In Figure 75, a picture of the test setup is displayed. Here, one can see the overall layout of the different components and their physical relationship to one another. In this picture, one can see four multimeters, which were used to measure the voltage and current for the input and the output. Also, there is an oscilloscope that displayed various waveforms such as the inductor currents, the input voltage, the output voltage, the input current, the output current, and the gate signal for one of the transistors. Additionally, one can see that the solar panel was placed outside, and the wires were fed through the window. In Figure 76, one can see how the solar panel was set up on the ground with its wires hanging outside the window. Also, the resistive load is depicted in Figure 77. As one may ascertain, the resistive load is simply a number of resistors in parallel. In Figure 78, the FPGA boards, which were assembled above the power converter board, were temporarily separated from the IBC to expose the components of the power converter. One notices that this board is more than just the basic components of the power converter as depicted in Figure 21. There are several other components that are needed to make the IBC work, such as the gate driver circuits, voltage regulators, measurement devices, and a heat sink with a fan.
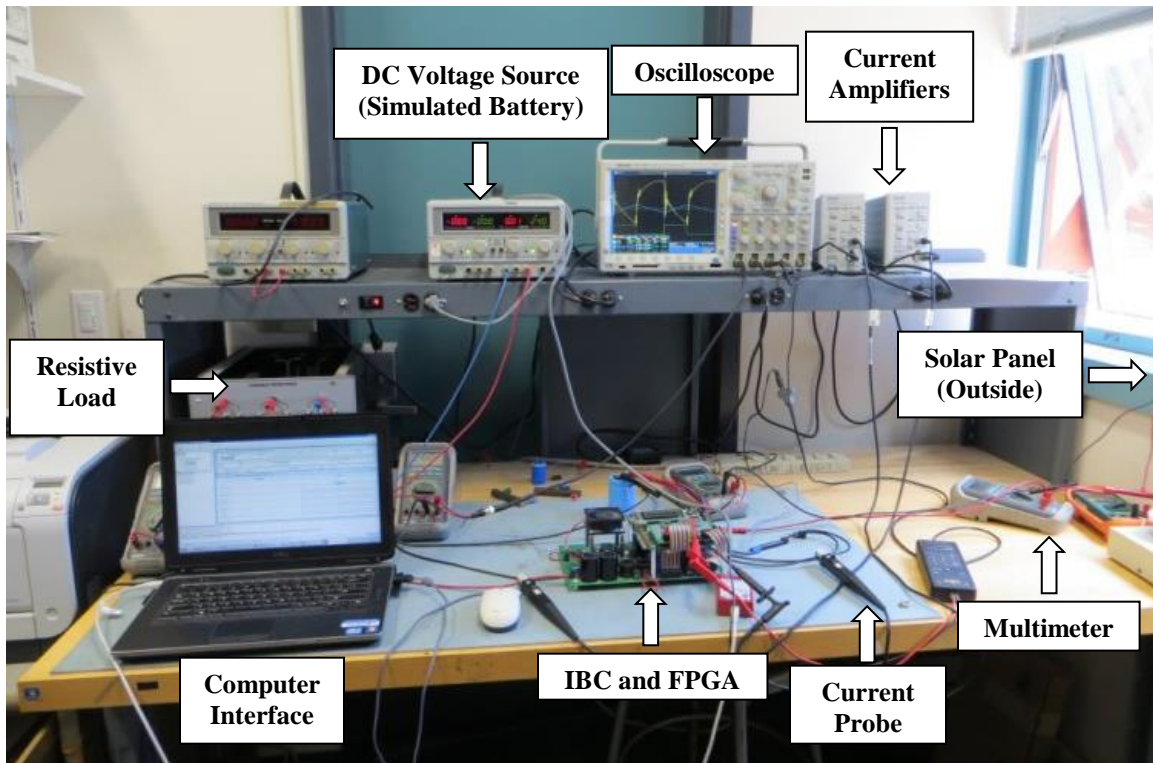
Figure 75.   Picture of the testing setup.

Figure 76.   Solar panel on the ground with the wires hanging outside the window.
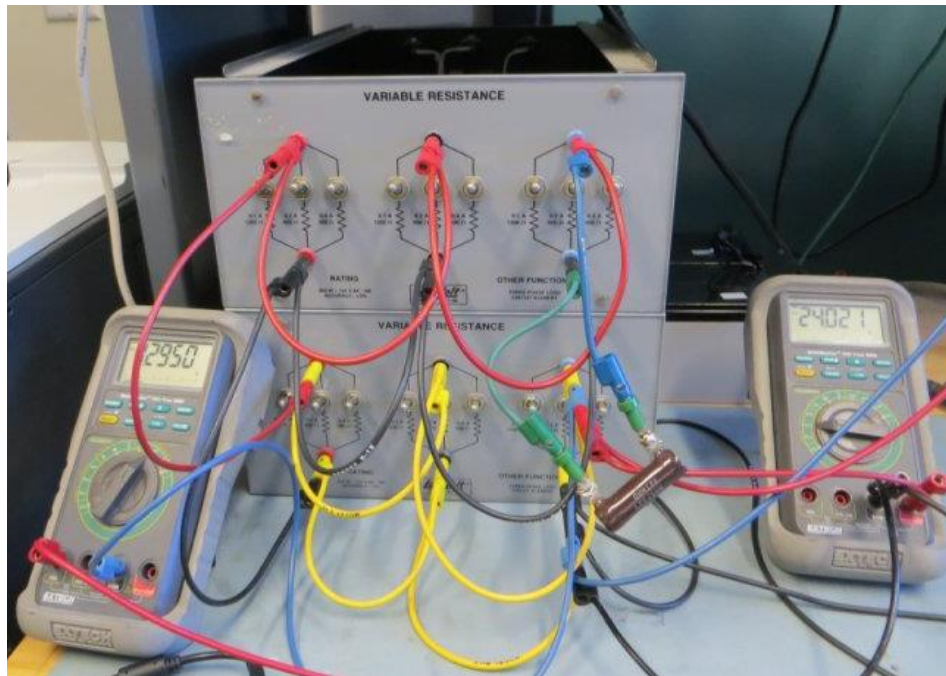
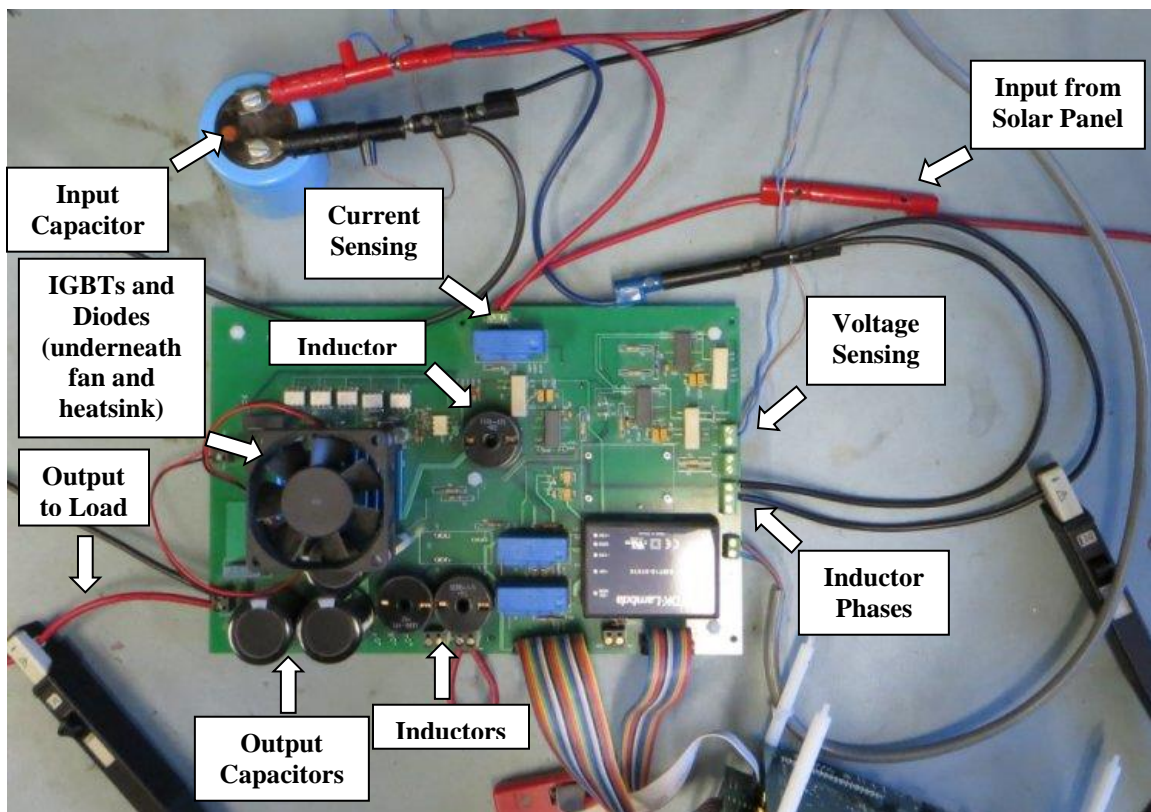Figure 77.   Resistive load with the output voltage and current meters.

Figure 78.   IBC exposed so that one can see the components of the power converter.

All of these miscellaneous parts were necessary to operate the converter, and that is what is seen in Figure 78. Lastly, one can discern the electrical connections that were made if one follows the wires. For example, one sees that the input from the solar panel is fed through a current sensing device and then goes to the input capacitor. From there, the wires split so that two separate phases connect with their respective inductors. In the vicinity of the output capacitors, a set of wires exists in order to feed the output current into the load and the simulated battery.

B.   TESTING

In this section, the testing of the PV system is explained, and the parameters used in the actual tests are described in detail. Similar to Chapter IV, certain results were analyzed, such as the speed of the algorithm under different control parameters and the ability of the system to track the MPP. It must be noted that mostly results from testing the interleaved boost converter are presented since the main focus of this thesis has been on the IBC. Nevertheless, at the end of this section, a comparison is made between the boost converter and the IBC with respect to ripple and efficiency.

1.   Testing Parameters

In this next section, the parameters utilized in the experimental testing are discussed. As for the components used in the testing of the PV system, they were the same as the theoretical values used in the simulation, and the numbers previously presented in Table 3 may be referenced once again for the experimental testing. There were several tests that were performed in order to see how the actual system responded. For instance, one of these tests involved turning the converter off and then back on to see how long it took for the system to reach full power. Additionally, the steady-state operation was analyzed. By recording voltages and currents at the input and the output while in the steady-state, the converter efficiency was verified. Another experiment involved looking at the waveforms for the inductor currents and output voltage in order to ascertain the ripple in each. Moreover, the operation of the system was investigated while the solar panel was experiencing a shading event. A shading event was created by

temporarily placing an object in front of approximately 1/5 of the solar panel so that a portion of the solar panel was covered from the sun.

2.   Perturb and Observe Experimental Results

In this portion of this chapter, the experimental results from the P&O testing is discussed. First, the speed of the algorithm is analyzed. As previously indicated, the converter was turned off and then back on in order to record the performance of the tracking algorithm. The power generated by the solar panel versus time is presented in Figure 79 for various settings. Note that the data from some of these tests was shifted in time; hence, all of these plots appear to begin at the same time, 1.55 seconds in this case.
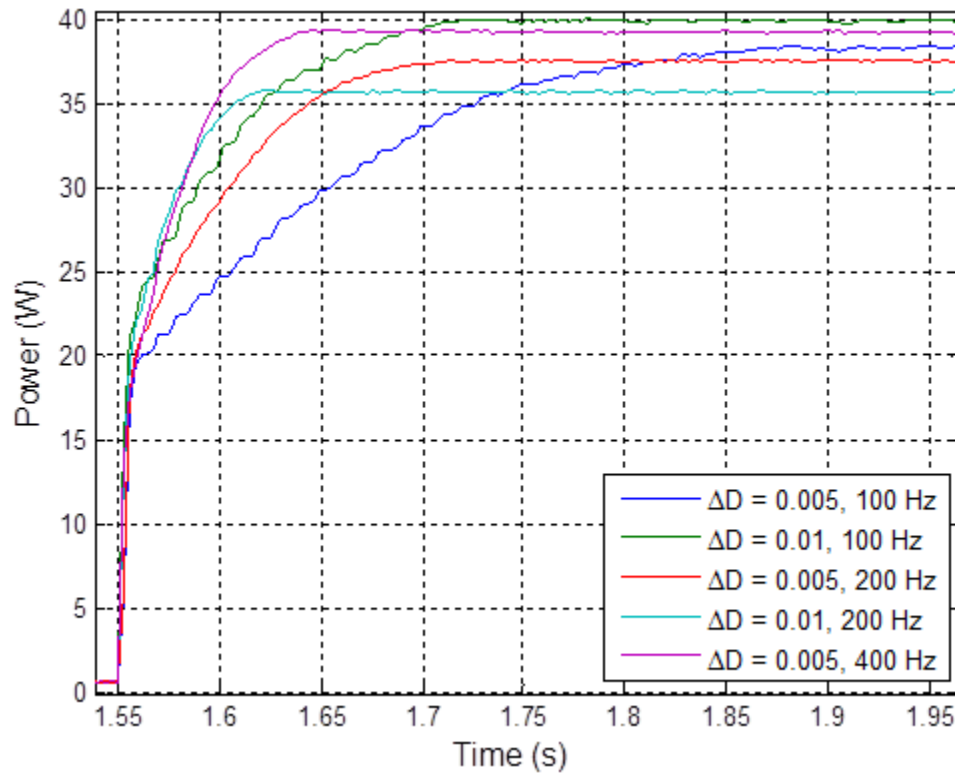

Figure 79.   Input power versus time for the P&O experiment using the IBC under various settings.

Just as in Chapter IV, the settling time was calculated for each of these plots. In Table 10, the settling time of the power response is summarized for various scenarios. While not exact, these results are similar to the results from simulation of the P&O

algorithm, which was discussed in Chapter IV. In fact, these results show that the actual system runs a little faster than the simulations predicted.

Table 10.   Settling time of the input power for the P&O experiment using the IBC under various settings.

Scenario	Settling Time (s)
$\Delta D = 0.005, f_{MPPT} = 100$ Hz	0.2736
$\Delta D = 0.01,\ \ f_{MPPT} = 100$ Hz	0.1396
$\Delta D = 0.005, f_{MPPT} = 200$ Hz	0.1251
$\Delta D = 0.01,\ \ f_{MPPT} = 200$ Hz	0.0576
$\Delta D = 0.005, f_{MPPT} = 400$ Hz	0.0768

Previously, in Chapter II, it was explained that changing certain control settings alters the performance of the algorithm. This speed test proves that these assertions are correct. For instance, as the MPPT frequency or the change in duty cycle increases, the algorithm drives the system to the MPP more quickly, and vice versa.

Another performance measure that was assessed is the accuracy of the MPP algorithm. One must ensure that the system actually reaches the MPP. To demonstrate this, the power versus voltage curve was created in Figure 80. Here, a thin black line depicts the theoretical power versus voltage curve. To produce this theoretical curve, the solar cell temperature was set to 43 °C, and the irradiance was adjusted to 1012 W/m^2. The timing of these measurements is broken up into four quarters just as in the Chapter IV. As one can observe, the system starts at the MPP. When the converter is turned off, the solar panel goes to the open-circuit voltage. When it is turned back on, the system recovers and then oscillates about the MPP until the end of the experiment; hence, P&O is functioning exactly as it is supposed to.
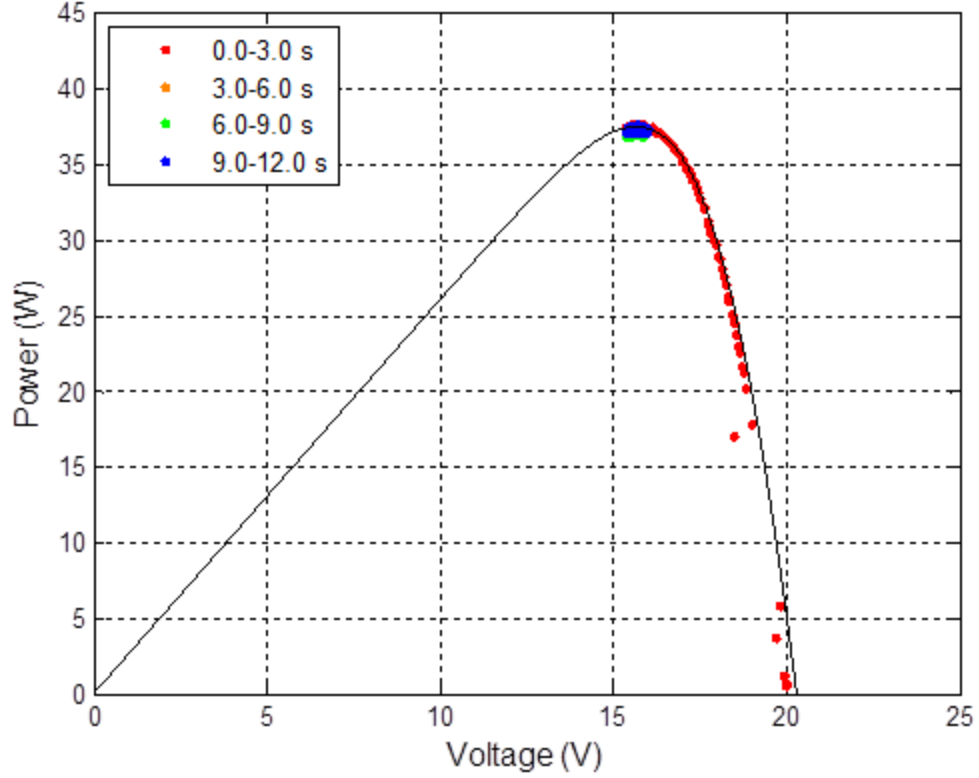
Figure 80.   Power versus voltage for the P&O experiment using the IBC where ΔD equals 0.005 and f_{MPPT} equals 200 Hz.

3.   Incremental Conductance Experimental Results

In this part of the thesis, the results from the test of the incremental conductance algorithm is shown and explained. As before, the speed of the algorithm is analyzed. In Figure 81, power versus time is graphed for the IC experiment when utilizing the IBC. The settling time associated with these plots is included in Table 11. Once more, these results paralleled the results from the simulation of the IC algorithm. Again, the actual system was slightly faster than the simulation. The P&O algorithm proved to be slightly faster than the IC algorithm but not by much; however, these results only depict a single sample for each scenario. To completely assess the performance, one should collect data from many more samples of the same test and then average the results.
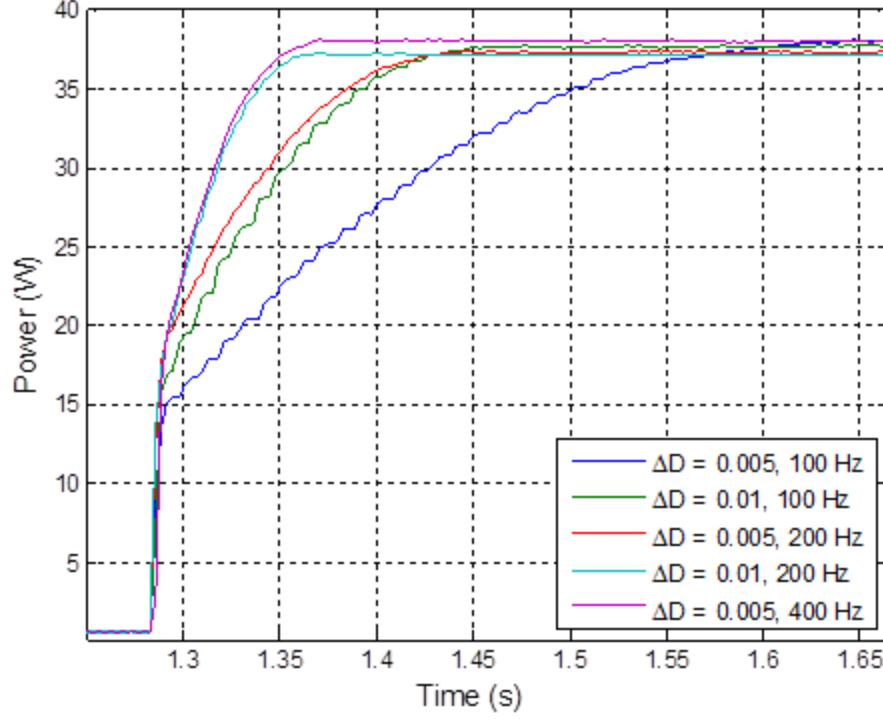
Figure 81.   Input power versus time for the IC experiment using the IBC under
various settings.

Table 11.   Settling time of the input power for the IC experiment using the IBC under
various settings.

Scenario	Settling Time (s)
$\Delta D = 0.005, f_{MPPT} = 100$ Hz	0.2975
$\Delta D = 0.01,\ \ f_{MPPT} = 100$ Hz	0.1417
$\Delta D = 0.005, f_{MPPT} = 200$ Hz	0.1294
$\Delta D = 0.01,\ \ f_{MPPT} = 200$ Hz	0.0670
$\Delta D = 0.005, f_{MPPT} = 400$ Hz	0.0697

Next, it had to be shown that the incremental conductance algorithm was able to operate at the MPP. As before, the power versus voltage data was plotted in Figure 82 in order to evaluate whether this algorithm could successfully find the MPP. Again, a simulated power versus voltage curve was overlaid on the plot of the actual experimental data. This time, the solar cell temperature was set to 43 °C and the irradiance was adjusted to 1009 W/m^2 to create this curve. In Figure 82, one observes that the IC algorithm performs very similar to the P&O algorithm. The difference is that the IC algorithm attempts to stop at the MPP voltage and remain there, as was seen in the

simulation results. In Figure 82, the data showed several changes about the MPP. This was because the environmental conditions during this particular test caused the algorithm to update itself every few seconds. If one looks at just the first three seconds of this experiment, one can see where the algorithm first locks onto the MPP. In Figure 83, the plot, which is a zoomed-in version of the power versus voltage curve from Figure 82, was adjusted to show that. Here, only the first three seconds are displayed as well as the initial lock-on point, which is plotted as a black dot. Clearly, one can see that the IC algorithm locks onto the MPP.
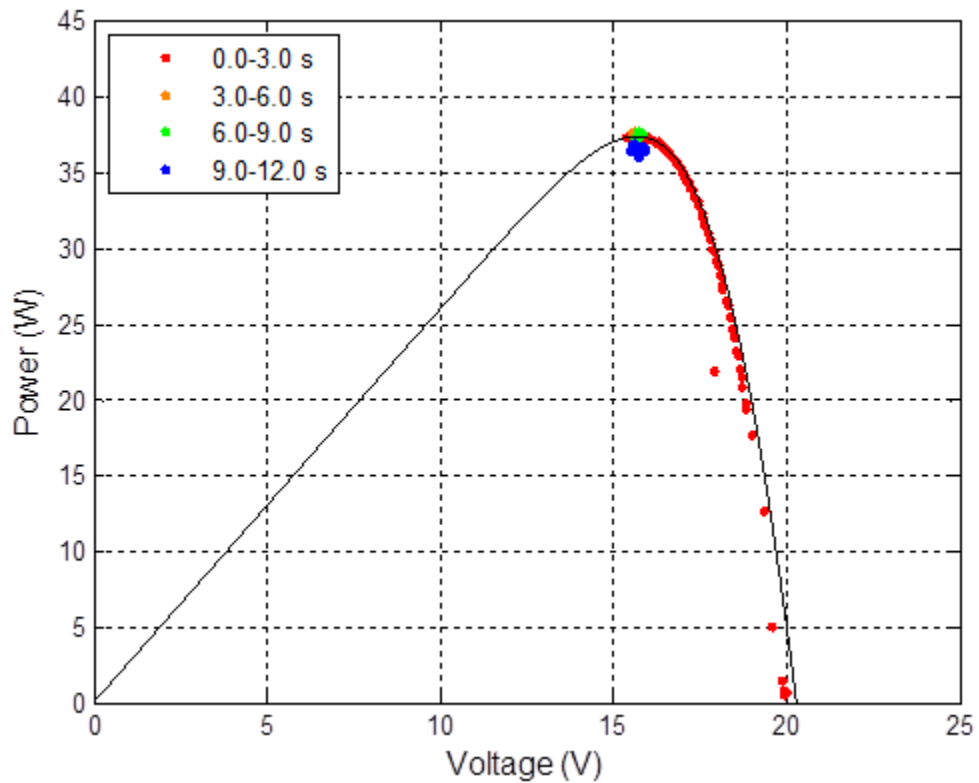
Figure 82.   Power versus voltage for the IC experiment using the IBC where ΔD equals 0.005 and f_{MPPT} equals 200 Hz.
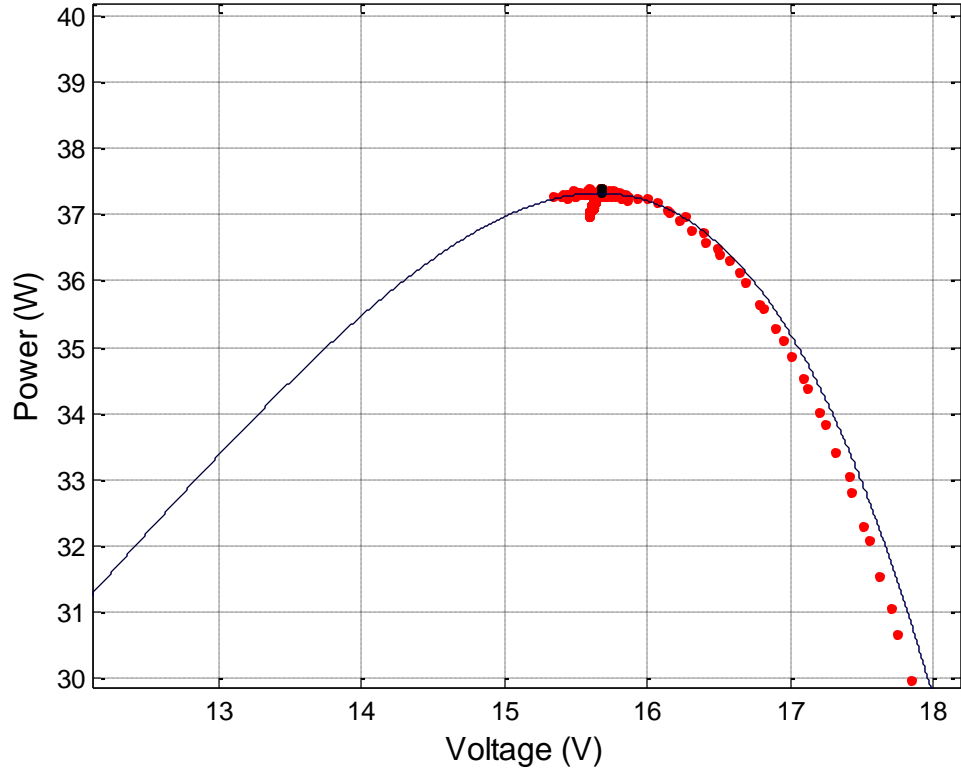
Figure 83.   Zoomed-in version of the power versus voltage for the IC
experiment using the IBC where ΔD equals 0.005 and f_{MPPT} equals
200 Hz (only 1st three seconds).

In order to better understand how the IC algorithm adjusted to the environmental conditions in this experiment, two other plots are offered. The duty cycle versus time plot in Figure 84 and the voltage versus time plot in Figure 85 were graphed to show what is taking place. As one can recognize, the duty cycle changes every few seconds due to a slight change in environmental conditions. Accordingly, the voltage changes in response to the change in duty cycle. After each adjustment, the algorithm determines a duty cycle in order to remain at the MPP or at least very close to the MPP. While this test shows a lot of variation in the operating point when using the IC algorithm, other tests show slightly different results. For instance, some of the tests locked onto a specific point and stayed there for the remainder of the experiment. In any event, these tests demonstrated that the IC algorithm operated as expected.
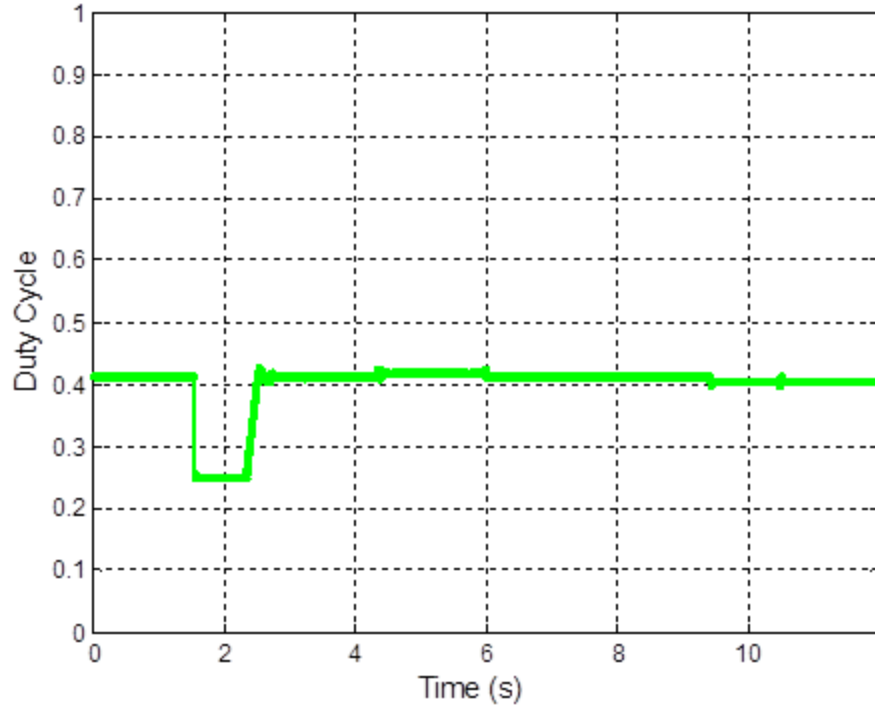
Figure 84. Duty cycle versus time for the IC experiment using the IBC where ΔD equals 0.005 and f_{MPPT} equals 200 Hz.
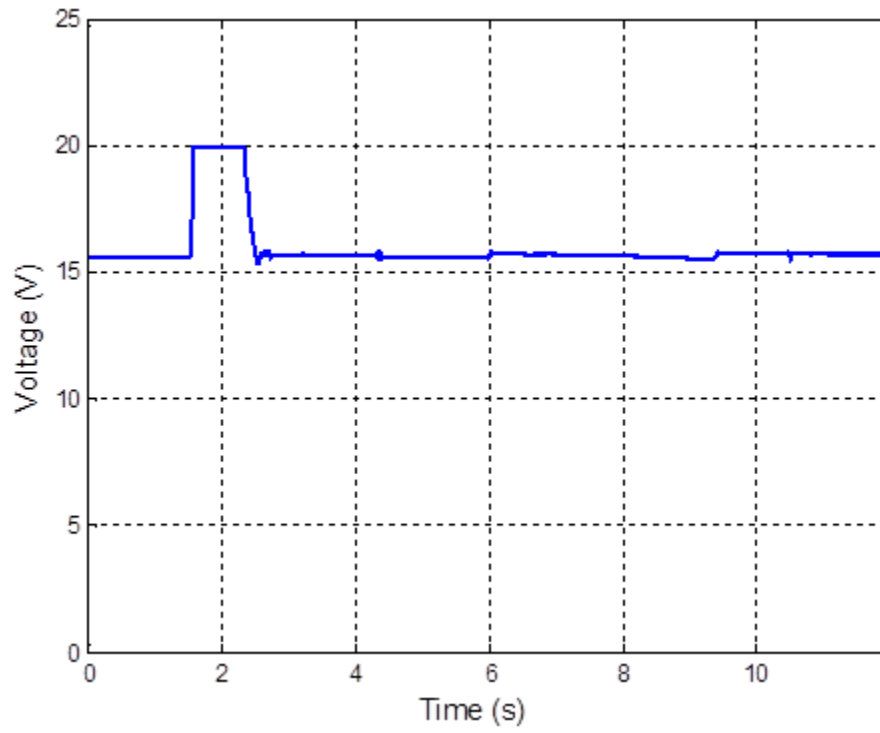
Figure 85. Voltage versus time for the IC experiment using the IBC where ΔD equals 0.005 and f_{MPPT} equals 200 Hz.

111

As a final note, the author could have included at least twenty different plots for various settings and conditions. These plots look similar to the plots in this section; thus, in the interest of conciseness, the number of plots was limited. Of note, even as the control settings were changed, the algorithms performed satisfactorily so that the system acquired the MPP.

4.   Other Experimental Results

The ripple of the interleaved boost converter is another item that was explored in this thesis. First, it must be noted that in Figures 86 and 87, the oscilloscope settings were used to average the samples in order to produce a finer plot. In Figure 86, an image of the oscilloscope shows the inductor current ripple when the duty cycle is 40%.
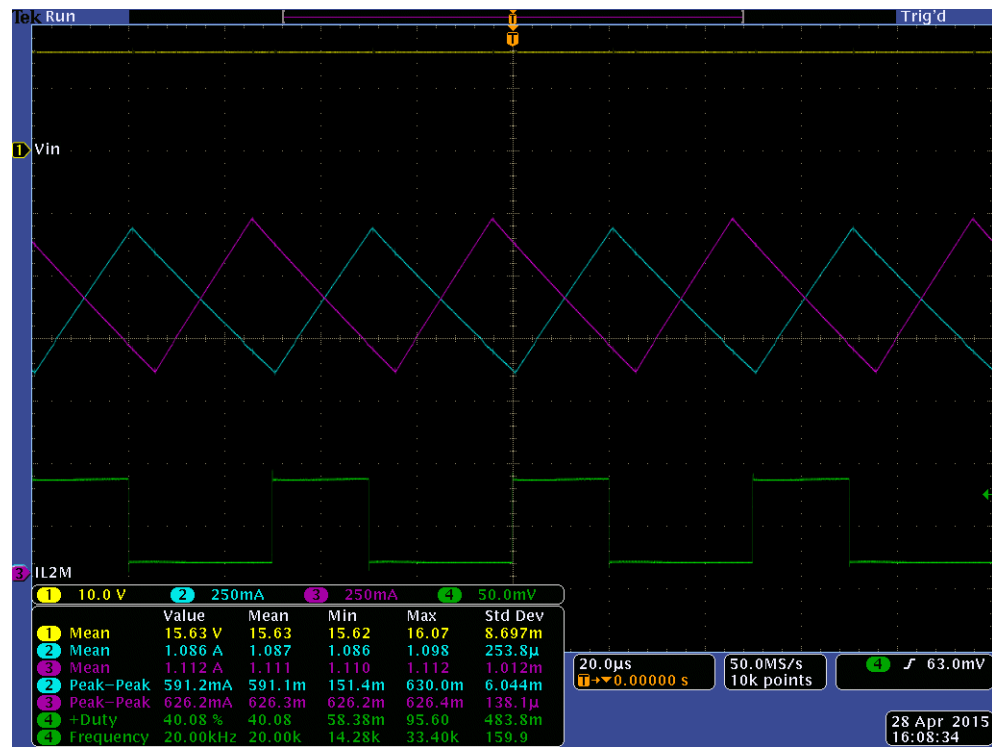
Figure 86.   Inductor current ripple using the IBC where the duty cycle is 40%.

There are a few things to note from this image. First, one can see that the inductor currents are interleaved just as designed, and they bear a striking resemblance to Figure 22, which was created with the simulation. Also, the inductor current ripple Δi_L, which is

112

the peak-to-peak current of the inductor, is around 600 mA. An approximation for this value can be predicted by doing theoretical calculations just as in Chapter II. In fact, this approximation turns out to be very close at 574.5 mA. Also, the simulation, which calculated the ripple to be 596 mA, can be used to verify this result.

In Figure 87, one sees the ripple in the total inductor current waveform. The total inductor current is the sum of the inductor current from each phase. Interestingly, this ripple happens to be about 1/3 of the ripple from a single phase in this scenario. As explained previously, this is due to the cancellation that occurs from the interleaved phases as the duty cycle approaches 50%. This image looks a lot like Figure 30, which shows the ripple in the total inductor current but was created via simulation.
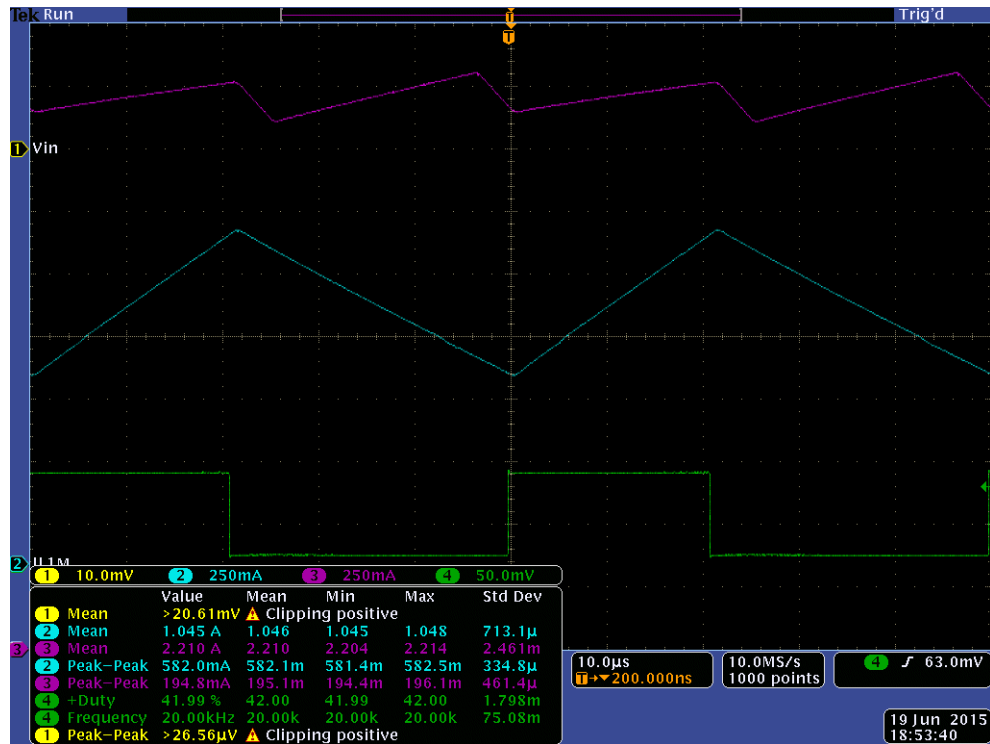
Figure 87.   Total inductor current ripple using the IBC where the duty cycle is 42%.

Next, the output voltage ripple is discussed. In this research, the evaluation of the output voltage ripple was extremely difficult due to measurement noise as well as the effects of switching, and there is certain level of uncertainty that is associated with these

113

measurements. Nevertheless, the following is presented in order to provide some insight into the benefits of the IBC. In Figure 88, the output voltage ripple for the IBC was assessed to be about 4 mV. Furthermore, in Figure 89, the output voltage ripple was determined to be around 21 mV using a regular boost converter. Thus, the output voltage ripple from the IBC was significantly less than for the regular boost converter. It must be noted that this disparity was dependent upon the fact that the IBC had a duty cycle that was fairly close to 50%. The amount of output current had a significant effect on the output voltage ripple as well. As a final point, these numbers for the output voltage ripple were comparable to those seen in the simulations.
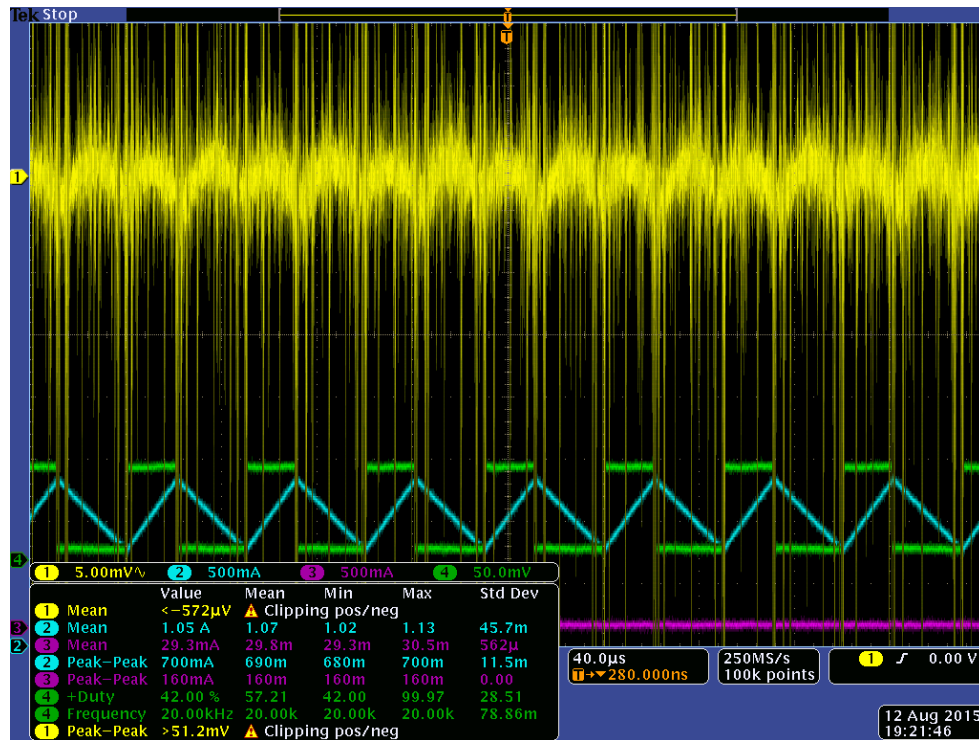
Figure 88.   Output voltage ripple using the IBC where the duty cycle is 42%.

The efficiency of the actual converter was explored in this thesis as well. Unfortunately, during the testing of the P&O algorithm, it was fairly difficult to measure the exact voltages and currents as they varied. Thus, the P&O efficiency results were deemed less reliable than the IC efficiency results. While these results were interesting, the reader should not draw any conclusions by comparing the two algorithms with each

other. For the P&O algorithm, the regular boost converter and the IBC achieved an average efficiency of 87.40% and 89.35%, respectively. The IC efficiency results were much more accurate since the algorithm locked on to a specific voltage and current for a period of time. This made it easier to record the correct values. The regular boost converter experienced an average efficiency of 86.58%, while the interleaved boost converter had an average efficiency of 88.61%. As predicted, the IBC operated with an efficiency about 2% greater than that of the regular boost converter.
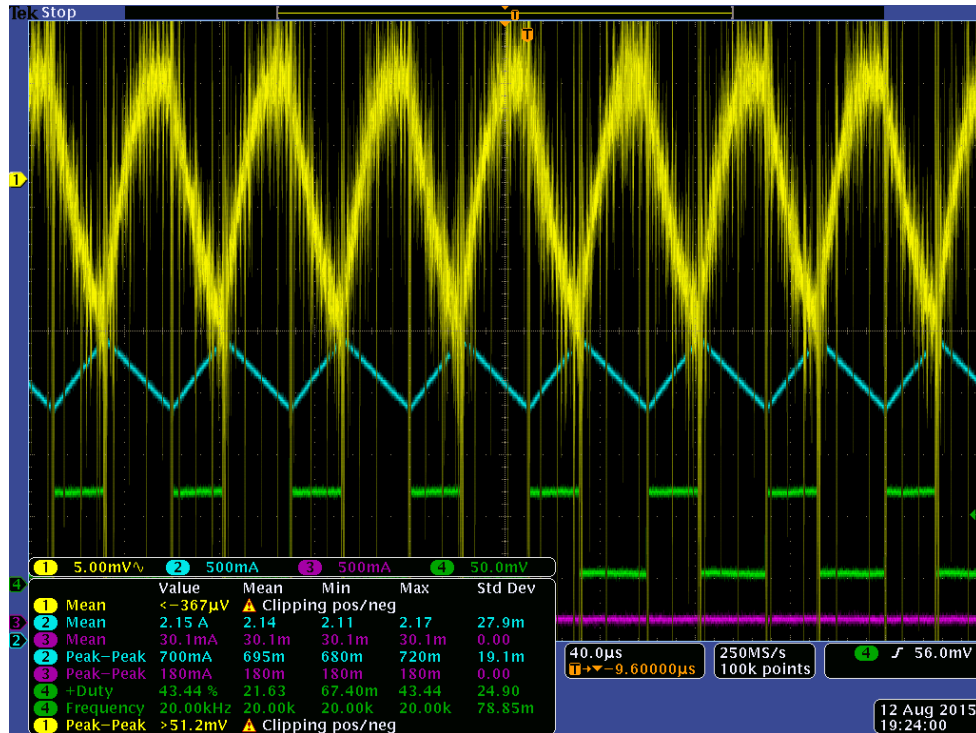
Figure 89.   Output voltage ripple using the regular boost converter where the duty cycle is about 43.5%.

Finally, the effects of shading were explored. In Figure 90, one can see how the system using the P&O algorithm reacts when the solar panel is partially shaded. A few observations can be noted here. For one, the algorithm finds a new MPP with a higher voltage. Also, only a small fraction of the panel was shaded, but the available power was decreased by over a factor of five. The photo-generated current was significantly reduced due to the shading. With all of the solar cells placed in series with one another, this

115

seriously limits the power produced by the panel. Furthermore, once the shading is removed, the system returns very quickly to its original MPP. Of note, in order to make the theoretical power versus voltage curve, the solar cell's temperature and irradiance were adjusted to 40 °C and 1020 W/m^2, respectively. Additionally, the IC algorithm behaved similarly under shading conditions except that it attempted to lock onto the new MPP setting as designed.
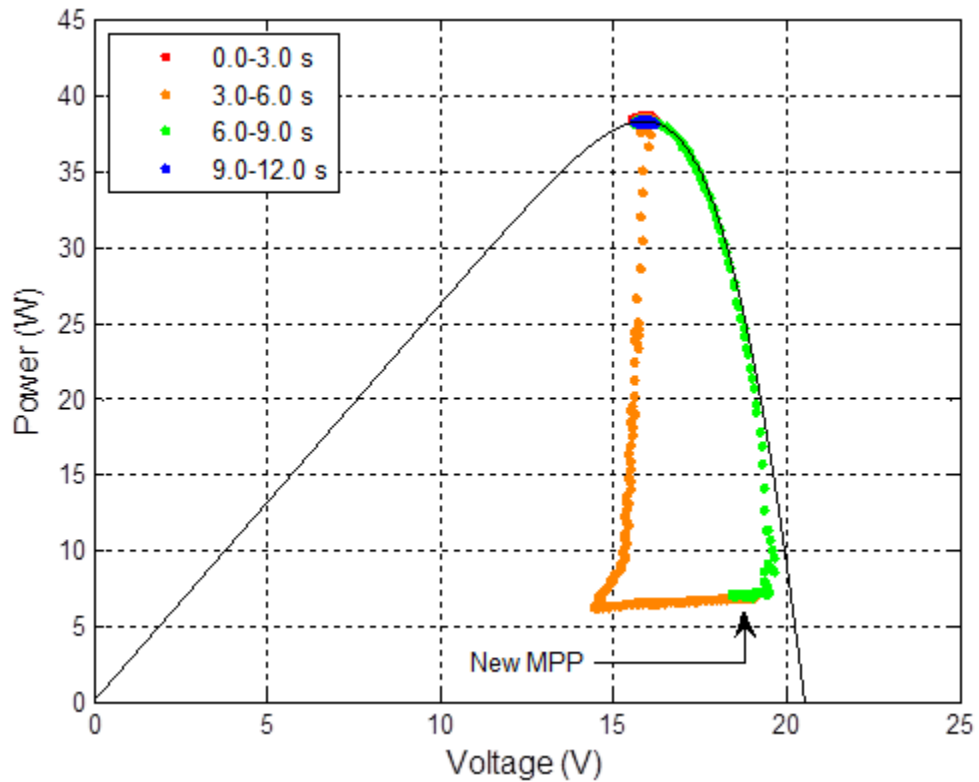
Figure 90.   Power versus voltage for the P&O shading experiment using the IBC where ΔD equals 0.005 and f_{MPPT} equals 200 Hz.

VI.   CONCLUSIONS AND RECOMMENDATIONS

Some conclusions that were deduced from this research as well as some recommendations for future work on this topic are offered in this chapter, which is not intended to be all-inclusive. In fact, many of the recommendations and findings have already been shared throughout this thesis.

A.   CONCLUSIONS

In conclusion, this research was successful. The author was able to explore the many facets of maximum power point tracking as well as the interleaved boost converter. Also, two successful algorithms were designed and tested using the Xilinx FPGA hardware and software. The main outcomes of this research and the associated lessons learned are described in the following.

1.   Benefits of Maximum Power Point Tracking

The main benefit of using a MPPT algorithm is that it allows the system to extract the most power from panel vice some fraction of that. As suggested previously, without the MPPT, the solar panel is not necessarily able to operate at its maximum power point. This is unfortunate since a great deal of available power is potentially lost. The benefits of tracking the MPP for each panel versus employing a centralized controller were also explained. It was shown that connecting a converter to each panel yields more overall power than using a system that tracks the MPP of an assembly of solar panels.

2.   Benefits of using an Interleaved Boost Converter

In this thesis, the IBC was shown to offer some key benefits. For one, it operates with greater efficiency than a regular boost converter. Additionally, the IBC produces a lower ripple since the inductor currents have a tendency to cancel each other. Because the IBC has more power electronic components, it likely costs more than a regular boost converter. Furthermore, it is more complicated to control and operate when compared to a regular boost converter.

117

3. Best MPPT Algorithm

While it would be preferred to rule that one algorithm was better than the other, this is difficult to do. Both of the algorithms have advantages and disadvantages. For instance, perturb and observe is a better algorithm if a simple, reliable MPPT program is desired; however, P&O does not stabilize perfectly at the MPP but fluctuates about the MPP. On the other hand, incremental conductance is best if one wishes to lock onto to a specific setting, which allows the system to operate more steadily at the MPP. This method induces almost no fluctuations in the voltage and current once it is stable at the MPP. The IC algorithm is more complicated, so it is likely more costly to program and implement. Additionally, as seen in this research, it was possible for the IC algorithm to lock onto the wrong point, in which case the system does not extract the maximum power from the solar panels.

4. Best Parameters for the Algorithm

When these algorithms are implemented on a digital platform, the MPPT rate and the step-size for the change in duty cycle (or reference voltage) are critical parameters. As the MPPT rate increases, the algorithm should be able to track the MPPT more quickly under changing conditions. It must be noted that doing this may require increased measurement resolution, or it may not be able to correctly find the MPP. Likewise, increasing the step-size reduces the tracking time, but increased measurement resolution may be needed. Furthermore, a large step-size can cause large fluctuations around the MPP; thus, it is desirable to reduce the step-size to an acceptable level so that the fluctuations in voltage and current are tolerable.

In this thesis, the best combination of settings was a MPPT frequency of 200 Hz and a step-size for the duty cycle of 0.005. This gave the best mixture of speed and stability in the steady-state. One can increase ΔD to get more speed, but this has a slight drawback. For instance, as the change in duty cycle was increased to 0.01 while f_{MPPT} remained at 200 Hz, the amount of perturbation also increased. When using the P&O algorithm, this causes the system to vary about the MPP a little more. When using IC, the algorithm sometimes fluctuated very briefly until it found an appropriate setting to lock

118

on to the MPP. When f_{MPPT} was increased to 400 Hz while keeping ΔD at 0.005, the algorithm made its decision before the dynamics of the system had settled. One must realize that the dynamics of the system only apply to this particular converter with its specific components. For a different converter, a frequency of 400 Hz may not have this issue. As a final point, the speed was cut in half when the frequency was decreased to 100 Hz.

5.   Implementation Difficulty

The difficulty of implementation was another key takeaway from this research. While developing a simulation is challenging enough, the real problem is in applying the theory to an actual physical system. For instance, the power board was originally meant to function as an inverter, so it had to be altered in order to work as an IBC. This involved removing a capacitor and modifying the circuit that sent the logic signals to the gate drivers. Once that was done, the sensors had to be calibrated so that they gave reasonable information. The issue of noise also had to be mitigated; thus, a digital filter was employed. It took many simulations to see what cutoff frequency worked best. Last but not least, the control parameters for the algorithms had to be fine-tuned so that the algorithm functioned as desired. This involved countless simulations and tests to find the best settings.

B.   RECOMMENDATIONS

Several recommendations for future work are contained in the following section. Some of these recommendations expand upon the present research while some could possibly develop into an entirely new research topic.

1.   Create a Faster and More Accurate Simulation

The Simulink simulations took an excessively long time. For instance, the simulation of the incremental conductance algorithm in Simulink took to 10.5 hours to run just a 0.7 second simulation when using a 40 ns numerical step-size. Even when the numerical step-size was increased to 250 ns, the incremental conductance simulation still took about 1.5 hours. If the simulation was forced to run much faster, then accuracy was

sacrificed.; hence, it is desired to find a way to increase the speed of the simulation while maintaining its accuracy. Also, while the modeling of the solar panel's characteristics was very good, it was not perfect. As one can see in Figures 80 and 82, the open-circuit voltage did not perfectly match the real data. Perfecting the model of the solar panel would be beneficial.

2.   Optimize the Hardware

Due to the time constraints while developing this thesis, the author did not have the time to build the hardware that was used in this research. Instead, a previously used inverter was modified in order to create the interleaved boost converter, and there are many items that could have been better optimized for performance. For instance, the capacitors and inductors were too large. While this helped control the ripple, these sizes would not be practical in a commercial product. Also, reducing the size of these components would minimize the conduction losses associated with these items. Furthermore, the analog-to-digital converter that was used was a 12-bit device. While this was adequate, it would have been better too use an ADC that had better resolution in order to achieve voltage and current measurements that were more accurate. In addition, the IGBTs were too large and had too high of a voltage rating. A smaller device would have made the system more efficient. For instance, using a power metal-oxide semiconductor field-effect transistor (MOSFET) may have been a better choice instead of IGBTs since the voltage and currents involved were small. Also, using MOSFETs would have allowed for a higher switching frequency than using IGBTs [17]. Along the same lines, the selection of a diode with lower on-state voltage drop would have helped improve efficiency as well. The highest voltage that these components are required to block is about 50 V; thus, selecting a smaller diode as well as a smaller transistor would have been entirely reasonable.

3.   Explore Other Algorithms and Scenarios

There were many maximum power point tracking algorithms presented in this thesis. For future work, one could explore one of these other MPPT algorithms with an interleaved boost converter. Furthermore, one could test other scenarios such as multiple

solar panels connected in parallel and/or series. During the testing phase of this research, the sun was used as the sole source of solar energy. If one could obtain a solar power simulator or a light source that could be controlled, then one could conduct scenarios where the solar irradiance is varied precisely. Lastly, one could explore the DCM characteristics of the IBC in detail.

4.   Construct a Resonant IBC

Switching losses were a significant portion of the reduced efficiency seen in the interleaved boost converter. Developing an IBC that attempts to avoid some or all of these losses through resonance is a worthwhile task. One could base such a proposal off the existing designs that incorporate resonant switching into a regular boost converter. With that, one could add an additional phase and ensure that the gating signals were interleaved. Alternatively, one could develop another topology that employed resonant principles but also utilized the interleaving effect.

5.   Integrate a Charge Controller

The main focus of this research was to do maximum power point tracking in order to power a resistive load and a battery. Another thesis topic is to develop a charge controller for the battery. This controller would integrate with the MPPT algorithm and the IBC. In this case, the layout of the system would be almost identical except that there would be some extra switches that would be in series with the battery and the load. There would be some additional logic involved in order to decide whether the battery, the load, or both would be powered according to the charge controller's settings.

THIS PAGE INTENTIONALLY LEFT BLANK

APPENDIX A. MATLAB CODE

```matlab
%% Solar model parameters

close all

sim=1;
if sim==1
    tstep=3.125*40e-9; % sets the time step for the clock
    ADC_count=round(180/3.125); % specifies the number of clock cycles
for the ADC sample period
    ADC_sample=ADC_count*tstep; % sets the ADC sample period
    ADC_freq=1/ADC_sample;  % finds the ADC sample frequency
    f_clock=1/tstep; % sets the clock frequency
    Dcmtn_plot=16; % specifies the decimation for plotting
else
    tstep=40e-9; % sets the time step for the clock
    ADC_count=180; % specifies the number of clock cycles for the ADC
sample period
    ADC_sample=ADC_count*tstep; % sets the ADC sample period
    ADC_freq=1/ADC_sample;  % finds the ADC sample frequency
    f_clock=1/tstep; % sets the clock frequency
    Dcmtn_plot=16*3.125; % specifies the decimation for plotting
end


% Analog-to-Digital Conversion parameter

f_cut_V=100; % sets the voltage cutoff frequency for the digital filter
in Hz
f_cut_I=100; % sets the current cutoff frequency for the digital filter
in Hz


pre_gain_V=2*pi*f_cut_V*tstep; % calculates the pre-gain of the digital
filter for the voltage signal
pre_gain_I=2*pi*f_cut_I*tstep; % calculates the pre-gain of the digital
filter for the current signal

feedback_gain_V=1-2*pi*f_cut_V*tstep; % calculates the feedback gain of
the digital filter for the voltage signal
feedback_gain_I=1-2*pi*f_cut_I*tstep; % calculates the feedback gain of
the digital filter for the current signal

F_mat=[0 0 0 1;1 1 2 0;2 2 3 0;3 3 0 0]; % sets up the F matrix to be
used in the Mealy State Machine used for analog-to-digital conversion
O_mat=F_mat;% sets up the O matrix to be used in the Mealy State
Machine used for analog-to-digital conversion

V_offset=-0.168; % adds an offset to the measured input voltage
I_offset=0.016; % adds an offset to the measured input current
V_out_offset=0.0; % adds an offset to the measured output voltage
```

```matlab
V_scaling=0.9913; % multiplies a scaling factor to the measured input
voltage
I_scaling=1.0384; % multiplies a scaling factor to the measured input
current

V_noise_SD=0.05; % sets the standard deviation for the voltage noise
I_noise_SD_high=0.06; % sets the standard deviation for the current
noise when the current is high
I_noise_SD_low=0.01; % sets the standard deviation for the current
noise when the current is low

high_to_low=0.22; % specifies when the irradiance transitions from high
to low
low_to_high=0.4; % specifies when the irradiance transitions from low
to high

gain2out=1/(1/6800+1/200000)/(1/(1/6800+1/200000)+120000*2); % output
voltage sensor gain
gain2=1/(1/100000+1/200000)/(1/(1/100000+1/200000)+120000*2);  % input
voltage sensor gain
gainI220=(3/1000*220); % current sensor gain

%Constants

k=1.3806488e-23;   % Boltzmann Constant
q=1.602176565e-19; % electron charge
Temp_ref=25; % Reference temperature of the solar cells in Celsius
Kelvin=273.15; % Temperature in Kelvin at 0 deg Celsius
Dcmtn=1000; % specifies the decimation for displaying values

% Solar array parameters

Temp=50; % Actual temperature of the solar cells in Celsius
S=1000; % solar insolation in W/m^2
theta=0.0*(pi/180); % angle of incidence
S_rate=10000; % max rate at which the solar irradiance is allowed to
change in W/m^2 per second
change_in_S=S*.8; % defines the change in S for the simulation
K_i=0.0017; % amps per temperature (A/degrees) - "MATLAB/Simulink Based
Modelling of Solar Photovoltaic Cell" by Salmi et al.
Eg=1.11; % bandgap energy of silicon in eV
cell_area=(4+7/8)*(2+7/16)*(2.54)^2; % cell area in cm^2
Jsc=0.0331325; % short circuit surface current density in A/cm^2
Isc=Jsc*cell_area; % short circuit current of the solar cell at a solar
irradiance of 1000 W/m^2 and a temperature of 25 degrees C
Rsh=1000; % Shunt resistance for solar cell model
Rs=0.01717; % Series resistance for solar cell model
Is_ref=3.12e-8; % reverse saturation current at 25 degrees C
Is2_ref=0; % Set to zero for 1-diode model; otherwise, set as
appropriate for 2-diode model
N1=1.282; % Ideality factor
N2=1.2; % Used only in the 2-diode model
Cell_series=36; % number of cells in series per module
Cell_parallel=1; % number of cells in parallel per module
```

```matlab
Module_series=1; % number of modules in series per array
Module_parallel=1; % number of modules in parallel per array

% Converter parameters

fs=20e3;  % switching frequency of the switches
Cpv=650e-6; % Capacitance of the PV capacitor
Vin_IC=19.77; % Initial input voltage for the PV capacitor
L=470e-6; % Inductance of the inductor
RL=0.25; % Resistance of the inductor
C=990e-6; % Capacitance of the output capacitor
Vout_IC=23.77; % Initial output voltage for the output capacitor
f_cut=1/(2*pi*sqrt(L*C)); % Cutoff frequency in Hz
R_diode=0.15; % sets the diode resistance
R_IGBT=0.15; % sets the IGBT resistance
Vf_diode=0.6; % sets the diode forward voltage drop
Vf_IGBT=1.2; % sets the IGBT forward voltage drop

Cs_MOSFET=1e-15; % sets snubber parameters so that there is effectively
no snubber in the simulated circuit
Rs_MOSFET=1e15;
Cs_IGBT=1e-15;
Rs_IGBT=1e15;
Cs_diode=1e-15;
Rs_diode=1e15;

% Load parameters

Rload=18.23;  % specifies the load resistance
Lload=0;  % specifies the load inductance
Rbatt=0.175; % source resistance (substitute for the battery)
Vbatt=24; % specifies the battery voltage

% Duty cycle parameters

MnPrd=1/fs; % specifies the mean period for averaging certain signals
D_IC=0.25; % specifies the initial condition for the duty cycle
D_lower=0.05; % specifies lowest allowable duty cycle
D_upper=0.95; % specifies highest allowable duty cycle
number_of_interleave=2; % specifies the number of interleaved parallel
branches
interleave_delay=round(((1/fs)/number_of_interleave)/tstep); %
determines the interleaved delay in number of clocks

% MPPT control paramters

T_sample=1/200; % sampling period of the MPPT in seconds
MPPT_delay=round(T_sample/tstep); % number of clock cycles associated
with the Delay for MPPT
delta_D=0.005; % step-size for change in duty cycle
IC_limit=0.012; % sets the limit for abs(dI/dV+I/V) to be considered 0
IC_limit_dV=0.007; % sets the limit for abs(dV) to be considered 0
IC_limit_dI=0.006; % sets the limit for abs(dI) to be considered 0
```

```matlab
% Xilinx parameters

bits=23; % specifies the number of bit to be used for fixed point
numbers
bp=17;  % specifies the binary point location for fixed point numbers
step_bits=34; % specifies the number of bit to be used to represent the
step size for fixed point numbers
accum_bits=59; % specifies the number of bit to be used in the
accumulator for fixed point numbers
const_bits=21; % % specifies the number of bit to be used to express
certain constants
bits1=bp+1; % specifies the number of bit to be used as bp+1
bits2=bp+2; % specifies the number of bit to be used as bp+2
bits3=bp+3; % specifies the number of bit to be used as bp+3
bits4=bp+4; % specifies the number of bit to be used as bp+4
MPPT_bits=22; % defines the number of bit to use for the MPPT counter
PWM_bits=12; % defines the number of bit used to count for the PWM
signal
ADC_count_bits=8; % specifies number of bits to use for the ADC counter
data_rate_count=round((12/2^12)/tstep); % specifies the number of clock
cycles for the data rate into Chipscope; do not make greater than 2^17
without adding more bits
data_rate_bits=17; % specifies number of bits to use for the data rate
counter
```

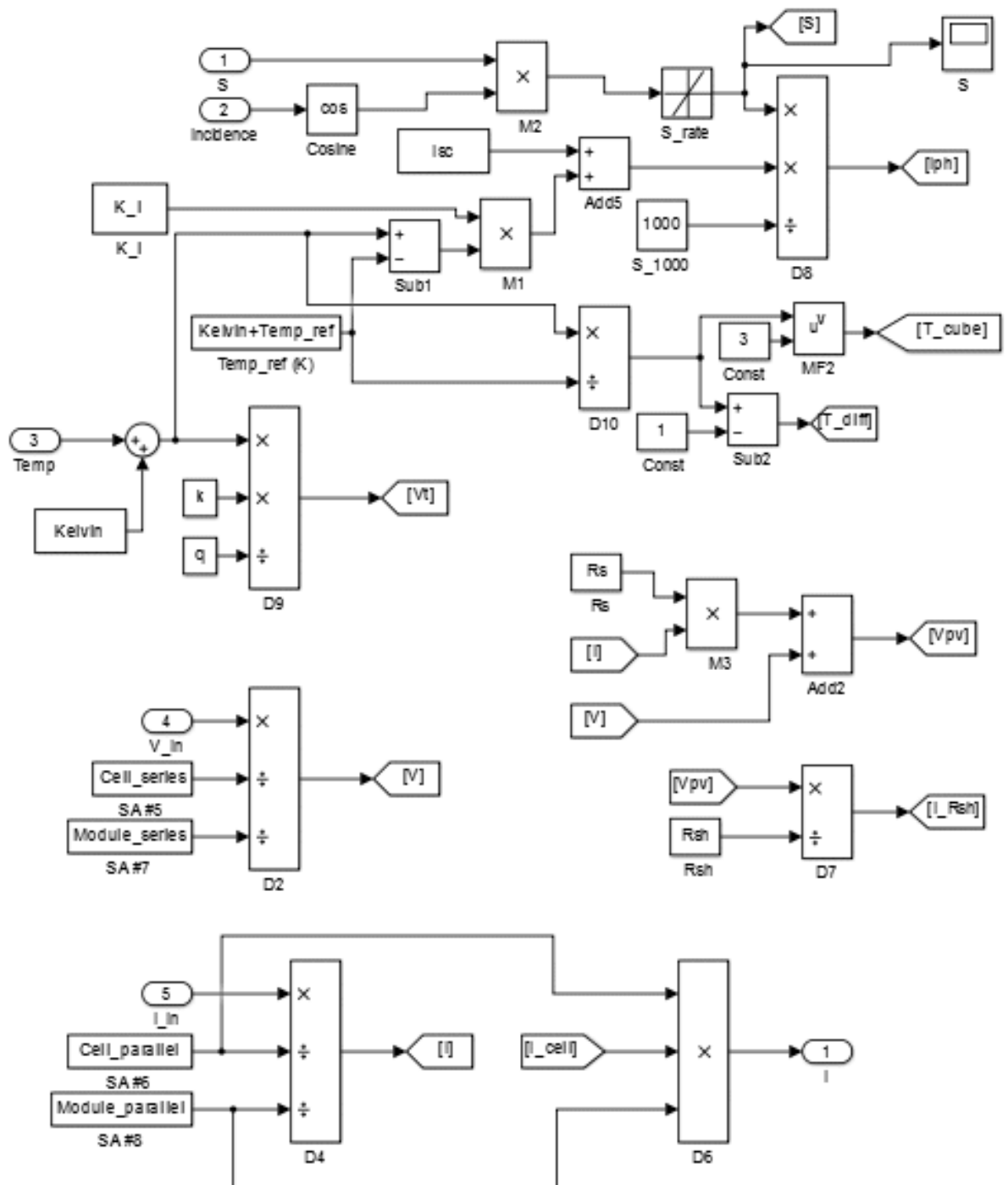# APPENDIX B. SIMULINK MODELS

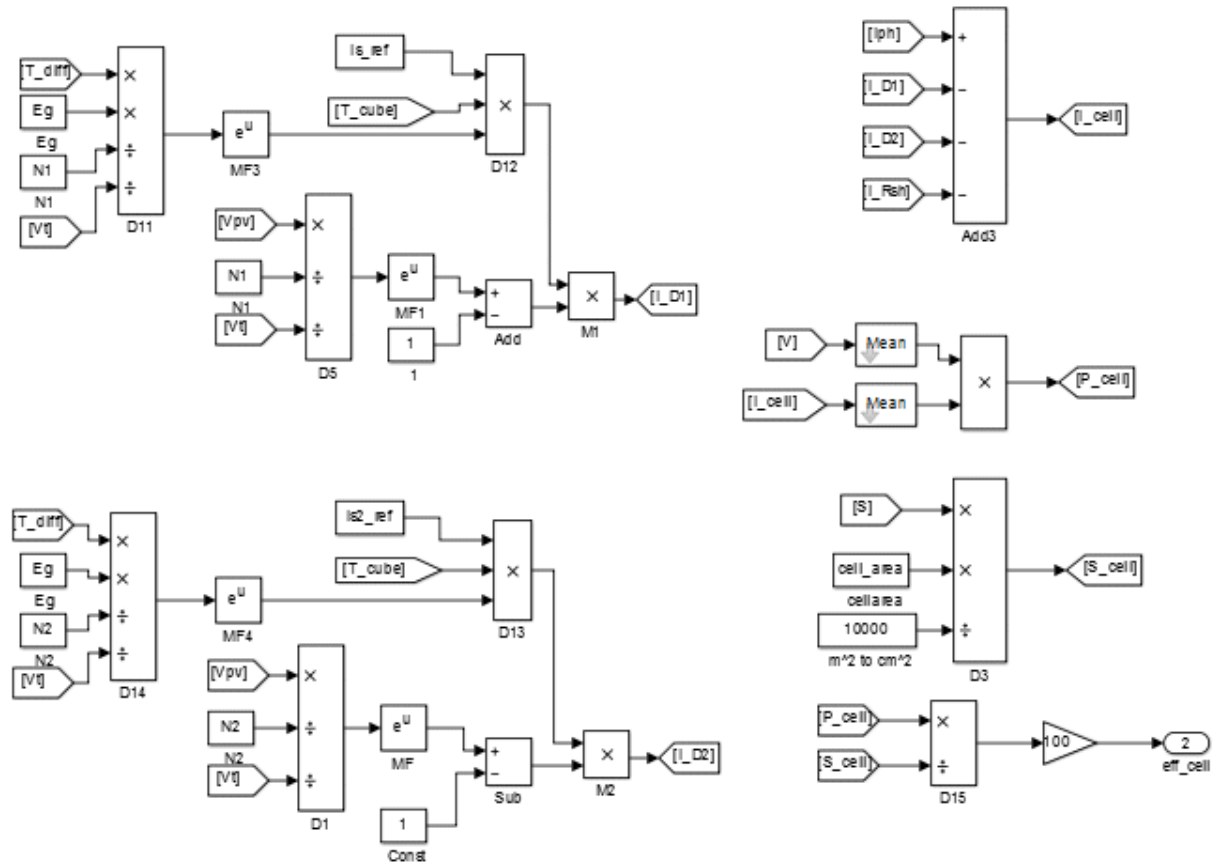Figure 91.   Solar cell model equations in Simulink (left side).

Figure 92.   Solar cell model equations in Simulink (right side).
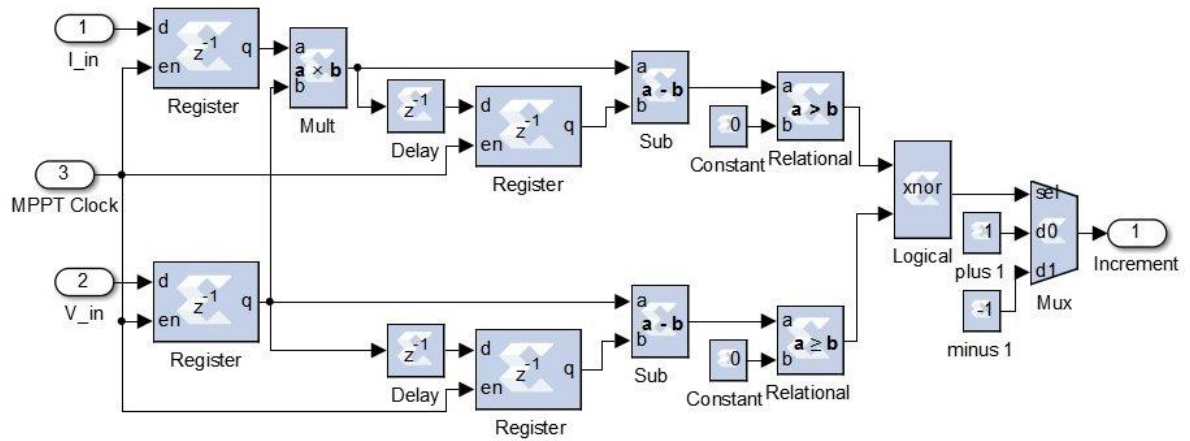

Figure 93.   Perturb and observe algorithm in Simulink using the Xilinx blockset.
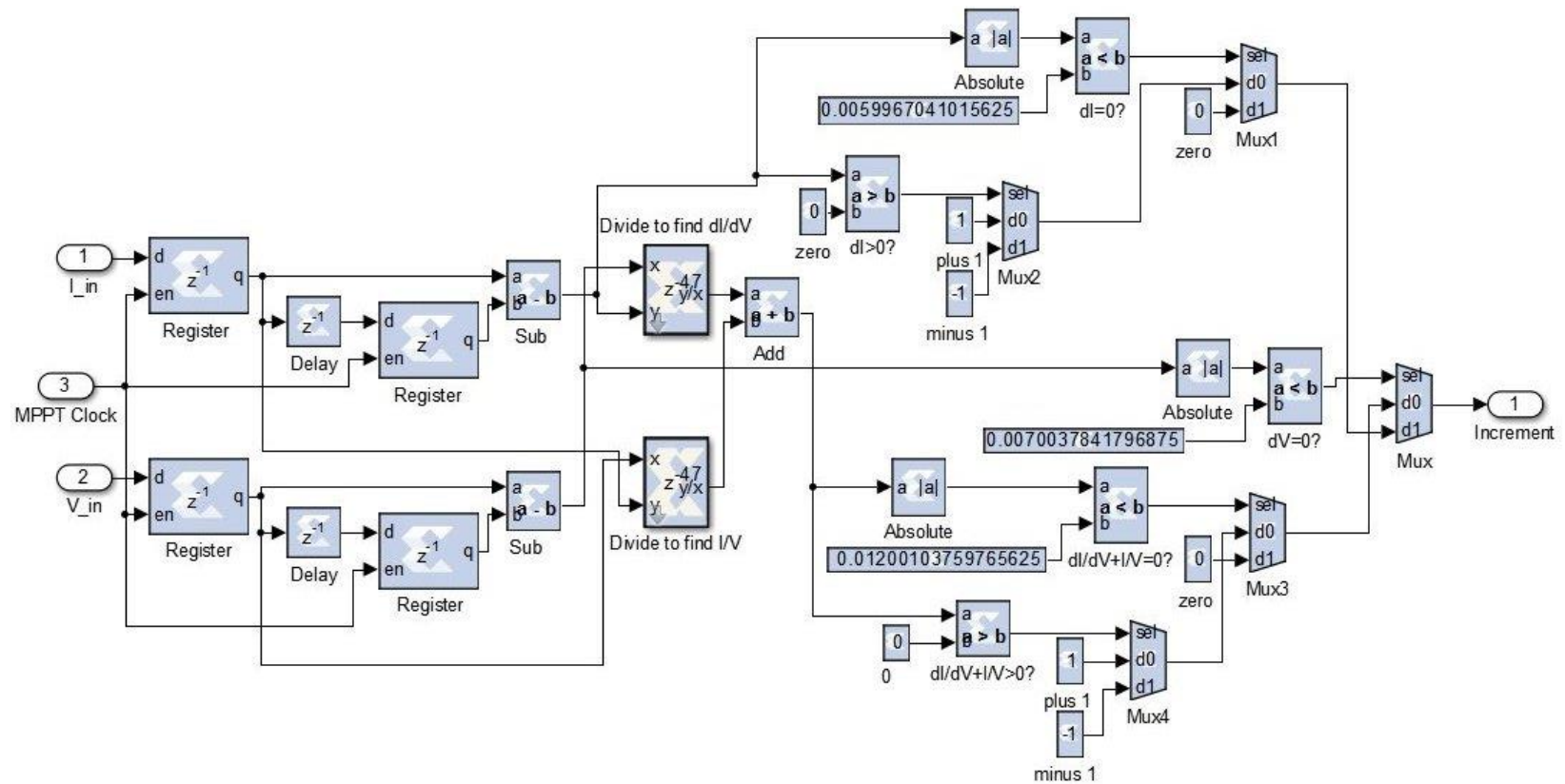
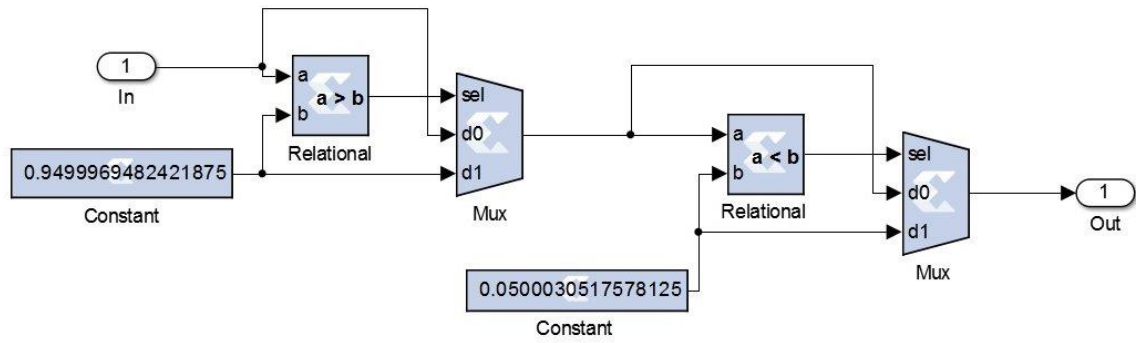Figure 94.   Incremental conductance algorithm in Simulink using the Xilinx blockset.

Figure 95.   Saturation limits in Simulink using the Xilinx blockset

LIST OF REFERENCES

[1]   *DOD Energy Policy*, DOD Directive 4810.01, Under Secretary of Defense (AT&L), Washington, DC, 2014, pp. 1.

[2]   *USMC Expeditionary Energy Strategy Implementation Planning Guidance*, Headquarters, United States Marine Corps (Expeditionary Energy Office), Washington, DC, 2011.

[3]   Ground Renewable Expeditionary Energy Network System (GREENS). (n.d.). UEC Electronics, LLC, Hanahan, SC. [Online]. Available: http://www.uec-electronics.com/pdfs/GREENS%20Product%20Brochure%209-11-2014.pdf. Accessed Jun. 20, 2015.

[4]   L. Jiang, "Resistance control MPPT for Smart Converter PV System," M.S. thesis, Dept. Elect. Comput. Eng., Virginia Polytechnic Institute and State University, Blacksburg, VA, 2012.

[5]   Marine Corps Expeditionary Energy Office. (n.d.). United States Marine Corps. [Online]. Available: http://www.hqmc.marines.mil/e2o/Fleet.aspx. Accessed Apr. 15, 2015.

[6]   A. S. Sedra and K. C. Smith, *Microelectronic Circuits*, 5th ed. New York, NY: Oxford University Press, Inc., 2004.

[7]   S. Michael, "Solar energy," class notes for EC3240 Renewable Energy at Military Bases and for the Warfighter, Dept. Elect. Comput. Eng., Naval Postgraduate School, Monterey, CA, summer 2014.

[8]   S. A. Kalogirou, *Solar Energy Engineering: Processes and Systems*, 1st ed. Burlington, MA: Academic Press, 2009.

[9]   D. Hettelsater, Y. Zhang, and A. Shakouri. (2002, May 9). Lab 7: solar cells. [Online]. Available: http://classes.soe.ucsc.edu/ee145/Spring02/EE145Lab7.pdf.

[10]   Photon. (n.d.). *Wikipedia*. [Online]. Available: http://en.wikipedia.org/wiki/Photon. Accessed May 27, 2015.

[11]   P. Gevorkian, *Large-Scale Solar Power System Design: An Engineering Guide for Grid-connected Solar Power Generation*, 1st ed. New York, NY: McGraw-Hill Education, 2011.

[12]   T. Salmi, M. Bouzguenda, A. Gastli, and A. Masmoudi, "MATLAB/Simulink based modelling of solar photovoltaic cell," *Int. J. of Renewable Energy Research*, vol. 2, no. 2, pp. 213–218, 2012.

[13]   S. Nema, R. K. Nema, and G. Agnihotri, "MATLAB/Simulink based study of photovoltaic cells / modules / array and their experimental verification," *Int. J. of Energy and Environment*, vol. 1, no. 3, pp. 487–500, 2010.

[14]   H. Tsai, C. Tu, and Y. Su, "Development of generalized photovoltaic model using MATLAB/SIMULINK," in *Proc. of the World Congr. on Eng. and Comput. Sci.*, San Francisco, CA, 2008, pp. 1–6.

[15]   Shanghai Raloss Energy Technology Co., Ltd. (2007, Sep.). *RLS-Datasheet-1*. Shanghai, China. [Online]. Available: http://www.farnell.com/datasheets/95510.pdf.

[16]   R. Ashton, "Popular direct-coupled dc-dc converters," class notes for EC3150 Solid State Power Conversion, Dept. Elect. Comput. Eng., Naval Postgraduate School, Monterey, CA, summer 2014.

[17]   N. Mohan, T. M. Undeland, and W. P. Robbins, *Power Electronics: Converters, Applications, and Design*, 3rd ed. Hoboken, NJ: John Wiley & Sons, Inc., 2003.

[18]   P. T. Krein, *Elements of Power Electronics*, 1st ed. New York, NY: Oxford University Press, Inc., 1997.

[19]   B. Hauke, "Basic calculation of a boost converter's power stage," Texas Instruments Inc., Dallas, TX, App. Rep. SLVA372C, Jan. 2014.

[20]   R. Crews, "AN-1820 LM5032 interleaved boost converter," Texas Instruments Inc., Dallas, TX, App. Rep. SNVA335A, May 2013.

[21]   H. M. Mallikarjuna Swamy, K. P. Guruswamy, and S. P. Singh, "Design, modeling and analysis of two level interleaved boost converter," in *Int. Conf. on Mach. Intell. Res. and Advancement*, Katra, India, 2013, pp. 509–514.

[22]   A. Dolara, R. Faranda, and S. Leva, "Energy comparison of seven MPPT techniques for PV systems," *J. Electromagnetic Analysis & Applications*, no. 3, pp. 152–162, Sep. 2009.

[23]   D. Ragonese and M. Ragusa, "Designing with the SPV1020, an interleaved boost converter with MPPT algorithm," STMicroelectronics, Geneva, Switzerland, App. Note AN3392, May 2012.

[24]   S. Gomathy, S. Saravanan, and S. Thangavel, "Design and implementation of Maximum Power Point Tracking (MPPT) Algorithm for a Standalone PV System," *Int. J. of Scientific & Eng. Res.*, vol. 3, no. 3, pp. 428–434, Mar. 2012.

[25]   T. Esram and P. Chapman, "Comparison of photovoltaic array maximum power point tracking techniques," *IEEE Trans. Energy Convers.*, vol. 22, no. 2, pp. 439–449, Jun. 2007.

[26]   R. Faranda and S. Leva, "Energy comparison of MPPT techniques for PV systems," *WSEAS Transactions on Power Systems*, vol. 3, no. 6, pp. 446–455, Jun. 2008.

[27]   M. A. Gomes de Brito, L. Galotto, Jr., L. P. Sampaio, G. de Azevedo e Melo, and C. A. Canesin, "Evaluation of the main MPPT techniques for photovoltaic applications," *IEEE Trans. Ind. Electron.*, vol. 60, no. 3, pp. 1156–1167, Mar. 2013.

[28]   D. Shmilovitz, "On the control of photovoltaic maximum power point tracker via output parameters," in *IEEE Proc. Elect. Power Appl.*, vol. 152, no. 2, pp. 239–248, Mar. 2005.

[29]   F. Blaabjerg, Z. Chen, and S. B. Kjaer, "Power electronics as efficient interface in dispersed power generation systems," *IEEE Trans. Power Electron.*, vol. 19, no. 5, pp. 1184–1194, 2004.

[30]   C. A. Stephenson, "Utilizing maximum power point trackers in parallel to maximize the power output of a solar (photovoltaic) array," M.S. thesis, Dept. Elect. Comput. Eng., Naval Postgraduate School, Monterey, CA, 2005.

[31]   Diodes in PV systems. (n.d.). OkSolar.com. [Online]. Available: http://www.oksolar.com/technical/diodes_in_pv_systems.htm. Accessed Aug. 10, 2015.

[32]   Diodes in solar arrays. (2001). ABS Alaskan, Inc., Fairbanks, AK. [Online]. Available: http://www.absak.com/tech/diodes.pdf.

[33]   R. Regan. (2012, Dec. 13). Number of bits in a decimal integer. [Online]. Available: http://www.exploringbinary.com/number-of-bits-in-a-decimal-integer/

[34]   C. L. Phillips and H. T. Nagle, *Digital Control System Analysis and Design*, 3rd ed. Englewood Cliffs, NJ: Prentice-Hall, Inc., 1995.

[35]   The MathWorks, Inc. (2015). SimPowerSystems. [Online]. Available: http://www.mathworks.com/products/simpower/

THIS PAGE INTENTIONALLY LEFT BLANK

INITIAL DISTRIBUTION LIST

1.   Defense Technical Information Center
        Ft. Belvoir, Virginia

2.   Dudley Knox Library
        Naval Postgraduate School
        Monterey, California